SMART ACTUATION AND SENSING FOR MESO-SCALE SURGICAL ROBOTIC SYSTEMS

A Dissertation
Presented to
The Academic Faculty

By

Jun Sheng

In Partial Fulfillment
of the Requirements for the Degree
Doctor of Philosophy in
Robotics

Georgia Institute of Technology

August 2019

SMART ACTUATION AND SENSING FOR MESO-SCALE SURGICAL ROBOTIC SYSTEMS

Approved by:

Dr. Jaydev P. Desai
Wallace H. Coulter Department of Biomedical Engineering
Georgia Institute of Technology

Dr. Jun Ueda
George W. Woodruff School of Mechanical Engineering
Georgia Institute of Technology

Dr. Frank L. Hammond III
Wallace H. Coulter Department of Biomedical Engineering
Georgia Institute of Technology

Dr. John N. Oshinski
Wallace H. Coulter Department of Biomedical Engineering
Georgia Institute of Technology

Dr. Zachary L. Bercu
School of Medicine
Emory University

Date Approved: July 2, 2019

The only true wisdom is in knowing you know nothing.

Socrates

To my wife Jiah-Ying Lu and my parents.

ACKNOWLEDGEMENTS

First and foremost, I would like to thank my advisor, Dr. Jaydev P. Desai, for providing invaluable mentorship and great support during my doctoral study. Without his help and guidance, I would not be able to overcome many academic challenges in the past five years. By working with Dr. Desai, I have learned a lot both academically and personally, and I will always be grateful for his mentorship. I would also like to thank Dr. Jun Ueda, Dr. Frank L. Hammond, Dr. John N. Oshinski, and Dr. Zachary L. Bercu for serving on my dissertation committee. Their invaluable suggestions and comments have helped me improve this dissertation.

The research reported in this dissertation was supported in part by the National Institute of Bioengineering Imaging and Bioengineering of the National Institutes of Health under Award Number R21EB019161, R21EB018581, and R01EB015870, and National Heart, Lung, And Blood Institute of the National Institutes of Health under Award Number R01HL140325. The content is solely the responsibility of the author and does not necessarily represent the official views of the National Institutes of Health. This work was performed in part at the Georgia Tech Institute for Electronics and Nanotechnology, a member of the National Nanotechnology Coordinated Infrastructure, which is supported by the National Science Foundation (Grant ECCS-1542174).

I would like to thank my collaborators and lab colleagues for their support. I would like to acknowledge Dr. J. Marc Simard, Dr. Dheeraj Gandhi, Dr. Rao Gullapalli, Dr. Timm-Michael L. Dickfeld, Dr. Jiachen Zhuo, Dr. Mahamadou Diakite, and Dr. Matthew Kole with the University of Maryland School of Medicine for the collaboration work we have done in the analysis and evaluation of the surgical robotic systems in the University of Maryland Medical Center (UMMC). I would also like to acknowledge Dr. Xuefeng Wang, currently an Assistant Professor at the University of Alabama, Tuscaloosa, for collaborating on the development of the low-current SMA bending module and Ms. Nancy J.

Deaton for collaborating on the development of the FBG bending sensor. I am also grateful to other colleagues in the Robotic Automation and Medical Systems (RAMS) Laboratory at University of Maryland College Park and the Medical Robotics and Automation (RoboMed) Laboratory at Georgia Institute of Technology, including Dr. Hardik J. Pandya, Dr. Yeongjin Kim, Dr. Elif Ayvali, Dr. Chad Kessens, Dr. Nahian Rahman, Dr. Seokhwan Jeong, Dr. Shing Shin Chen, Kihan Park, Yash Chitalia, Phillip Tran, Wenxue Zhao, Carolyn Adkins, Dennis Nesline, and Drew D. Elliott. It has been a great pleasure to work with these talented, friendly, and diligent colleagues. I appreciate all the discussions we had and help they provided for my research.

Last but not least, I would like to express my deepest gratitude to my family. I owe a debt of gratitude to my parents, Juming Sheng and Weifang Wu, for all their love and sacrifices which allow me to study abroad and pursue a doctoral degree. I am also grateful to my parents-in-law, Tzong-Shi Liu and Baoin Hsu, for their understanding and encouragement. Most of all, my special thanks go to my lovely wife, Jiah-Ying Lu. It is her support and encouragement that help me successfully complete this research work. .

TABLE OF CONTENTS

Acknowledgments v

List of Tables xiii

List of Figures xiv

List of Abbreviations xxiv

Summary xxvi

Chapter 1: Introduction 1

1.1 Background and Motivation 1

1.2 Related Works 2

1.2.1 Brief History of Surgical Robots 2

1.2.2 Meso-Scale Surgical Robotics 4

1.2.3 Smart Material Actuation 6

1.2.4 Robotic Shape Sensing 8

1.3 Research Objectives and Main Contributions 10

1.4 Organization of the Thesis 12

Chapter 2: SMA Torsion Module 13

2.1 Design and Fabrication 14

2.1.1 Working Principle . . . 14
2.1.2 Torsion Module Development . . . 15
2.1.3 NICHE Robot Development . . . 17
2.1.4 SMA Training . . . 19
2.2 Torsion Module Modeling . . . 21
2.2.1 SMA Torsion Spring Model . . . 21
2.2.2 Torsion Module Static Model . . . 22
2.2.3 Maximum Motion Range . . . 26
2.3 Torsion Module Characterization . . . 29
2.3.1 SMA Torsion Spring Characterization . . . 29
2.3.2 Friction Torque Characterization . . . 34
2.4 Experimental Studies . . . 37
2.4.1 Controller Design . . . 37
2.4.2 Feedback Control Results . . . 39
2.4.3 Proof-of-Concept Demonstration . . . 41
2.5 Discussion and Conclusions . . . 42

Chapter 3: Low-Current SMA Bending Module . . . 44
3.1 Hardware Development . . . 45
3.1.1 Bending Module Design . . . 45
3.1.2 Bending Module Fabrication . . . 46
3.2 Actuator Modeling . . . 48
3.2.1 Electromagnetic Field . . . 48

3.2.2 Heat Transfer 50
3.2.3 SMA Constitutive Model 50
3.3 Experimental Studies 51
3.3.1 Fatigue Tests 51
3.3.2 SMA Actuation Comparison 53
3.3.3 Estimation of Contact Conductance Coefficient 55
3.3.4 Proof-of-Concept Demonstration 57
3.4 Discussion and Conclusions 58

Chapter 4: Fiberoptic Rotation Sensor 59
4.1 Sensor Design and Fabrication 59
4.1.1 First generation: One Fiber Set 59
4.1.2 Second/Third Generation: Multiple Fiber Sets 61
4.2 Light Intensity Modulation Modeling 63
4.2.1 Coordinate Frame Definition 63
4.2.2 LIM for the First Generation 65
4.2.3 LIM for the Second/Third Generation 67
4.3 Preliminary Studies and Calibration 70
4.3.1 Performance Comparison 70
4.3.2 Model Verification 73
4.3.3 Calibration of the First Generation 74
4.3.4 Calibration of the Second/Third Generation 75
4.4 Experimental Evaluation and Demonstration 78

4.4.1 Measurement Algorithm 78
4.4.2 Precision Evaluation 79
4.4.3 Control with the First Generation 83
4.4.4 Control with the Third Generation 84
4.5 Discussion and Conclusions 86

Chapter 5: Large-Curvature FBG Bending Sensor 87
5.1 Hardware Development 87
5.1.1 Sensor Design 87
5.1.2 Sensor Fabrication 89
5.2 Sensor Modeling 90
5.2.1 Fiber Bragg Grating 90
5.2.2 Strain Transfer Model 91
5.2.3 Simulations 94
5.3 Experimental Studies 96
5.3.1 Model Evaluation 96
5.3.2 Temperature Influence on Sensor Output 97
5.3.3 Sensor Influence on Motion Range 98
5.3.4 Evaluation of the Integrated Sensor 99
5.4 Discussion and Conclusions 101

Chapter 6: Neurosurgical Robotic Headframe 102
6.1 Hardware Development 102
6.1.1 System Design and Installation 102

6.1.2 System Fabrication . . . 104

6.2 Kinematic analysis . . . 105

6.2.1 Inverse Kinematics . . . 105

6.2.2 Motion Planning . . . 106

6.2.3 Configuration Optimization . . . 108

6.2.4 Workspace Simulation . . . 110

6.3 Experiment and Demonstration . . . 112

6.3.1 2D Positioning Accuracy . . . 112

6.3.2 3D Positioning Accuracy . . . 114

6.3.3 System Demonstration . . . 116

6.4 Discussion and Conclusions . . . 117

Chapter 7: Image-Guided Studies . . . 118

7.1 *In Vitro* Robot Evaluation . . . 118

7.1.1 MR Imaging-Guided Tests . . . 118

7.1.2 CT Imaging-Guided Manipulation . . . 120

7.2 *Ex Vivo* Robot Evaluation . . . 122

7.2.1 Human Cadaver Head Preparation . . . 122

7.2.2 CT Imaging-Guided Manipulation . . . 123

7.2.3 MR Imaging-Guided Manipulation . . . 125

7.3 Discussion and Conclusions . . . 128

Chapter 8: Conclusions and Future Work . . . 130

8.1 Conclusions . . . 130

8.2 Future Work 131

Appendix A: Headframe Registration in Chapter 6 134

Appendix B: Use of Copyrighted Materials and Permissions 136

Bibliography 137

Vita 154

LIST OF TABLES

2.1 Geometric properties of customized SMA torsion springs 20

2.2 Status sequence of SMA torsion springs 24

2.3 Characterization tests for SMA torsion springs 30

2.4 Results of SMA torsion spring characterization 31

3.1 Properties of SMA wire and nichrome wire 56

4.1 Experimental results of sensor evaluation 81

4.2 Comparison between 3-set sensor and 4-set sensor 83

5.1 Mechanical properties of FBG bending sensor 94

5.2 Results of model fitting and measurement error 100

6.1 Positioning error for entry points 113

6.2 Positioning error for target points 115

LIST OF FIGURES

2.1 Working principle of the SMA torsion module: (a) SMA A and SMA B are pre-tightened by one turn (initial configuration), (b) SMA A is in the recovered configuration (heated) and SMA B is unheated, and (c) SMA A is unheated and SMA B is in the recovered configuration (heated). The red arrows indicate the motion direction of the torsion disk. 14

2.2 Motion process of the SMA torsion module under alternate Joule heating and natural cooling of SMA torsion springs. Status (0) denotes the initial configurations of pre-tightened SMA A and SMA B. Status (1) to status (4) denotes the change of spring configurations when SMA A and SMA B are alternately heated and cooled. 15

2.3 Mechanical design of the SMA torsion module: (a) first generation, (b) second generation, and (c) third generation. 16

2.4 SMA torsion module prototypes: (a) first generation, (b) second generation, and (c) third generation. 17

2.5 Development of the NICHE robot: (a) design of the NICHE robot, (b) NICHE robot with the second-generation torsion module, and (c) NICHE robot with the third-generation torsion module. 18

2.6 Simulation of the workspace of the NICHE robot considering the motion of the SMA bending tip and SMA torsion module. 19

2.7 Customized SMA torsion spring: (a) thermal training setup and (b) geometric schematic. 20

2.8 Torque output of SMA torsion springs versus deformation angle when the spring angle at S_2 is smaller (a) or larger (b) than β_{cr}. The ideal change denotes the torque of the heated spring without the friction torque, while the upper and lower solid lines incorporate the friction when it is equal to τ^c and $-\tau^c$, respectively. [A,M] means that both the austenite phase and martensite phase exist and [M] means that SMA is entirely in the martensite phase. 23

2.9 Torque output of SMA torsion springs versus deformation angle for full-range motion and three cases of pre-deformation and the same number of spring turns. The definitions of ideal change, solid and dash lines, [A,M], and [M] are the same as Figure 2.8. [A] means that SMA is entirely in the austenite phase. 26

2.10 Simulation results: (a) full motion range against pre-deformation and friction torque, (b) optimal pre-deformation against spring turns and friction torque, and (c) full motion range against spring turns and friction torque when the pre-deformation is optimal. 28

2.11 Experimental setup for the SMA torsion spring characterization. 30

2.12 Rotation angle of the SMA torsion spring against temperature during the heating process compared to model predictions. RMSE is 9.5752° for Liang-Rogers model (A_s=36°C,A_f=54°C) and 14.8436° for Tanaka's model (A_s=42°C,A_f=60°C). R^2=0.9771 (-118°, Liang-Rogers), R^2=0.9860 (-138°, Liang-Rogers), R^2=0.9454 (-118°, Tanaka), and R^2=0.9653 (-138°, Tanaka). 31

2.13 Force measurement versus rotation angle of the SMA torsion spring in the small-angle motion range at room temperature. RMSE is 0.0105 N. R^2 value is 0.8475 and 0.7421 for the 1^{st} and the 2^{nd} experiment, respectively. . 32

2.14 Force measurement versus rotation angle of the SMA torsion spring in the large-angle motion range at room temperature. RMSE is 0.0113 N. R^2 value is 0.6357 and 0.7532 for the 1^{st} and 2^{nd} experiment, respectively, in the range of -400° to -300°. 33

2.15 Block force measurement versus temperature of the SMA torsion spring: (a) SMA torsion spring is heated (RMSE is 0.0227 N and R^2 value is 0.9392) and (b) SMA torsion spring is naturally cooled after heating (RMSE is 0.0125 N and R^2 value is 0.9850). 33

2.16 Experimental setup for characterizing the friction torque. 34

2.17 Snapshots of the torsion module moving clockwise as the arrow indicates when SMA A is heated. 36

2.18 Rotation of the torsion module in one cycle. 36

2.19 Temperature of the SMA torsion springs in one cycle. 37

2.20 Rotation angle of the torsion module versus the temperature of SMA A when SMA A is heated and then naturally cooled (RMSE is 16.7588° and R^2 value is 0.9867). 37

2.21 Block diagram of the double-channel cascade PI controller. 38

2.22 Experimental results: (a) Sinusoidal tracking at 0.017 Hz frequency (RMSE is 1.67°), (b) Sinusoidal tracking at 0.025 Hz frequency (RMSE is 2.05°), (c) Sinusoidal tracking at 0.050 Hz frequency (RMSE is 3.60°), (d) step input response with the time step of 30s and step size of 20° (upper) and time step of 30s and step size of 10° (lower), (e) Quasi-static tracking with both feed-forward and feedback compensation from 0s to 300s (RMSE is 1.86°) and only feedback compensation from 300s to 600s (RMSE is 2.24°), and (f) Quasi-static tracking with only feed-forward compensation applied from 0s to 300s (RMSE is 8.19°) and only feedback compensation applied from 300s to 600s (RMSE is 2.58°). 40

2.23 Experimental setup for the gelatin evacuation demonstration: (a) NICHE robot connected to a suction device and a electrosurgery generator and (b) gelatin evacuated from the slab and transferred into the cup. 42

2.24 Snapshots of the gelatin evacuation demonstration with (a) and (b) showing the deflection of the bending tip and (b)→(i) showing the articulation of the end effector. 42

3.1 Robotic cardiac catheter consisting of a flexible stem and a steerable tip. . . 45

3.2 Design of the robotic catheter: (a) steerable tip comprised of multiple SMA bending modules, (b) assembly of two bending modules with orthogonal bending directions, (c) assembly of two bending modules via a positive adapter, (d) assembly of two bending modules via a negative adapter, and (e) nichrome coils routed around an SMA wire of the bending module. The red arrows show bending directions and the blue arrows show assembly directions. 47

3.3 Fabrication of the SMA bending module: (a) fixing an SMA wire onto the jigs followed by routing a nichrome wire, (b) assembling two SMA wires to a module link, and (c) connecting the module link with SMA wires to another link. The blue arrows indicate assembly directions. 48

3.4 Photos showing the fabrication of the SMA bending module: (a) nichrome wire routed around the SMA wire, (b) two SMA wires assembled with one module link, (c) assembling another module link, and (d) prototype of the SMA bending module. 49

3.5 Fatigue tests of the SMA bending module: (a) experimental setup, (b) microscopic view before actuation, and (c) microscopic view before actuation after 200 cycles. 51

3.6 Experimental results of fatigue tests: (a) maximum bending angles versus bending cycles and (b) twist angles of the SMA bending module versus bending angles. 52

3.7 Comparison between Joule heating actuation and conductive heating actuation: (a) experimental setup to measure the block force, (b) block force under Joule heating actuation, and (c) block force under conductive heating actuation. 54

3.8 Comparison between Joule heating actuation and conductive heating actuation in terms of heating response (a) and natural cooling response (b). . . . 55

3.9 Angular recovery percentage of the SMA wire versus electric current applied to the nichrome coils. RMSE and R^2 value of the experimental results with respect to the model prediction are 0.0704 and 0.9775, respectively. . 56

3.10 Manipulation of the steerable robotic catheter inside the right atrium: (a) catheter inserted through the inferior vena cava and viewed from the superior vena cava, (b) straight steerable tip before actuation, (c) tip moving upward, (d) tip moving downward, (e) tip moving leftward, and (f) tip moving rightward. 57

4.1 Design of the first-generation fiberoptic rotation sensor: (a) fiberoptic rotation sensor to be integrated with the SMA torsion module, (b) fiberoptic rotation sensor consisting of an optical fiber set, a rotary head, and a shaft, and (c) two designs of the rotary head with different reflective surface profiles. 60

4.2 Fiberoptic rotation sensor prototype: (a) SMA torsion module integrated with a fiberoptic rotation sensor, (b) type I rotary head made of aluminum, and (c) type II rotary head made of brass. 61

4.3 Design of the second-generation fiberoptic rotation sensor: (a) exploded view of NICHE robot assembly and (b) exploded view of the fiberoptic rotation sensor with the subset showing the assembly of the rotor, shaft, and bearing. 62

4.4 Fabrication of the reflective sensor rotor: (a) 3D-printed rotor with a brass micro mirror, (b) microscopic view of the brass micro mirror, (c) bonding brass disks onto a glass wafer before polishing, and (d) polishing brass disks using a wafer polisher. 63

4.5 Geometrical optics for the reflective rotor: (a) optical fibers transmitting a light beam towards the type I rotary head, (b) optical fibers transmitting a light beam towards the type II rotary head, and (c) light beam towards the reflecting point, D, on the type I rotary head in $\mathrm{x_s}$-$\mathrm{z_s}$ plane. 64

4.6 Modulation of the light intensity received by the optical fibers for the first-generation sensor. 66

4.7 Working principle of the second-generation sensor: (a) three optical fiber sets pointing to the reflective sensor rotor, (b) four optical fiber sets pointing to the reflective sensor rotor, (c) one optical fiber set transmitting light to the sensor rotor in the $\mathrm{x_s}$-$\mathrm{z_s}$ plane, and (d) light beam transmitted and received by two different optical fiber sets in the second-generation sensor. 68

4.8 Simulation results of sensitivity: (a) normalized sensitivity versus rotation angle for different fiber sets and (b) normalized sensitivity versus number of fiber sets. 70

4.9 Experimental setup for comparing the working performance of different designs and verifying the developed model for the first-generation sensor. . 71

4.10 Experimental results for different designs of the first-generation sensor: (a) comparing two type I rotary heads made of brass and aluminum, (b) comparing two different off-the-shelf optical fiber sets, (c) comparing a brass type I rotary head and a brass type II rotary head. 72

4.11 Normalized experimental results when the shaft of the first-generation sensor is rotated by 360°: (a) RMSE is 0.04 and R^2 value is 0.98 for the brass type I rotary head and (b) RMSE is 0.17 and R^2 value is 0.54 for the brass type II rotary head. 73

4.12 Calibration of the first-generation sensor: (a) rotation angle versus sensor output (R^2 values for the linear fitting 1, 2, and 3 are 0.98, 0.88, and 0.55, respectively) and (b) comparing the measurements of the rotary encoder and the developed fiberoptic rotation sensor (RMSEs are 2.27°, 2.06°, 4.36°, and 5.99° for the tests when (A_s, T_s) is equal to (120°, 120 s), (120°, 60 s), (120°, 30 s), and (240°, 120 s), respectively). 74

4.13 Experimental setup for calibrating the second-generation fiberoptic rotation sensor. 75

4.14 Calibration of the second-generation sensor: (a) voltage output of three fiber sets (A, B, and C) versus rotation angle when the sensor shaft rotates from 0° to 360° and then to 0° for eight cycles, (b) 3D space formed by the voltage output of the three fiber sets with showing negligible hysteresis, and (c) normalized average voltage output of the three fiber sets. 76

4.15 Calibration of the third-generation sensor: (a) voltage output of the three-set sensor, (b) normalized output of the three-set sensor, (c) voltage output of the four-set sensor, and (d) normalized output of the four-set sensor. . . . 77

4.16 Measurement error analysis for the second-generation sensor: (a,b) error histograms of the measurements based on the average, normalized calibration results for (a) positive rotation and (b) negative rotation, and (c) average measurement error and system sensitivity versus rotation angle. . . 79

4.17 Evaluation tests for the second-generation sensor: (a) $A_\theta = 180°$ and $T_\theta = 20\ s$, (b) $A_\theta = 180°$ and $T_\theta = 40\ s$, (c) $A_\theta = 360°$ and $T_\theta = 40\ s$, (d) $A_\theta = 360°$ and $T_\theta = 80\ s$, (e) $A_\theta = 540°$ and $T_\theta = 60\ s$, and (f) $A_\theta = 540°$ and $T_\theta = 120\ s$. The rotation angles are relative to the initial position. . . . 80

4.18 Measurement error analysis for the third-generation sensor: (a,c) average measurement error and sensitivity versus rotation angle for three-set sensor (a) and four-set sensor (c), and (b,d) error histograms for three-set sensor (b) and four-set sensor (d). 81

4.19 Evaluation tests for the second-generation sensor: (a) $T_\theta = 80\ s$, (b) $T_\theta = 60\ s$, (c) $T_\theta = 40\ s$, and (d) measurement error comparison. 82

4.20 Feedback control of the SMA torsion module integrated with the first-generation sensor: (a) experimental setup and (b) comparing the actual rotation angles with stepwise references. 83

4.21 Feedback control of the tip articulation of the NICHE robot integrated with the first-generation sensor: (a-b) initial (a) and final (b) robot configuration for a 120° step input to the SMA torsion module, (c) measurements of the fiberoptic rotation sensor for the step input, and (d) measurements of the fiberoptic rotation sensor for the linear position references. 84

4.22 Feedback control of the tip articulation of the NICHE robot integrated with the third-generation sensor: (a) experimental setup, (b) robot at the initial configuration, (c) robot at the final configuration, (d) position of the vision marker in the x-y plane during robot tip articulation, and (e) measurements by the third-generation fiberoptic rotation sensor. 85

5.1 System design and fabrication: (a) SMA bending module integrated with the FBG bending sensor, (b) design of the FBG bending sensor, and (c) fabrication of the FBG bending sensor. 88

5.2 System prototypes: (a) superelastic Nitinol strip, (b) FBG bending sensor, (c) zoom-in sagittal view of the sensor, and (d) SMA bending module integrated with the sensor. 89

5.3 Analytical model of the FBG bending sensor: (a) cross-section view and (b) sagittal view. 92

5.4 Simulation results: (a) sensitivity versus adhesive shear modulus, G_a, (b) sensitivity versus adhesive thickness, t_s, (c) sensitivity versus coating thickness, $r_c - r_f$, (d) strain at the upper and lower edges of the upper and lower fibers versus curvature for current design, (e) maximum strain in the fibers versus adhesive shear modulus at the curvature of 100 m^{-1}, and (f) maximum strain in the fibers versus adhesive thickness at the curvature of 100 m^{-1}. Ratio is the sensitivity of case I to case II. The red dot indicates the current design. 95

5.5 Experimental model evaluation: (a) bending sensor constrained in a curved slot on a model and (b) comparison between the experimental results with model predictions. 97

5.6 Analysis of temperature influence: (a) wavelength shift with temperature change and (b) temperature measurements of the two grating segments. . . . 97

5.7 Experimental setup: (a) photo showing vision markers attached to the SMA bending module and (b) schematic showing the placement of RTD sensors. . 98

5.8 Motion range of the SMA bending module versus motion cycles (sensor is removed after the 21$^{\text{st}}$ cycle). 98

5.9 Calibration results of the FBG bending sensor integrated with the SMA bending module: (a) electric current increased from 0 to 38 mA, (b) electric current increased from 0 to 30 mA (hysteresis loop (a) denotes the hysteresis loop in figure (a)), (c) experimental results of 100 cycles with the Prandtl-Ishlinskii hysteresis model. 100

6.1 Robotic headframe prototype: (a) headframe mounted on a human skull model, (b) snap-fit mechanism, to attach the NICHE robot to the rack, (c) NICHE robot attached to the rack, (d) vision markers placed around the base plate of the headframe, and (e) rack actuated by a DC motor via a pinion. 103

6.2 Installation of the skull-mounted headframe including: (a) fixing the pedestal using bone anchoring screws, (b) installing the Stewart platform on the pedestal, (c) attaching the NICHE robot to the rack, and (d) installing the linear actuation module interfaced with the NICHE robot onto the Stewart platform. 103

6.3 Definitions of coordinate frames: (a) coordinate frames for the Stewart platform and (b) Tait-Bryan rotation convection for the linear actuation module. 105

6.4 Kinematic relationship among the NICHE robot, entry point, and target point. 107

6.5 Workspace of the headframe when the entry point is fixed at $[0, 0, -28]^T$: (a) 3D view and (b) top view. (c) Maximum tilt angle in the x_b-axis when the lower bound varies between [110 mm, 150 mm] for different $\{r_b, r_j\}$. (1:{45,40},2:{45,30},3:{45,35},4:{40,35},5:{50,35}). (d) Maximum tilt angle along the x_b-axis versus r_b and r_u. 110

6.6 Maximum tilt angle in the positive and negative directions along x_b- and y_b-axis versus the entry point position: (a) entry point shifts along the x_b-axis and (b) entry point shifts along the y_b-axis. 111

6.7 Experimental evaluation of 2D positioning accuracy: (a) a slender rod with a conical tip manipulated by the headframe and (b) indentation on the grip paper with red dots showing the planned entry points. 112

6.8 Experimental setup for evaluating 3D positioning accuracy: (a) headframe manipulating a slender rod with a vision marker on the tip and (b) all vision markers detected by the stereoscopic camera. 114

6.9 Registration of the base plate of the headframe and tip of the rod by detecting all the vision markers using the stereoscopic camera: (a) isometric view and (b) top view. 115

6.10 Proof-of-concept demonstration: (a) robotic headframe interfaced with the NICHE robot mounted on a container filled with gelatin phantom, (b) NICHE robot steered by the robotic headframe towards the entry hole, (c) NICHE robot inserted into the simulated hemorrhage (red gelatin core), (d) distal bending tip of the NICHE robot actuated and deflected, and (e) torsion module of the NICHE robot actuated and the end effector articulating within the gelatin phantom. 116

7.1 MRI-compatibility evaluation: (a) experimental setup with the SMA-actuated catheter tip inside a water container and (b) SNR values of MR images acquired before actuation (baseline), when the tip moves upward and downward, and after actuation (baseline again). 119

7.2 Manipulation of the SMA-actuated catheter tip under MR imaging guidance: (a) before Joule heating actuation, (b) during Joule heating actuation, (c) before conductive heating actuation before actuation, (d) tip moving upward under conductive heating actuation, (d) tip moving downward under conductive heating actuation, and (f) after conductive heating actuation. . . 119

7.3 Experimental setup for CT imaging-guided tests on phantom models: (a) NICHE robot within the cantaloupe and (b) shaded surface display of the NICHE robot in a gelatin slab. 120

7.4 CT imaging of the tip articulation of the NICHE robot within the cantaloupe by actuating the SMA torsion module. 121

7.5 Screenshots of the multi-planar display capabilities of cone-beam CT and I-Guide reconstructions during the NICHE robot manipulation within the cantaloupe. 121

7.6 Preparation of the *ex vivo* studies on a human cadaver head: (a) removing scalp, (b) drilling a burr hole on the skull, (c) drilling screw holes using a mold, (d) mounting the pedestal onto the skull, (e) installing the headframe onto the pedestal, and (f) inserting the NICHE robot and fixing its position using brass screws. 122

7.7 Experimental setup for CT imaging-guided tests on a human cadaver head: (a) overall view and (b) close-up view. 123

7.8 CT imaging-guided manipulation of the NICHE robot in the human cadaver brain: (a) cone-beam CT imaging showing artifacts, (b) beginning of tip deflection, (c) end of tip deflection, (d) beginning of tip articulation, (e) during tip articulation, and (f) end of tip articulation. 124

7.9 Experimental setup for MR imaging-guided tests on a human cadaver head: (a) overall view and (b) close-up view. 125

7.10 Dynamic MR imaging of the NICHE robot in the coronal plane: (a) human cadaver head without the NICHE robot, (b) NICHE robot in the brain before tip deflection, (c) bending tip of the NICHE robot deflecting towards the left, and (d) bending tip of the NICHE robot deflecting towards the right. The red rectangle shows the ROI for calculating SNR values. 126

7.11 Dynamic MR imaging of the NICHE robot in the transverse plane: (a) human cadaver head without the NICHE robot, (b) NICHE robot in the brain before tip articulation, (c) robot tip articulating clockwise by actuating the SMA torsion module, and (d) robot tip at a stable position. The red rectangle shows the ROI for calculating SNR values. 127

7.12 Change of SNRs value for dynamic MR imaging: (a) SMA bending tip actuated and (b) SMA torsion module actuated. The baseline denotes the SNR values when the human cadaver head was placed inside the bore of the MRI scanner without the NICHE robot. 128

LIST OF ABBREVIATIONS

3D Three-Dimensional.

CT computed tomography.

DEA Dielectric Elastomer Actuator.

DoF Degree of Freedom.

EDM Electric Discharge Machining.

EM Electromagnetic Tracking.

FBG Fiber Bragg Grating.

ICH Intracerebral Hemorrhage.

IPMC Ionic Polymer-metal Composite.

LA Left Atrium.

LED Light-Emitting Diode.

LIM Light Intensity Modulation.

MIS Minimally Invasive Surgery.

MOSFET Metal–Oxide–Semiconductor Field-Effect Transistor.

MRI Magnetic Resonance Imaging.

NiTi Nickel-Titanium.

PVs Pulmonary Veins.

PWM Pulse Width Modulation.

RF Radiofrequency.

RMSE Root-Mean-Squared Error.

ROI Region of Interest.

RTD Resistance Temperature Detector.

SMA Shape Memory Alloy.

SMP Shape Memory Polymer.

SNR Signal-to-Noise Ratio.

TCE Trichloroethylene.

TE Echo Time.

TR Repetition Time.

UV Ultraviolet.

SUMMARY

This dissertation presents the development of meso-scale surgical robotics based on smart actuation and sensing for minimally invasive surgery (MIS). By replacing conventional straight tools by steerable surgical robots, surgical outcomes can potentially be improved due to more precise, stable, and flexible manipulation. Since bending and torsion are the two fundamental motion forms required by surgical tools to complete general surgical procedures, compact torsion and bending modules, both integrated with intrinsic sensors for motion feedback, have been developed based on shape memory alloy (SMA). By actuating individual modules at discrete joints, a meso-scale surgical robot can be steered while avoiding motion coupling and snapping problem suffered by other surgical robotic techniques.

The SMA torsion module is developed by bonding two pre-tightened, antagonistic SMA torsion springs with a rotary shaft, and enclosing all components in a housing to protect the device from external tissue and liquid. By alternately heating an individual SMA torsion spring while keeping the other at low temperature, bi-directional motion of the torsion module will be initiated by the shape recovery of the SMA springs. To control the torsion module in a closed-loop manner, a fiberoptic rotation sensor has been developed based on the light intensity modulation (LIM) mechanism. By modulating the light received by optical fibers using a reflective rotor, the rotation of the SMA torsion module can be measured and precisely controlled. The SMA bending module is developed by bonding two straightened, antagonistic SMA wires between two rigid links. A bending sensor is developed for the SMA bending module by bonding two fiber Bragg grating (FBG) fibers with a superelastic Nitinol substrate using flexible adhesive. By installing the sensor in the center of the bending module, the deflection of the bending module will induce wavelength shift of the reflected light inside the FBG fibers. A conductive heating actuation technique is developed to significantly reduce the electric current required to actuate SMA modules.

By routing nichrome coils around each SMA wire of the bending module, the SMA wire can be energized via conductive heating at the nichrome wire due to the high resistance of nichrome coils. As a result, the system safety and MRI compatibility are improved.

The developed actuation and sensing techniques have been applied on a robot for neurosurgical intracerebral hemorrhage evacuation (NICHE) and a steerable catheter for atrial fibrillation (AFib) treatment. The NICHE robot consists of a straight stem, an SMA torsion module, and an SMA bending module as a distal bending tip. By synchronizing the motion of the stem, the bending module, and the torsion module, the robot is capable of tip articulation within the brain to remove hemorrhage effectively through suction and electrocauterization. In addition, a skull-mounted robotic headframe has been developed based on a Stewart platform to manipulate the NICHE robot. The robotic catheter is developed by integrating multiple SMA bending modules with flexible braid reinforced tubing. Polymer 3D-printing is used to fabricate all the structural components due to its relatively low cost, short fabrication period, and capability of fabricating complicated structures with high accuracy. The developed surgical robotic systems have been thoroughly evaluated using phantom or cadaver models under computed tomography (CT) and/or magnetic resonance imaging (MRI) guidance. The imaging-guided experimental studies showed that the developed robotic systems consisting of smart actuation and sensing were compatible with CT and MR imaging.

CHAPTER 1
INTRODUCTION

As a revolutionary technology related to human health care, surgery has enabled physicians and patients to fight against many diseases that are difficulty to be cured by medicine. In 2008, nearly 234 million surgical procedures were operated [1]. To improve surgical outcomes and perform procedures that are conventionally impossible, robot-assisted surgery has been developed. In 2012, it was estimated that over 400,000 robot-assisted procedures were performed in the United States [2]. How to develop to robotic systems that can perform various kinds of procedures efficiently, effectively, and safely becomes a major concern. Therefore, it is desirable to develop highly flexible and steerable meso-scale surgical robots.

1.1 Background and Motivation

Minimally invasive surgery (MIS) has become a popular choice for physicians when they plan interventional treatment for many health-related conditions. Compared with conventional open surgery, MIS usually causes much less trauma to patients, leading to better surgical outcomes and shorter hospital stay. A typical MIS involves inserting one or multiple endoscopic tools into a patient body through small incisions. However, the manipulation of endoscopic tools demands high expertise of surgeons due to physiological limitations. To reduce the tremor of surgeons' hands and improve manipulation precision, robot-assisted MIS using robotic manipulators interfaced with endoscopic tools has been developed to explore the essential precision and stability of robotic manipulators. Nevertheless, most endoscopic tools for MIS are straight and rigid with limited steerability, resulting in limited workspace and the difficulty in treating targets out of sight or deformable targets [3]. Therefore, meso-scale surgical robotics with high steerability are of great interest to both research and clinical communities to further improve outcomes of robot-assisted MIS.

Despite much effort has been made to develop meso-scale surgical robotics, it is still an open question to develop highly compact and reliable actuation mechanisms for imaging-guided meso-scale surgical robots. It is observed that in current MIS for various applications, torsion and bending are the two fundamental motion capabilities required by interventional tools. When intra-operative imaging guidance is required, the space restriction and imaging compatibility requirement will make it more challenging to achieve robotic bending and torsion motion. Smart materials and structures have shown their potential in robotic actuation and sensing, but their applications surgical robotics is still at an early stage due to the challenges in the design, manufacturing, and control of smart actuators and sensors. It is believed that by pushing the envelope of smart actuation and sensing, a variety of fundamental techniques can be developed for meso-scale surgical robotic for various applications.

1.2 Related Works

1.2.1 Brief History of Surgical Robots

The development of robot-assisted MIS was initiated by the applications of industrial robots on surgical procedures. The first surgical robot was a 6-degree-of-freedom (DoF) PUMA robot used to manipulate a needle for brain biopsies in 1985 [4]. In 1991, PUMA 200 was used to manipulate a surgical retractor to remove deep-seated low-grade brain tumors in six children [5]. Since then, a variety of robotic manipulators have been customized for surgical procedures to improve safety and realize special functions, some of which have been marketed and applied in clinic studies. For example, ROBODOC was developed by Integrated Surgical Systems (Sacramento, CA, USA) for total hip arthroplasty [6]. It is equipped with a high-speed drill and allows for the optimization of prosthesis size. Since ROBODOC obtained FDA approval in 2008, it has been used in more than 24,000 procedures [7]. A breakthrough for surgical robotics came in early 2000s when da Vinci

Surgical System (Intuitive Surgical Inc., Sunnyvale, CA, USA) obtained FDA approval for general laparoscopic MIS. This system is teleoperated by surgeons who sit beside remote consoles, observe magnified three-dimensional (3D) images of surgical sites, and control ergonomically designed master manipulators. By now, it is the most used surgical robotic system in the world and known for its customizability, high steerability, and high dexterity. Other examples of surgical robots applied in clinic studies include NeuroMate (Renishaw, Wotton-under-Edge, UK) and ROSA (Medtech, Montpellier, France) for various intracranial procedures [8–11], Renaissance (Mazor Robotics Ltd., Caesarea, Israel) for spinal interventions [12], CyberKnife (Accuray Incorporated, Sunnyvale, CA, USA) for radiosurgery [13], etc.

Surgical robots may have the following advantages compared with surgeons: (a) surgical robots possess superior positioning precision and accuracy to perform procedures with the minimal damage to healthy tissue; (b) surgical robots with multiple degrees-of-freedom (DoFs) have high steerability to overcome movement limitations imposed on surgeons' hands. To utilize these two potential advantages, three types of robot-assisted MIS have been developed so far according to the role played by surgical robotics in surgery, namely assistive mode, autonomous mode, and teleoperated mode [14]. In the assistive mode, a surgical robot shares its workspace with a surgeon by providing a support structure for the surgeon's upper limbs to reduce tremor and prevent risky movement, or positioning an endoscopic instrument nearby an incision before the surgeon manually inserts it. Nevertheless, the assistive mode only works for a fully passive tool, such as a cannula or a needle. To control the micro instruments at the tip of endoscopic tools, such as scissors and gripers, the autonomous or teleoperated mode is usually employed. In the autonomous mode, a surgical procedure is performed autonomously by a surgical robot without any interventions by surgeons. In the teleoperated mode, a surgeon remotely operates a master device while a slave robot follows the trajectory of the master device. As a result, surgical procedures can gain benefits of tremor filtration and motion scaling from this mode. Since the teleoperated mode maintains surgeons' control of surgical procedures while taking full advantage of robotic manipulation, it is usually the optimal choice for surgeons currently and will remain so in the near future.

1.2.2 Meso-Scale Surgical Robotics

Intracranial neurosurgery, namely surgery on the human brain, is one of the MIS disciplines that tremendously demand meso-scale surgical robotics due to the delicacy, complexity, and deformability of brain structures. To avoid delicate, complex critical brain structures, insertion path planning has to be performed meticulously based on pre-operative imaging for conventional straight tools, and sometimes solutions may not exist. To treat targets of a relatively large volume and irregular geometry, repetition of insertion and retraction may be involved for straight tools, which will probably cause significant trauma to healthy tissue. Therefore, meso-scale surgical robots with multiple DoFs can potentially enhance neurosurgical outcomes by precisely reaching targets and maintaining configurations stability. Another MIS discipline that has attracted much research focus is transcatheter cardiothoracic surgery, which may be an option for patients who are unqualified for conventional open surgery. However, since the respiratory system and cardiovascular system contain many bifurcations and sharp turns, it is challenging to perform cardiothoracic surgery using a passive guidewire and/or catheter. Therefore, a meso-scale robot, namely a robotic catheter, can potentially improve the surgeons' capability in reaching challenging surgical cardiothoracic cites.

The body of a meso-scale surgical robot can be a continuum structure, such as a spring backbone [15], a wire backbone [16], or a flexible tube, or an articulated structure consisting hinged rigid links [17]. According to their working principles, meso-scale surgical robots can be classified into several major categories, including tendon-driven robots [15–17], concentric-tube robots [18–20], magnetically actuated catheters [21], bevel-tipped needles [22], and smart material actuated robots [23, 24]. A tendon-driven robot is actuated by pulling the tendons connected to the robot body. For example, a tendon-driven robot consisting of a spring backbone was developed by Kim et al. for brain tumor removal [25]. A concentric-tube robot is formed by multiple concentric pre-curved tubes, so that the robot tip can be manipulated by rotating, inserting, and retracting the tubes. For example, a concentric-tube robot was developed for intracerebral hemorrhage evacuation [26, 27] and a motion planning algorithm was proposed for lung surgery using a concentric-tube robot [28, 29]. A bevel-tipped needle is deflected by the reactive force applied on the bevel tip by soft tissue, so that the motion trajectory is controlled by rotating the needle during insertion [22]. However, the deflection is limited by the small reactive force, and it is challenging to control the needle in nonhomogeneous tissue [30]. A magnetically actuated catheter is steered by the force generated at discrete joints in the magnetic field, such as inside a magnetic resonance imaging (MRI) scanner bore [21]. For smart material actuated surgical robots, SMA is the most widely used smart actuation technique for surgical robotics, and more details will be discussed in the following subsection. Compared with other working principles, SMA can avoid joint coupling and snapping issues suffered by tendon-driven robots and concentric-tube robots, respectively [25, 31]. So far, several robotic catheters for cardiothoracic surgery have obtained FBA approval and introduced to the market. For example, a robotic magnetic navigation system was developed to manipulate a catheter via two permanent magnets to perform ablation for atrial fibrillation treatment (Stereotaxis, St. Louis, MO, USA), and Monarch Platform (Auris Health Inc., Redwood City, CA, USA) and Ion endoluminal system (Intuitive Surgical Inc., Sunnyvale, CA, USA) were intended for the diagnosis and treatment of lung cancer through natural openings.

In a typical MIS, imaging modalities such as computed tomography (CT), fluoroscopy, MRI, and ultrasound are usually used to obtain pre-operative or intra-operative images to provide visualization of surgical targets. For soft-tissue structures, such as brain and vasculatures, MRI and CT show their superiority in providing high-contrast 3D imaging. To register surgical instruments and detect target deformation and shift in real time, intra-operative imaging guidance is desired by many procedures; however, it is challenging to obtain continuous, intra-operative CT and MR imaging due to safety concern and space limitation. Intra-operative CT imaging is usually acquired discontinuously to allow surgeons to manipulate surgical instruments during imaging intervals and to avoid excessive radiation exposure to patients, surgeons, and nurses. To address the safety concern caused by radiation exposure, MRI is an alternative solution. However, since MR imaging usually takes place in the confined bore of an MRI scanner in an isolated suite, surgeons' access to patients is prohibited during MR imaging. To overcome these challenge, meso-scale surgical robots compatible with imaging modalities have been developed to perform imaging-guided procedures with the remote control outside the MRI suite [17, 18, 24, 25, 32, 33]. To develop a compatible robotic system, the system safety in the magnetic field should be ensured (namely MRI safety) and the influence to imaging quality should be minimal (namely MRI compatibility). In the literature, ultrasonic piezoelectric motors and SMA are the three most used MRI-safe actuators. For example, piezoelectric motors were used to actuate MRI-compatible concentric-tube robots [18, 32], ultrasonic motors and SMA spring actuators were used in a spring-based tendon-driven robot [25, 33], and SMA wires and springs were used to actuate articulated meso-scale neurosurgical robots [17, 24]. To minimize the influence of the electromagnetic field generated by these actuators, they are usually placed remotely by using tendon-driven transmissions [17, 33].

1.2.3 Smart Material Actuation

Smart materials, including piezoelectric material, dielectric elastomer actuator (DEA), ionic polymer-metal composite (IPMC), shape memory polymer (SMP), SMA, soft fluidic actuator, etc., have been investigated extensively for a variety of robotic applications [34], such as piezoelectrically actuated Harvard RoboBee [35], DEA-actuated legged robots [36, 37], IPMC-actuated fish robots [38], etc. Among all the smart materials, SMA is one of the most promising techniques for surgical robotics due to its appropriate properties for meso-scale robotic actuation, including high stress, compactness, low cost, etc. SMA is a type of alloys that can memorize particular shapes. Once above a critical transformation temperature, SMA can recover the memorized shape due to microscopic crystal lattice transformation from martensite phase to austenite phase, which is known as shape memory effect (SME) [39]. To memorize a particular shape, as-drawn SMA has to go through a series of typical training procedures, including fixing SMA at a desired shape, thermal treatment using an oven [40] or laser energy [41], and annealing. Via the choices of heating and annealing conditions, critical SMA properties, such as Young's modulus and transformation temperatures, can thereby be adjusted [42]. Via reheat treatment, two-way SMA can be manufactured to memorize two different shapes at high and low temperatures, respectively, but their small recoverable strain and short fatigue life have prohibited them from being used in robotic applications [43, 44]. As a result, bi-directional SMA actuators are usually formed by a pair of antagonistic SMA elements or a combination of an SMA element and a bias element, such as a spring [45] or a flexible body structure [46]. Although several kinds of SMA exist, nickel-titanium (NiTi) alloys, also known as Nitinol, is the most popular option for surgical robotic applications, due to its relatively low transformation temperature, large recoverable strain, high stress, and MRI safety [47].

SMA can be used to realize robotic bending and rotation in a variety of geometric forms. An as-drawn SMA wire or strip is usually trained to memorize a curved configuration. By clamping an SMA wire inside a flexible rod, a steerable cannula for diagnostic or therapeutic purposes can be developed [48–50]. To develop a flexible meso-scale surgical robot, multiple discrete joints are individually actuated by a pair of antagonistic SMA wires or strips [23, 24, 51]. Due to the capability of generating large linear displacements, SMA linear springs were used as low-cost linear actuators for tendon-driven robots [17, 25, 52]. By bonding SMA linear springs around the flexible continuum body of a surgical robot, the robot can be deflected omni-directionally by heating selected SMA springs [53–55].

Flat meandering springs were fabricated by chemical etching to develop submillimeter catheters [56, 57]. Several SMA rotary actuators were proposed, but they were inappropriate for meso-scale surgical robotics. For example, a torsion actuator was built upon an SMA rod for the helicopter rotor blade [58]. Several more compact rotary actuators were developed by winding an SMA wire around a torsion cylinder against a torsion spring [59], or transmitting the motion and force of SMA wires to a rotary shaft via monolithic flexures [60], but it is intractable to miniaturize these designs. To the best of the author's knowledge, the only meso-scale surgical robot equipped with an SMA rotation actuator is a catheter with a pre-twisted SMA wire embedded in its flexible continuum body [50]. Although Joule heating is a convenient method to energize SMA actuators, it lowers the MRI-compatibility of SMA actuators due to the magnetic field generated by electric current through SMA. To address this issue, optical heating using laser energy through optical fibers was developed to develop an MRI-compatible SMA-actuated surgical robot [48].

1.2.4 Robotic Shape Sensing

Knowledge of the shape of a meso-scale surgical robot during operation can assist surgeons to avoid important structures in anatomical confines, efficiently reach target targets, and successfully perform procedures with the minimal trauma to patients. Although the shape of some types of surgical robots, such as tendon-driven robots and concentric-tube robots, can be estimated via forward kinematics [20, 61], it is challenging to develop precise kinematic models due to uncertainty in hysteresis, friction, payload, and interaction with soft tissue and blood [19, 61]. Commercial magnetic, capacitive, or optical encoders have been extensively used in conventional robotic manipulators, but their applications in meso-scale systems are intractable due to form factors. In addition, due to onboard electronics, their functional reliability is low when exposed to strong radiation or magnetic field generated by imaging modalities. As a result, several innovative techniques have been developed for the motion feedback of meso-scale surgical robotics, such as fiberoptic sensing, electromagnetic tracking (EM), and imaging-based shape reconstruction [62].

The precision of EM tracking may suffer from errors caused by nearby magnetic and conductive devices used during surgical procedures. When imaging-based shape reconstruction is applied, it is challenging to precisely estimate the shape of surgical robots. MR imaging cannot provide real-time information without sacrificing imaging quality for a continually moving tool due to relatively long imaging time [63]. Fluoroscopic imaging is either unsuited for continuous, real-time tracking since it exposes patients to ionizing radiation, and ultrasound imaging usually suffers from low resolution and imaging artifacts [64]. Fiberoptic shape sensing is promising to address this challenge owing to its compact size, immunity from radiation and magnetic field, and real-time implementation. So far, light intensity modulation (LIM) and fiber Bragg grating (FBG) are the two typical working principles for robotic fiberoptic sensing. An LIM-based sensor usually works by measuring the variation of light intensity caused by joint motion. For example, a LIM-based sensor consisting of an IR emitter and an IR detector was developed to measure the rotation of a robotic endoscope [52]. An FBG fiber contains discrete grating segments with varied reflective index so that light of particular wavelength can be reflected. Once the axial strain or temperature of an FBG fiber changes, the wavelength of reflected light will be shifted [65].

Previous studies have attempted to use FBG to develop intrinsic shape sensors for surgical tools. For non-robotic tools, three FBG fibers with four grating segments per fiber were embedded into grooves of a flexible needle for 3D shape estimation [66], and an MRI-compatible biopsy needle was developed by bonding three FBG fibers inside three grooves at 120 degree intervals using a low-viscosity biocompatible cyanoacrylate adhesive [67]. A helical wrapping of FBG fibers over a continuum robot was proposed to measure curvature, force, and torsion based on force-curvature-strain model [68]. To develop a standalone sensing assembly, a polymer tube consisting of surface mounted FBG fibers was proposed [69]. Araújo et al. fixed two D-shaped FBG sensors together to compensate for temperature sensitivity of strained FBG during shape estimation [70]. Chen et al. offset the fiber core from the neutral axis of its coating and reported high sensitivity of the device [71]. Liu et al. bonded an FBG fiber along two superelastic Nitinol wires in a triangular configuration and threaded the sensing assembly through a channel along a continuum manipulator to measure its planar deflection [72]. So far, the largest curvature reported in the literature is about 66.6 m^{-1}, achieved by a sensing assembly consisting an FBG fiber and two superelastic Nitinol wires encased in a polycarbonate tube [73]. It is still open question to develop compact and flexible large-curvature bending sensors for meso-scale surgical robots.

1.3 Research Objectives and Main Contributions

From the discussion of the existing literature, the development of meso-scale surgical robots is still at an early stage. It is desired to develop fundamental actuation and sensing technologies for imaging-guided meso-scale surgical robots.

In this thesis, SMA is explored to develop various actuation modules for meso-scale surgical robotics with an innovative actuation technique for improved safety and reliability. In addition, intrinsic motion sensors have been developed for the proposed SMA actuation modules, which are applied on a neurosurgical robot and a robotic catheter. As a result, it is promising to push image-guided meso-scale surgical robotics closer to clinical applications, bringing benefits to patients requiring interventional treatment. The primary contributions presented by this thesis are listed as follows:

1) A compact and lightweight SMA torsion module is developed to achieve torsion motion in surgical procedures. Two pre-tightened SMA torsion springs are bonded with the disc of a shaft. By heating one SMA spring while keep the other at low temperature, the energized spring will go through a recovery process towards its memorized configuration, leading to the rotation of the shaft and tightening of the antagonistic spring. The system is analytically modeled and the analytic optimal pre-deformation for the maximum motion

range is investigated. This technology is applied on a robot for neurosurgical intracerebral hemorrhage evacuation (NICHE) equipped with electrocautery probes and suction tubing.

2) A conductive heating technique is developed for SMA actuation and applied on SMA bending modules. By wrapping high-resistance nichrome wiring over SMA, the electric current required by SMA actuation is significantly reduced compared with conventional direct Joule heating actuation. As a result, the MRI-compatibility, safety, and reliability of SMA actuators can be improved, enabling more appropriate SMA actuators for surgical applications. This technology is applied on the SMA bending tip of the NICHE robot, as well as a robotic catheter consisting of multiple SMA bending modules for the diagnosis and treatment of atrial fibrillation.

3) A fiberoptic rotation sensor based on the LIM mechanism is developed for the motion feedback of the SMA torsion module. The sensor is comprised of multiple off-the-shelf optical fibers and a tilted reflector mounted on the sensor shaft. Once the reflector rotates, the intensity of the light received by optical fibers is modulated by the reflector due to varying distance, resulting in varying output of a conditioner converting received light intensity to analog voltage. Different reflector materials and profiles, as well as fabrication methods are investigated to optimize the sensor performance.

4) An FBG bending sensor is developed to measure large-curvature deflections of the SMA bending module. A superelastic Nitinol substrate is bonded with an FBG fiber with a grating segment using flexible adhesive. Once the sensor is deflected, the difference between surface strains of the substrate and fiber induces shear strain within adhesive, resulting in axial strain in the fiber and wavelength shift. Due to the small shear modulus of flexible adhesive, the sensing assembly is flexible and large curvatures can be measured while ensuring the strain of the fiber below the strain limit.

5) The developed meso-scale robotic systems consisting of smart actuation and sensing modules are evaluated by performing imaging-guided experiments using *ex-vivo* and/or *in-vitro* models. Various components of the robots can be clearly identified against soft-tissue

structures in CT and MR images. The experiments show that the developed fiberoptic rotation sensor is capable of working under CT radiation, and the MRI-compatibility of the robotic system is improved by using the conductive heating technique.

1.4 Organization of the Thesis

The rest of the thesis is organized as follows. Chapter 2 presents the development of SMA torsion and bending modules for meso-scale surgical robotics. Chapter 3 details the conductive heating actuation technique for SMA modules. Chapter 4 presents the development of a fiberoptic rotation sensor for the SMA torsion module. Chapter 5 describes a flexible, large-curvature FBG bending sensor for the SMA bending module. Chapter 6 details a skull-mounted parallel robotic headframe for manipulating a meso-scale neurosurgical robot. Chapter 7 presents several evaluating experiments under intra-operative imaging guidance. Finally, Chapter 8 concludes the thesis.

CHAPTER 2

SMA TORSION MODULE

Torsion motion is considered as an important motion for the success of many surgical procedures. For example, intracerebral hemorrhage (ICH) is a common health issue and affects a significantly large population. It occurs when blood accumulates inside the brain due to the rupture of blood vessels. As a major cause of stroke [74], less than 40% of patients survive the first year [75]. To remove an intracerebral blood clot, an open craniotomy may be implemented, but it usually incurs neural damage and recurrent bleeding. To address these issues, MIS was proposed as an alternative solution [76]. A surgical tool with an articulating tip will help surgeons effectively remove blood clots with negligible trauma to healthy tissue. However, it is challenging to realize torsion motion during surgical procedures, especially when intra-operative imaging modalities are used. Hydraulic and pneumatic actuators are usually bulky, electromagnetic motors are prohibited in the MRI environment, and the force output of micro piezoelectric actuators is limited [77–80]. A concentric-tube robot was been developed for ICH removal by rotating a pre-curved inner tube inside a straight, stiff outer tube [26, 27]. To develop a compact system, this chapter will present a methodology to utilize shape memory alloy (SMA) to develop a torsion module for a neurosurgical intracerebral hemorrhage evacuation (NICHE) robot. Considering the localization error of commercial imaging-guided neurosurgical systems (e.g., Stealth™ Navigus™ frameless biopsy solution (Medtronic PLC, Dublin, Ireland) [81]), 1 mm is set as the target positioning accuracy for the NICHE robot.

The rest of this chapter is organized as follows. Section 2.1 presents the design and fabrication of the SMA torsion module. Section 2.2 presents the analytic model of the SMA torsion module. Section 2.3 presents a series of experiments to characterize the develop model. Section 2.4 presents the development of the NICHE robot and experimental evaluation of the torsion module and the robot. Section 2.5 concludes the chapter.

2.1 Design and Fabrication

2.1.1 Working Principle

When an SMA torsion spring is heated, it tends to recover its memorized shape due to its internal crystal transformation from martensite phase (M) to austenite phase (A). Figure 2.1 shows the working principle of the proposed SMA torsion module. Two SMA torsion springs (SMA A and SMA B) with the same properties are coaxially fixed at the green points and connected to a torsion disk at the orange points. In case (a), both springs are pre-tightened. When SMA A or SMA B partially recovers its memorized configuration after it is heated, the system status is shown in case (b) or (c), respectively. In case (b) or (c), when SMA B or SMA A is heated, it will start recovering its memorized configuration, rotating the torsion disk counter-clockwise or clockwise (top view), and tightening the other spring. Since the SMA Young's modulus is large at high temperatures, the immediate heating of the SMA spring after the heating process of the other one can hardly reverse the torsion disk. Therefore, a cooling process is required between alternate heating processes

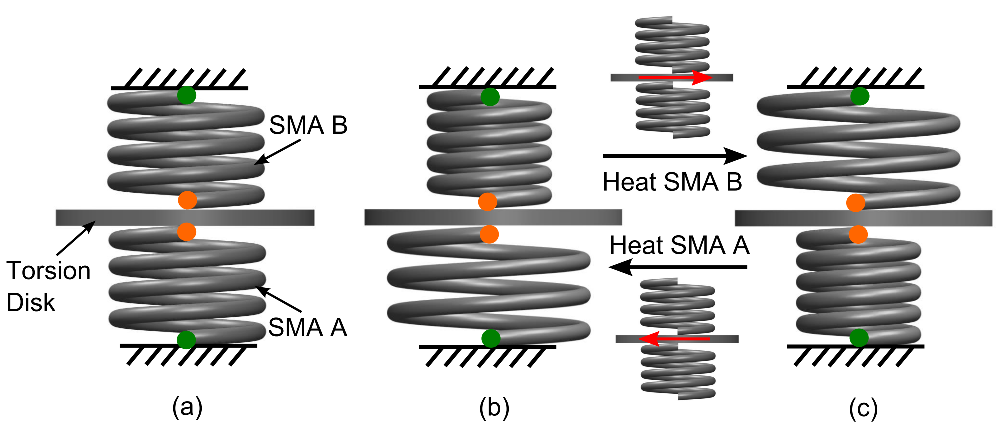

Figure 2.1: Working principle of the SMA torsion module: (a) SMA A and SMA B are pre-tightened by one turn (initial configuration), (b) SMA A is in the recovered configuration (heated) and SMA B is unheated, and (c) SMA A is unheated and SMA B is in the recovered configuration (heated). The red arrows indicate the motion direction of the torsion disk.

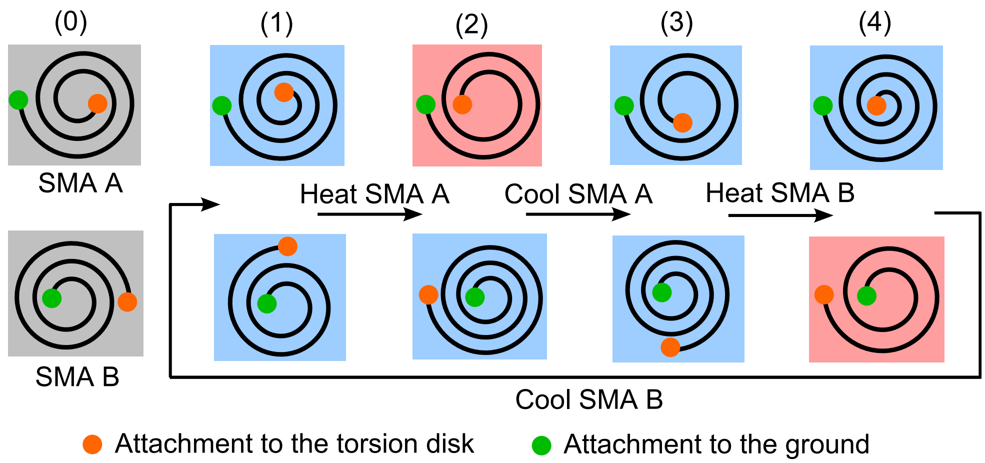

Figure 2.2: Motion process of the SMA torsion module under alternate Joule heating and natural cooling of SMA torsion springs. Status (0) denotes the initial configurations of pre-tightened SMA A and SMA B. Status (1) to status (4) denotes the change of spring configurations when SMA A and SMA B are alternately heated and cooled.

and natural cooling by ambient atmosphere is used. Figure 2.2 shows the typical motion of the torsion module by heating and cooling individual SMA springs alternately. In Status (0), both springs are pre-tightened by half a turn as their initial configurations.

2.1.2 Torsion Module Development

Figure 2.3(a) shows the schematic diagram of the torsion module consisting of a shaft, which is a metallic screw, two disks fixed at the two ends of the shaft, a torsion disk in the middle, and two SMA torsion springs fixed between the disks. Three supporting rods are connected between the torsion disk and an output disk. Two insulating sheaths are threaded along the shaft to constrain the axial position of the torsion disk and prevent short circuit. Grease is applied to reduce the friction on the torsion disk. By selecting an appropriate spring wire diameter and an appropriate coil pitch, the friction torque caused by the contact between the spring turns can be minimized. After assembly, both springs are pre-tightened equally. The SMA torsion springs is customized based on a 0.5 mm diameter as-drawn Nitinol wire (Dynalloy, Inc.) and the fabrication details will be presented in Section 2.1.4. In their natural configurations, both springs contain five turns with a counter-clockwise

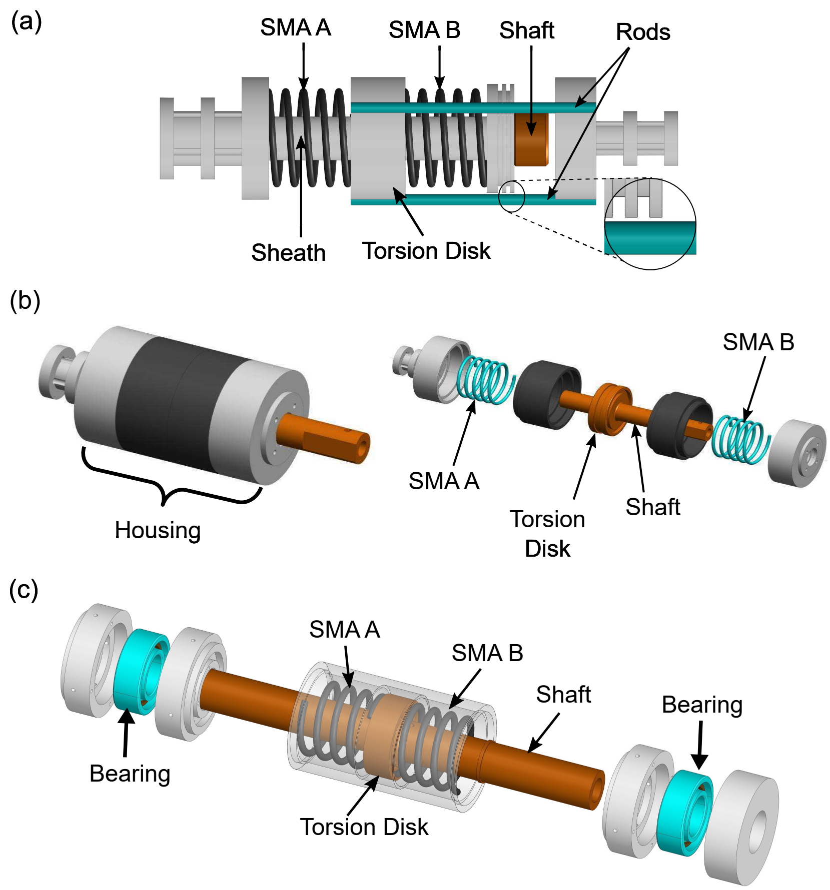

Figure 2.3: Mechanical design of the SMA torsion module: (a) first generation, (b) second generation, and (c) third generation.

winding shape. For each spring, the number of deformable turns, N_0, is equal to three in our design, since the first and last turns are fixed on the disks.

Considering that the torsion module for surgical procedures needs to work in the humid environment, it is necessary to insulate the SMA elements and electrical wiring to ensure effective Joule heating and to avoid short circuit. To seal the torsion module, an improved design is proposed, as shown in Figure 2.3(b). All components are enclosed in a 11 mm diameter and 20 mm long housing with a cover at each end. A shaft with a through hole is 3D-printed with the torsion disk as a monolithic piece. Two SMA torsion springs are installed by fixing one end of each spring on the torsion disk and the other end on the housing cover. Therefore, by applying Joule heating alternately, the torsion disk can be rotated bi-directionally together with the shaft. The shaft contains micro steps at the two

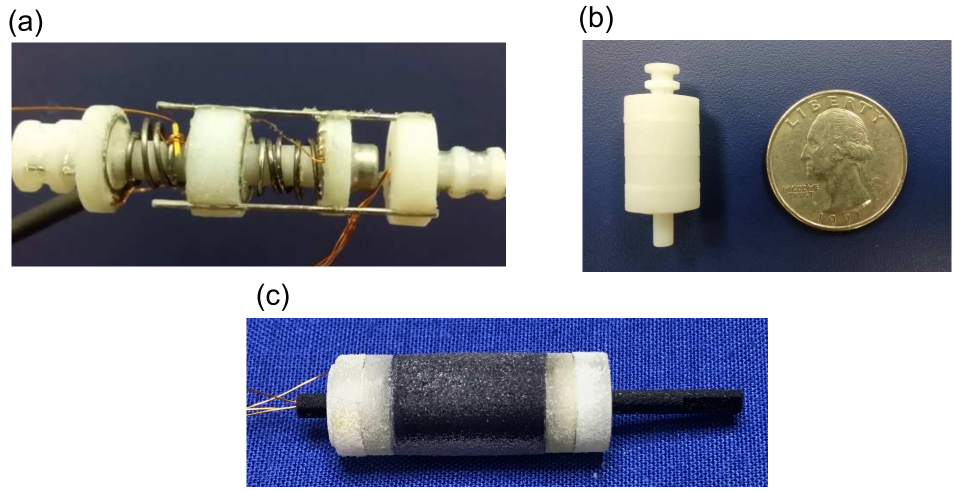

Figure 2.4: SMA torsion module prototypes: (a) first generation, (b) second generation, and (c) third generation.

ends to constrain its axial motion. Electrical wires for Joule heating can pass through the micro holes on the shaft and then through the central hole to the outside. To reduce the friction torque, the torsion disk with the shaft can be 3D-printed in brass and grease is filled between the torsion disk and the shell. In the third generation, two micro bearings are used to support the rotary shaft, as shown in Figure 2.3(c). Thus, the torsion disk/shaft can be 3D-printed in plastic material and the rotary motion is more smooth than previous generations. The diameter of the torsion module is further reduced to 7 mm, resulting in less invasiveness compared than the previous torsion modules when used for surgical procedures. Figures 2.4(a) to (c) show the SMA torsion modules of these three generations.

2.1.3 NICHE Robot Development

The NICHE robot is primarily comprised of a stiff and straight stem, an SMA torsion module, and a distal bending tip. The bending tip is made of a pair of antagonistic SMA wires that can recover curved configurations at high temperature. Thus, the tip can be deflected bi-directionally by heating individual SMA wires [23]. By actuating the torsion module and bending tip simultaneously, articulation of the robot tip can be realized. Figures 2.5(a) and (b) show the 3D model and prototype of the NICHE robot equipped with the second-

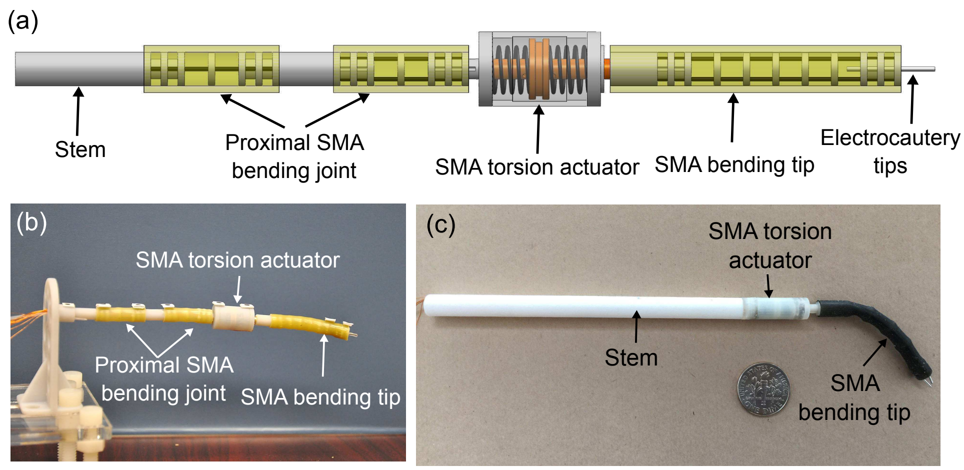

Figure 2.5: Development of the NICHE robot: (a) design of the NICHE robot, (b) NICHE robot with the second-generation torsion module, and (c) NICHE robot with the third-generation torsion module.

generation torsion module. Two proximal bending joints made of antagonistic SMA wires, similar to the bending tip, are integrated with the NICHE robot to augment its motion capability. Since the SMA wires are eccentrically placed, the bending joint or bending tip will be slightly twisted when it is deflected, due to the torque applied by the energized SMA wire. Therefore, circular disks are threaded through the SMA wires and equally spaced to enhance the torsional stiffness and thereby minimize the torsion motion of the bending joint or tip when it is deflected. Silicone rubber tubing is threaded through the bending tip and bending joints to insulate SMA wires from the environment. Aluminum rods are installed at the robot tip as electrocautery tips to perform electrocauterization procedures. Meanwhile, micro tubing runs through the central channel through the robot for irrigation and suction purposes at the robot tip.

Figure 2.5(c) shows the NICHE robot prototype equipped with the third-generation torsion module. A flexible sleeve is 3D-printed in elastomeric material and threaded through the bending tip for insulation. All the structural components are 3D-printed in VisiJet® CR-CL 200 (3D Systems, Rock Hill, SC, USA) due to high precision, surface smoothness, and bio-compatibility of this material. VisiJet® CR-BK can be an alternative 3D-printing material due to its relatively higher heat distortion temperature than CR-CL 200, but it is

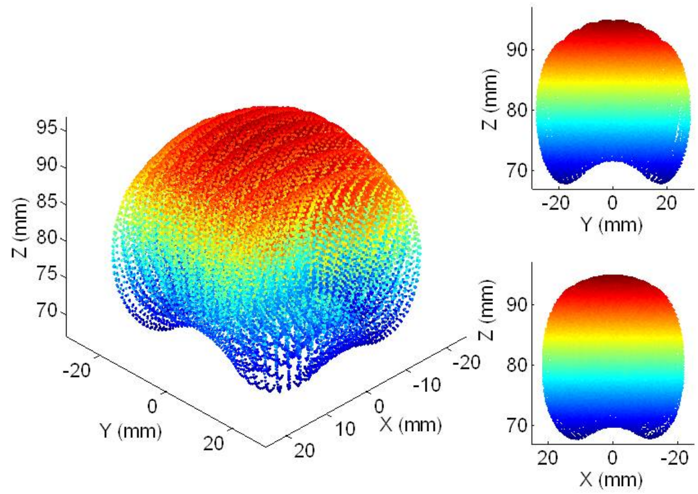

Figure 2.6: Simulation of the workspace of the NICHE robot considering the motion of the SMA bending tip and SMA torsion module.

not bio-compatible. Enameled copper wires are soldered to the two ends of each SMA wire or spring for Joule heating by using the Indalloy® Flux (Indium Corporation, Clinton, NY, USA). The workspace of the NICHE robot is simulated based on the forward kinematics considering the motion of the distal bending tip and the SMA torsion module. As shown in Figure 2.6, the workspace is able to cover a spherical hemorrhage up to 40 mm in diameter. A patient study showed that most hemorrhages possessed a diameter smaller than 5 cm [82]. Considering that the distal bending tip of the NICHE robot can be customized in this length, the workspace of the NICHE robot is sufficient for most ICHs.

2.1.4 SMA Training

The training procedure for the SMA torsion spring includes two steps. As shown in Figure 2.7(a), the first step is shaping the SMA torsion spring by winding a 0.5 mm diameter as-drawn Nitinol wire around a metallic screw mounted on a steel block. The two ends of the Nitinol wire are fixed by screws and nuts. A trade-off exists between the force output and device footprint when selecting the diameter of the Nitinol wire. By using a thinner Nitinol wire, the torsion module will be more compact, but the force output of the spring

Table 2.1: Geometric properties of customized SMA torsion springs

Parameter	Meaning	Value	Unit
D_0	Initial Mean Diameter	6.8	mm
d	Wire Diameter	0.5	mm
N_{c0}	Initial Coil Number	5	N/A
N_0	Initial Active Coil Number	3	N/A
p	Coil Pitch	1.3	mm

during shape recovery may not be large enough to overcome external loading. A 5/16”-18 thread size screw is used as the shaping screw to allow sufficient gap between the spring turns and minimize the friction when the spring tightens up. The geometric properties of the SMA torsion spring for the torsion module are summarized in Table 2.1.

The second step is the heat treatment of the shaped torsion spring. The SMA wire wound around the screw on the steel block is kept in an oven at 490°C for 40 minutes. After this, this assembly is dipped inside an ice-water mixture for quenching. After the annealing process, the SMA wire is removed from the steel block and an SMA torsion spring with one-way shape memory is fabricated. When the SMA torsion spring is deformed and then heated, it will tend to recover its original shape and output force at its two ends if the two ends are constrained.

The SMA wire for the bending tip is fabricated in a similar way. A 0.5 mm diameter as-drawn Nitinol wire is manually routed around a bolt by one turn and fixed on a steel

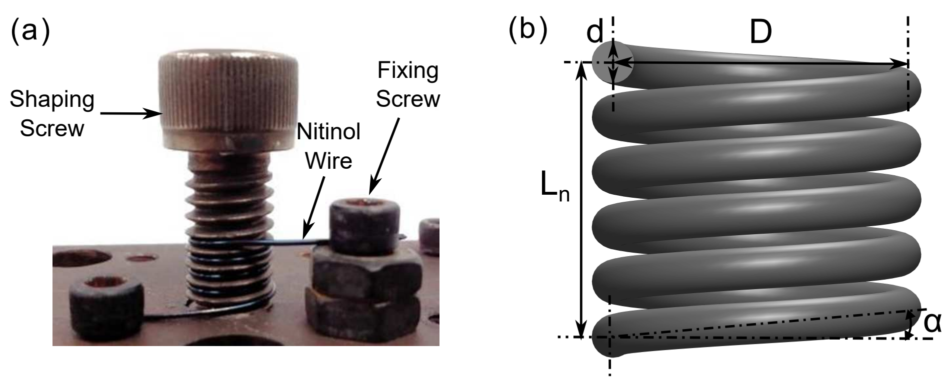

Figure 2.7: Customized SMA torsion spring: (a) thermal training setup and (b) geometric schematic.

block by screws, followed by heat treatment as described above. As a result, the SMA wires memorizes a bending angle of 360° at the curvature of about 192.31 m^{-1}.

2.2 Torsion Module Modeling

2.2.1 SMA Torsion Spring Model

The axial length of the SMA torsion spring is assumed to be constant under pure torsion. Thus, the shear strain caused by axial pre-compression is negligible. By considering each spring turn as a bending wire, the maximum normal strain of a bending spring turn at its outer and inner edge, ϵ, is given by:

$$\epsilon = C_1\theta \tag{2.1}$$

where $C_1 = \frac{d}{2L_s}$, and d, L_s, and θ represent the wire diameter, wire length, and torsion angle of the spring, respectively. For a torsion spring, the maximum normal stress, σ, caused by external torque, τ, is given by:

$$\sigma = C_2 K_c \tau \tag{2.2}$$

where $C_2 = \frac{32}{\pi d^3}$ and K_c is the stress-concentration factor approximately equal to one. To model the nonlinear characteristics of the SMA torsion spring, the Liang-Rogers model [83] is used. By substituting Equations (2.1) and (2.2) into the Liang-Rogers model, the constitutive model for the SMA torsion spring is given by:

$$C_2(\tau - \tau_0) = C_1 E(\theta - \theta_0) - C_1 \theta_L E(\xi - \xi_0) \tag{2.3}$$

where E, ξ, and θ_L represent the SMA Young's modulus, martensite volume fraction, and the maximum recoverable torsion angle, respectively. The variables with subscript '0' denote their initial states. Thermal expansion is neglected, because the strain change caused by thermal expansion is much smaller than that caused by phase transformation. By substituting Equations (2.1) and (2.2) into the expressions for ξ in the Liang-Rogers model [83],

ξ is rewritten for the SMA torsion spring as:

$$\xi_{M\rightarrow A} = \frac{\xi_0}{2}\{\cos[\frac{\pi}{A_f - A_s}(T - A_s - \frac{C_2\tau}{C_A})] + 1\} \tag{2.4}$$

and

$$\xi_{A\rightarrow M} = \frac{1-\xi_0}{2}\cos[\frac{\pi}{M_s - M_f}(T - M_f - \frac{C_2\tau}{C_M})] + \frac{1+\xi_0}{2} \tag{2.5}$$

where T is the spring temperature, A_s and A_f are the start and end temperatures for M→A, respectively, M_s and M_f are the start and end temperatures for A→M, respectively, and C_A and C_M are the coefficients representing the influence of stress on the transformation temperatures for these two processes, respectively. Using Equations (2.1) and (2.2), the torsional stiffness of the torsion spring, K, can be expressed as: $K = C_1E/C_2$. The value of E is a combination of Young's modulus in the entirely martensite phase, E_M, and entirely austenite phase, E_A, as a function of ξ, if ϵ is smaller than a critical strain, ϵ_s^{cr}. If ϵ is larger than ϵ_s^{cr}, E is constant and equal to E_S. Therefore, the torsional stiffness can be written as:

$$K = \begin{cases} K_A + \xi(K_M - K_A) & \theta \leq \theta_s^{cr} \\ K_S & \theta > \theta_s^{cr} \end{cases} \tag{2.6}$$

where

$$\theta_s^{cr} = \epsilon_s^{cr}/C_1, \tag{2.7}$$

$K_M = C_1E_M/C_2$,$K_A = C_1E_A/C_2$, and $K_S = C_1E_S/C_2$. ϵ_s^{cr} is the critical strain that denotes the start of stress-induced martensite phase.

2.2.2 Torsion Module Static Model

The SMA torsion spring is defined to be deformed positively if it tightens. Thus, the positive deformation angles for SMA A, θ^A, and SMA B, θ^B, are counter-clockwise and clockwise, respectively (see Figure 2.2). Since the torsion module outputs torque from the torsion disk, the counter-clockwise rotation of the torsion disk is defined as the positive motion of the torsion module, θ^J. The deformation angles of SMA A and SMA B satisfy the following angular constraint:

$$\theta^A + \theta^B = \theta^P \tag{2.8}$$

where θ^P is the summation of the pre-deformation angles of both springs. Since the torque of each SMA torsion spring points to its recovered configuration, the torque directions of SMA A and SMA B are always clockwise (negative) and counter-clockwise (positive), respectively (see Figure 2.2). When the external loading is negligible, and SMA A and SMA B are balanced during the quasi-static motion of the torsion module, we have the following torque constraint:

$$-\tau^A + \tau^B + \tau^f = 0 \tag{2.9}$$

where τ^A and τ^B are the torque magnitudes of SMA A and SMA B, respectively. τ^f is the friction torque and it is assumed that $\tau^f = -\tau^c sign(\dot{\theta}^J)$ when the torsion module rotates, where τ^c is the magnitude of the critical torque for motion initiation. When the torsion disk is stationary, τ^f varies between $\pm\tau^c$. According to the angular and torque constraints, two conclusions can be drawn: 1) The angle of the heated spring is equal to the difference between θ^P and the angle of the unheated spring; 2) The torque magnitude of the heated spring is equal to the summation of the torque magnitude of the unheated spring and the friction torque. Therefore, two typical motion processes are shown in Figure 2.8 based on

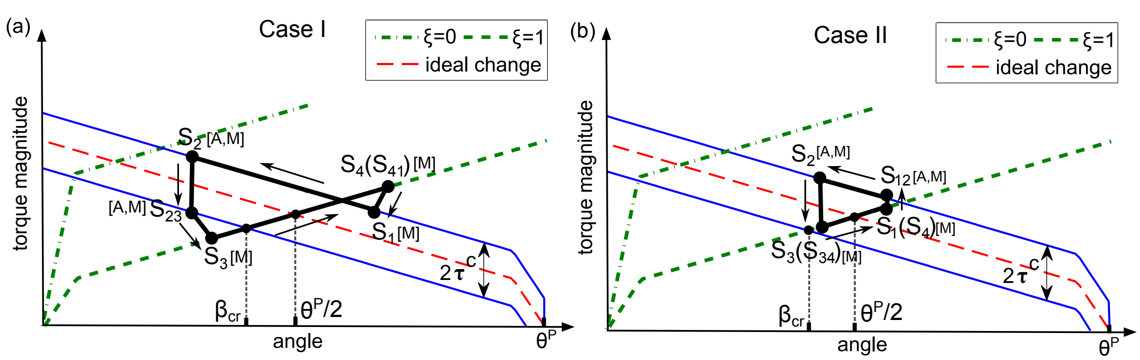

Figure 2.8: Torque output of SMA torsion springs versus deformation angle when the spring angle at S_2 is smaller (a) or larger (b) than β_{cr}. The ideal change denotes the torque of the heated spring without the friction torque, while the upper and lower solid lines incorporate the friction when it is equal to τ^c and $-\tau^c$, respectively. [A,M] means that both the austenite phase and martensite phase exist and [M] means that SMA is entirely in the martensite phase.

Table 2.2: Status sequence of SMA torsion springs

Case I	1	2	3	4	5	6	7	...
SMA A	S_1	S_2	S_{23}	S_3	S_4	S_{41}	S_1	...
SMA B	S_3	S_4	S_{41}	S_1	S_2	S_{23}	S_3	...
Case II	1	2	3	4	5	6	7	...
SMA A	S_1	S_{12}	S_2	S_3	S_{34}	S_4	S_1	...
SMA B	S_3	S_{34}	S_4	S_1	S_{12}	S_2	S_3	...

the stiffness model for the SMA torsion spring (see Equation (2.6)). In Table 2.2, each row shows the motion sequence of an individual SMA torsion spring and each column shows the simultaneous statuses of both springs.

These two cases in Figure 2.8 are differentiated by whether the angle of the SMA torsion spring at S_2 is smaller (case I) or larger (case II) than a critical angle, β_{cr}. In case I, when the SMA torsion spring is heated from S_1 to S_2, the antagonistic spring is passively deformed from S_3 to S_4. In the cooling process from S_2 to S_3, the spring is stationary in the beginning due to the friction torque and starts moving at S_{23} when the friction torque magnitude achieves τ^c. Meanwhile, the antagonistic spring is stationary from S_4 to S_{41} with a constant torque due to its constant stiffness at room temperature. From S_{41} to S_1, the deformation of the antagonistic spring is relaxed to some extent. Therefore, the path inclinations from S_1 to S_2, S_{23} to S_3, S_3 to S_4, S_{41} to S_1 are equal to $-E_S$, $-E_M$, E_S, and E_M, respectively. In case II, when the spring is heated, it is stationary in the beginning due to the friction torque and starts moving at S_{12} when the friction torque magnitude achieves τ^c at S_{12}. Thus, the antagonistic spring is stationary from S_3 to S_{34} and passively deformed from S_{34} to S_4. When the spring is cooled, it is stationary in the whole cooling process due to the friction torque from S_2 to S_3. Meanwhile, the antagonistic spring is stationary from S_4 to S_1 and outputs a constant torque. Therefore, the path inclinations from S_{12} to S_2 and S_{34} to S_4 are equal to $-E_S$ and E_S, respectively.

A general physical parameter for SMA A or SMA B at S_i is denoted by using a superscript of A_i or B_i, respectively. Since both springs have the same properties, SMA A is used for modeling. In both the heating and cooling processes, the governing equation for SMA A is given by Equation (2.3). In the heating process of case II, since SMA A is stationary until S_{12} and its martensite volume fraction is one at S_1, the governing equation at S_{12} is given by:

$$C_2(\tau^{A_{12}} - \tau_0^{A_1}) = -C_1\theta_L^A E^A(\xi^{A_{12}} - 1) \tag{2.10}$$

where $\tau_0^{A_1}$ and $\tau^{A_{12}}$ are functions of θ^{A_1}. By writing Equation (2.10) as a quadratic form, $\xi^{A_{12}} \in [0, 1]$ can be solved unless τ^c is too large. Since the friction torque is constant once SMA A starts moving, τ^A proportionally changes with θ^A. Based on the governing Equation (2.3), θ^A from S_1 to S_2 in case I and from S_{12} to S_2 in case II is solved as:

$$\theta^A = \theta_0^A + \frac{E^A}{E^A + E_S}(\xi^A - \xi_0^A)\theta_L^A \tag{2.11}$$

where ξ_0^A is equal to one for the process from S_1 to S_2 in case I and $\xi^{A_{12}}$ for the process from S_{12} to S_2 in case II. Since E^A is a function of ξ^A, which can be expressed by T^A and τ^A using Equation (2.4), and τ^A is dependent on θ^A based on Equation (2.6), the nonlinear relationship between θ^A and T^A can be obtained from Equation (2.11). Although it is difficult to explicitly express θ^A as a function of T^A, we can numerically solve T^A with the reference of θ^A by computing the references of ξ^A and τ^A using Equations (2.11) and (2.6), and substituting them into Equation (2.4). In the cooling process of case II, SMA A is stationary from S_2 to S_3 , so we have $\theta^A = \theta^{A_2}$. In the cooling process of case I, SMA A is stationary until S_{23}, so the governing equation at S_{23} is rewritten as:

$$C_2(\tau^{A_{23}} - \tau_0^{A_2}) = -C_1\theta_L^A E^A(\xi^{A_{23}} - \xi_0^{A_2}) \tag{2.12}$$

where $\tau_0^{A_2}$ and $\tau^{A_{23}}$ are functions of θ^{A_2}, and $\xi_0^{A_2}$ can be obtained from Equation (2.4) as the result of the previous heating process. By using the quadratic form of Equation (2.12), $\xi^{A_{23}} \in [0, 1]$ can be solved. After S_{23}, SMA A starts moving with the constant friction torque. By using a method similar to that for the heating process, θ^A from S_{23} to S_3 in case I is solved as:

$$\theta^A = \theta_0^A + \frac{E^A}{E^A + E_M}(\xi^A - \xi_0^A)\theta_L^A \tag{2.13}$$

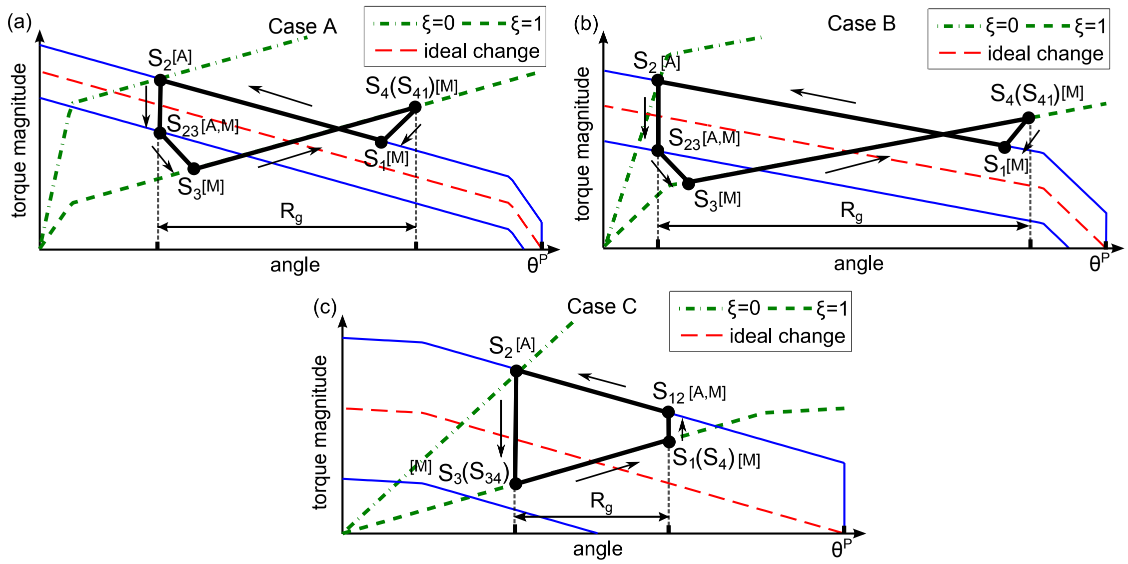

Figure 2.9: Torque output of SMA torsion springs versus deformation angle for full-range motion and three cases of pre-deformation and the same number of spring turns. The definitions of ideal change, solid and dash lines, [A,M], and [M] are the same as Figure 2.8. [A] means that SMA is entirely in the austenite phase.

where ξ_0^A is equal to $\xi^{A_{23}}$ for the process from S_{23} to S_3 in case I. Based on the reference of θ^A, we can numerically compute T^A by using Equations (2.4), (2.6), and (2.11). The critical angle β_{cr} can be computed using the following geometric relationship, as shown in Figure 2.8, when the deformation angle is equal to β_{cr}:

$$K_M\theta_s^{cr} + K_S(\beta_{cr} - \theta_s^{cr}) = K_M\theta_s^{cr} + K_S(\theta^P - \beta_{cr} - \theta_s^{cr}) - \tau^c \tag{2.14}$$

which yields:

$$\beta_{cr} = \frac{\theta^P}{2} - \frac{\tau^c}{2K_S}$$

The other two processes for SMA A when SMA B is heated and cooled, which are S_3 to S_4 and S_4 to S_1, respectively, can be modeled based on the angular constraint (see Equation (2.8)) and the modeling results for SMA B.

2.2.3 Maximum Motion Range

The full motion range of a rotary actuator made of a pair of antagonistic SMA wires is numerically solved based on the force balance between the actuated SMA wire and the load [84]. In this paper, we investigate the optimal pre-deformation of SMA torsion springs to maximize the full motion range by using an analytic approach based on the derived model. The maximum motion range is affected by N_0, θ^P, and τ^c, and our objective is to find the optimal θ^P under certain N_0 and τ^c. When SMA A (SMA B) is at S_2, the angle of SMA A (SMA B) is the minimum, denoted by $\theta^{A_2}_{min}$ ($\theta^{B_2}_{min}$), and the angle of SMA B (SMA A) is the maximum, denoted by $\theta^{B_4}_{max}$ ($\theta^{A_4}_{max}$). The motion range, R_g, is equal to the difference between $\theta^{A_2}_{max}$ and $\theta^{A_2}_{min}$ (or $\theta^{B_2}_{max}$ and $\theta^{B_2}_{min}$) and given by: $R_g = \theta^{A_4}_{max} - \theta^{A_2}_{min}$. Due to the angular constraint (see Equation (2.8)) and the identity between SMA A and SMA B, R_g can be rewritten as:

$$R_g = \theta^P - 2\theta^{A_2}_{min} \tag{2.15}$$

Based on the derived model, different pre-deformations under certain N_0 result in three types of motion cycles with the full motion range as shown in Figure 2.9. When the deformation angles of SMA A and SMA B are the minimum and maximum, respectively, the torque balance between SMA A at S_2 and SMA B at S_4 is given by:

$$\tau^{A_2} = \tau^{B_4} + \tau^c \tag{2.16}$$

where τ^{A_2} and τ^{B_4} are functions of $\theta^{A_2}_{min}$ for the three cases and given by:

$$\tau^{A_2} = \begin{cases} K_A\theta^{cr}_s + K_S(\theta^{A_2}_{min} - \theta^{cr}_s) & \text{case A} \\ K_A\theta^{A_2}_{min} & \text{case B} \\ K_A\theta^{A_2}_{min} & \text{case C} \end{cases} \tag{2.17}$$

and

$$\tau^{B_4} = \begin{cases} K_M\theta^{cr}_s + K_S(\theta^P - \theta^{A_2}_{min} - \theta^{cr}_s) & \text{case A} \\ K_M\theta^{cr}_s + K_S(\theta^P - \theta^{A_2}_{min} - \theta^{cr}_s) & \text{case B} \\ K_M(\theta^P - \theta^{A_2}_{min}) & \text{case C} \end{cases} \tag{2.18}$$

where case A: $\theta^{cr}_1 \leq \theta^P < 2\theta^{cr}_{max}$, case B: $\theta^{cr}_2 \leq \theta^P < \theta^{cr}_1$, and case C: $0 \leq \theta^P < \theta^{cr}_2$. θ^{cr}_1 and θ^{cr}_2 are the critical values of θ^P to differentiate different cases. θ^{cr}_{max} is the critical pre-deformation of the SMA torsion spring before any unrecoverable deformation occurs and is given by: $\theta^{cr}_{max} = \epsilon^{cr}_{max}/C_1$, where ϵ^{cr}_{max} is the critical strain approximately equal to 8% for low-cycle use of SMA made of Nitinol [85], which makes θ_{max}^{cr} equal to 6.5π for the presented SMA torsion springs. In our case, each spring is pre-tightened by 2.5π, so the springs always stay in the safe region. By substituting Equations (2.17) and (2.18) into Equation (2.16), $\theta_{min}^{A_2}$ is solved and the motion range is given by:

$$R_g = \begin{cases} \dfrac{(K_A - K_M)\theta_s^{cr} - \tau^c}{K_S} & \text{case A} \\ \dfrac{(K_A - K_S)\theta^P + 2(K_S - K_M)\theta_s^{cr} - 2\tau^c}{K_A + K_S} & \text{case B} \\ \dfrac{(K_A - K_M)\theta^P - 2\tau^c}{K_A + K_M} & \text{case C} \end{cases} \tag{2.19}$$

Note that K_M, K_A, K_S, and θ_s^{cr} are functions of N_0. By making the expression for case B equal to those for case A and case C, respectively, the critical pre-deformations can be solved as:

$$\theta_1^{cr} = \frac{(K_A - K_M + 2K_S)\theta_s^{cr} - \tau^c}{K_S} \tag{2.20}$$

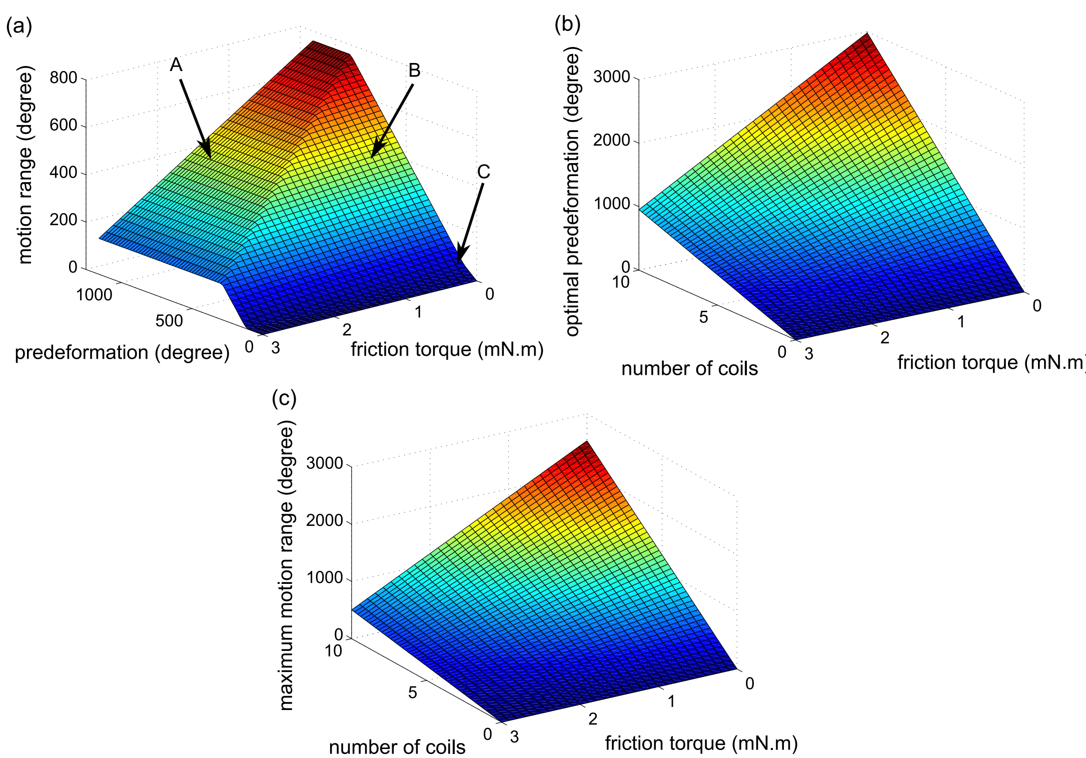

Figure 2.10: Simulation results: (a) full motion range against pre-deformation and friction torque, (b) optimal pre-deformation against spring turns and friction torque, and (c) full motion range against spring turns and friction torque when the pre-deformation is optimal.

and

$$\theta_2^{cr} = \frac{(K_A + K_M)\theta_s^{cr} + \tau^c}{K_A} \tag{2.21}$$

Case A in Equation (2.19) shows that the full motion range is constant if θ^P is equal to or larger than θ_1^{cr}, and cases B and C show that the full motion range monotonically decreases with reducing θ^P. Figure 2.10(a) shows the full motion range versus θ^P and τ^c when N_0 is equal to 3 in our system. It indicates that we can achieve the maximum full motion range when θ^P is equal to or larger than θ_1^{cr}, which is applicable to different N_0. Meanwhile, small pre-deformation is preferred, since it allows a large diameter of the rotation shaft to deliver tools through channel of the shaft. Therefore, θ_1^{cr} is regarded as the optimal pre-deformation. Figure 2.10(b) shows the theoretical optimal pre-deformation versus τ^c and N_0. It indicates that the optimal pre-deformation linearly increases with increasing N_0 under certain τ^c. Figure 2.10(c) shows the maximum full motion range versus N_0 and τ^c, if the optimal pre-deformation is adopted. It indicates that a larger full motion range can be achieved if there are more spring turns. Based on the estimated properties of the SMA torsion spring (see Table 2.4), the optimal pre-deformation in our system is estimated to be 4.2π. Since the current total pre-deformation is 6π, the theoretical motion process falls into case A, which validates the quasi-static model in Figure 2.8. In the design procedure, we can set the required motion range as the maximum full motion range and calculate the required N_0 using Equation (2.19) if τ^c is known. Afterwards, the optimal pre-deformation can be computed from Equation (2.20).

2.3 Torsion Module Characterization

This section presents the experimental characterization of the SMA torsion module to estimate the model parameters. The studies include the characterizations of the SMA torsion spring and the friction torque of the torsion module.

2.3.1 SMA Torsion Spring Characterization

The experimental setup for characterizing the SMA torsion spring is shown in Figure 2.11. An SMA torsion spring is fixed to the base of the platform at its bottom spring turn. The top spring turn is fixed to an adapter mounted on the shaft of an encoder (US Digital, Vancouver, WA, USA) to measure

Table 2.3: Characterization tests for SMA torsion springs

Test No.	Test Description	Characterized Parameters
1	Torque Free Test	A_s, A_f
2	Torsion Angle vs. Force Test	E_M, E_S, θ_s^{cr}, ϵ^{cr}
3	Heating Process of Block Test	E_A, C_A
4	Cooling Process of Block Test	M_s, M_f, C_M

the deformation angle of the spring. A pair of electrical wires are soldered to the top and bottom spring turns for Joule heating using a current amplifier (Maxon Motor, Sachseln, Switzerland). The electric current output can be controlled by modulating the analog voltage input to the amplifier. A resistance temperature detector (RTD) (Alpha Technics, Oceanside, CA, USA) is bonded with the middle section of the torsion spring using thermally conductive adhesive to measure the temperature of the spring. Due to the small spring size, temperature variance is assumed to be negligible in the spring. All digital and analog signals are communicated via a I/O board (Sensoray Co., Inc., Tigard, OR, USA) with a master computer. Based on this setup, four steps are performed to characterize the SMA torsion spring, as shown in Table 2.3.

Step 1 - Torque free test: The load cell (Transducer Techniques MLP-10) in Figure 2.11 is removed in this step. The torsion spring is pre-tightened to θ_d at room temperature. It will start recovering its initial configuration when it is heated above the transformation temperature. If the friction torque is negligible, the recovery angle can be derived using Equation (2.3) and is given by: $\theta = \theta_0 + \theta_L(\xi - 1)$, where θ_0 and θ_L are both equal to θ_d. Figure 2.12 shows the deformation angle

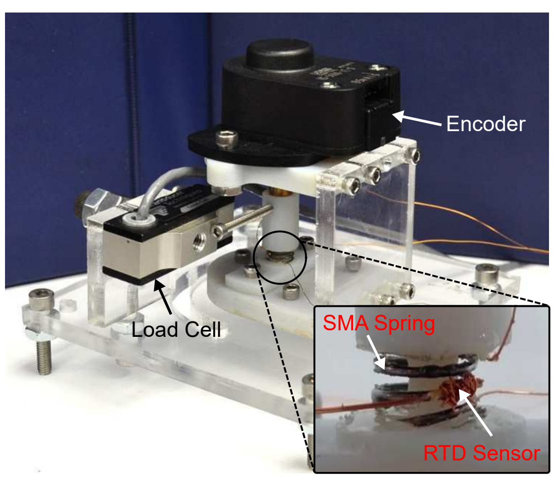

Figure 2.11: Experimental setup for the SMA torsion spring characterization.

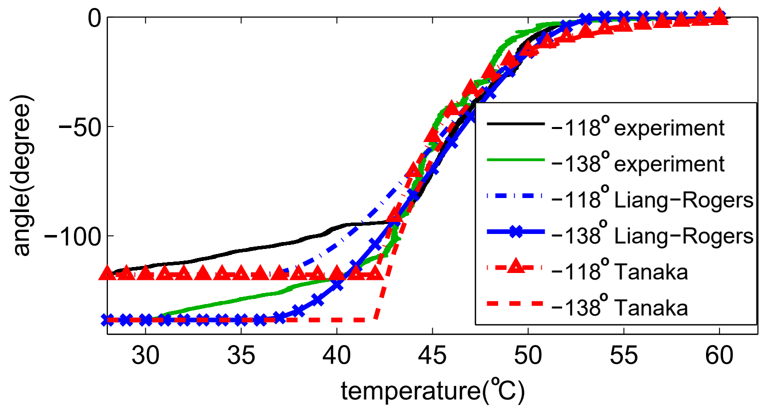

Figure 2.12: Rotation angle of the SMA torsion spring against temperature during the heating process compared to model predictions. RMSE is 9.5752° for Liang-Rogers model (A_s=36°C,A_f=54°C) and 14.8436° for Tanaka's model (A_s=42°C,A_f=60°C). R^2=0.9771 (-118°, Liang-Rogers), R^2=0.9860 (-138°, Liang-Rogers), R^2=0.9454 (-118°, Tanaka), and R^2=0.9653 (-138°, Tanaka).

Table 2.4: Results of SMA torsion spring characterization

Parameter	Value	Unit
A_s	36	°C
A_f	54	°C
M_s	53	°C
M_f	32	°C
E_M	30.035	GPa
E_A	96.375	GPa
E_S	7.847	GPa
C_A	95	MPa/°C
C_M	56	MPa/°C
ϵ_s^{cr}	0.0046	N/A
τ^c	0.0007	Nm

of the torsion spring for -118° and -138° pre-deformation. The least-square approach is used to fit the Liang-Rogers model and the Tanaka's model with the experimental data by searching for the optimal values of A_s and A_f. The results show that the Liang-Rogers model can fit the experimental results better. The estimated values of A_s and A_f are listed in Table 2.4.

Step 2 - Determination of E_M and E_S: The experimental setup is the same as the one in the first step, except that the bolt is used to apply a pushing force on the load cell by the SMA torsion spring. In this step, the relationship between the deformation angle and the pushing force is measured at room temperature. When $\xi = 1$ at room temperature, the governing Equation (2.3) is rewritten as: $E = \frac{C_2(F-F_0)L_l}{C_1|\theta-\theta_0|}$, where F is the force measurement of the load cell, F_0 is the initial force measurement when θ is equal to θ_0, and L_l is the leverage length of the bolt. By measuring the rate of force change before and after θ_s^{cr}, the values of E_M and E_S can be estimated. Figures 2.13 and 2.14 show the force measurements for these two cases, respectively. A linear model is used to fit the experimental data using the least-square approach and estimate the values of E_M and E_S. In Figure 2.14, the middle section from -400° to -300° is used for model fitting, since the stress initially increases at the rate of E_M from zero. The increased rate of force change when the angle is smaller than -400° is caused by the increased friction torque between the neighboring spring turns when the spring becomes very tight at large deformation angles. The intersection of the model fitting results of the two cases yields the critical angle, θ_s^{cr}, and ϵ_s^{cr} is calculated using Equation (2.7). The estimated values of E_M, E_S, θ_s^{cr}, and ϵ_s^{cr} are listed in Table 2.4.

Step 3 - Determination of E_A and C_A: In this step, block tests are adopted using the experimental same as the one in second step. The SMA torsion spring is pre-tightened and the pre-deformation is measured to be -85°. When the torsion spring is heated and tends to recover the initial shape, the load cell constrains its motion and measures the block force. The SMA torsion spring is heated to follow a temperature reference by modulating the electric current for Joule heating using a PI controller with the temperature feedback provided by the RTD temperature sensor. From Equation (2.3), the generated force is given by: $F = \frac{C_1|\theta_0|E(1-\xi)}{C_2 L_l}$, where ξ is described by Equation (2.4). When

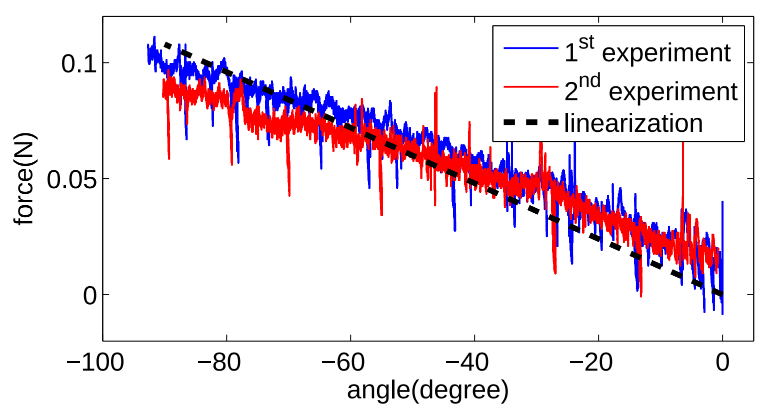

Figure 2.13: Force measurement versus rotation angle of the SMA torsion spring in the small-angle motion range at room temperature. RMSE is 0.0105 N. R^2 value is 0.8475 and 0.7421 for the 1^{st} and the 2^{nd} experiment, respectively.

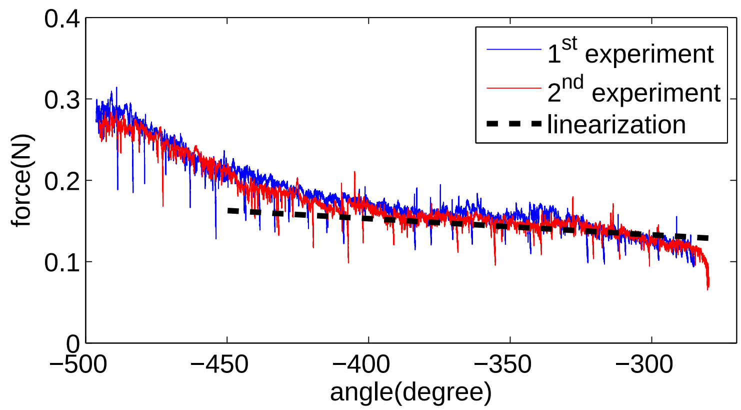

Figure 2.14: Force measurement versus rotation angle of the SMA torsion spring in the large-angle motion range at room temperature. RMSE is 0.0113 N. R^2 value is 0.6357 and 0.7532 for the 1^{st} and 2^{nd} experiment, respectively, in the range of -400° to -300°.

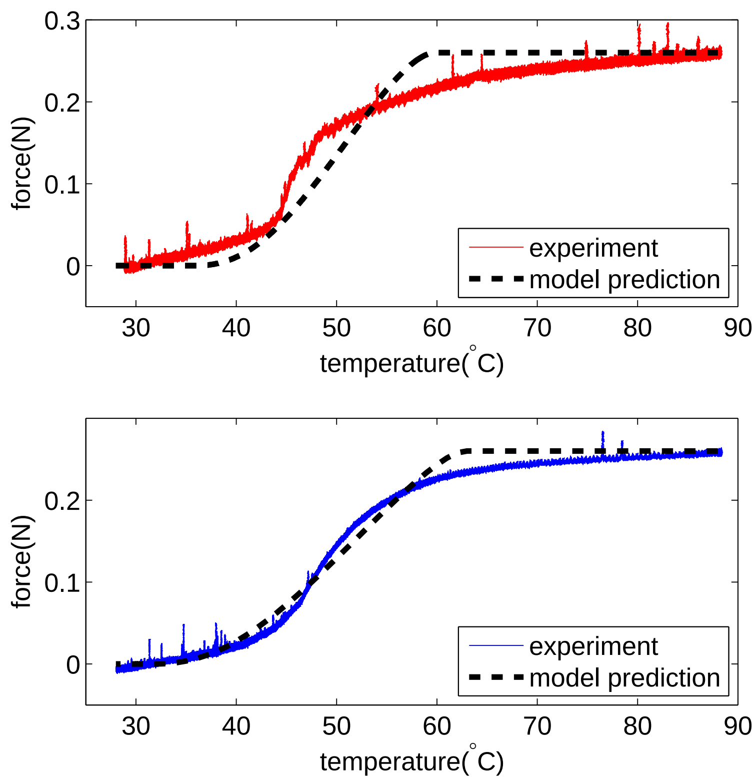

Figure 2.15: Block force measurement versus temperature of the SMA torsion spring: (a) SMA torsion spring is heated (RMSE is 0.0227 N and R^2 value is 0.9392) and (b) SMA torsion spring is naturally cooled after heating (RMSE is 0.0125 N and R^2 value is 0.9850).

$\xi = 0$, the generated force is the maximum an given by: $F_{max} = \frac{C_1|\theta_0|E_A}{C_2 L_l}$. Thus, E_A can be estimated by using the measurement of the maximum force. By using the least-square approach to fit the derived model with the force measurements, the value of C_A can be estimated. The values of E_A and C_A are listed in Table 2.4. The experimental results and model predictions are shown in Figure 2.15(a).

Step 4 - Determination of M_s, M_f and C_M: Since the shape of the SMA torsion spring will not change when the spring is cooled, the torque free test in the first step is not applicable in this step. Thus, we take advantage of the cooling process of the previous block test to estimate the values of M_s, M_f, and C_M by fitting the model using the least-square approach. In the cooling process, the expression of the generated force is the same as that during the heating process in the previous test, while ξ is described by Equation (2.5). Figure 2.15(b) shows the experimental results and the model predictions based on the fitted model when the SMA torsion spring is cooled following the test as described in Figure 2.15(a). The estimated values of M_s, M_f and C_M are listed in Table 2.4.

2.3.2 Friction Torque Characterization

The experimental setup for the friction torque characterization is shown in Figure 2.16. The shaft of the torsion module is fixed between two parallel plates on the stage. Two wooden sticks are respectively glued on the base disk and the torsion disk with two vision markers on each stick. A

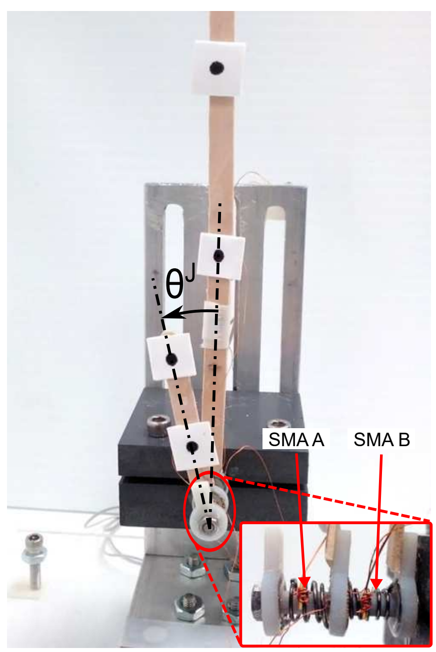

Figure 2.16: Experimental setup for characterizing the friction torque.

MicronTracker stereo camera (Claron Technology Inc., Toronto, Ontario, Canada) is used to track the four vision markers by Lucas-Kanade optical flow method [86]. The position of all markers is calculated using OpenCV libraries to calculate the orientation of both sticks. Using this approach, the rotation angle of the torsion module can be obtained. All vision-related processes are conducted on a slave computer.

The electrical wires for each SMA torsion spring are connected between the current source and a metal–oxide–semiconductor field-effect transistor (MOSFET) (Infineon, Neubiberg, Germany), which is controlled ON and OFF by the master computer via the I/O board. By turning one switch ON and the other switch OFF, the corresponding SMA torsion spring can be energized under the electric current supplied by the aforementioned power source. The temperature of each SMA torsion spring is measured using an RTD temperature sensor, and the measurement is fed to the master computer via the I/O board. The sampling time of the master computer is set as 15 ms to coordinate the serial communication with the slave computer.

The positive direction of the SMA torsion module is defined to be counter-clockwise, as shown in Figure 2.16. When SMA A is heated, the torsion module rotates clockwise and the rotation angle decreases, and vice versa when SMA B is heated. To generate a consistent home position, SMA B is heated to make the module rotate to the positive extremum and then cooled naturally to room temperature. The terminal angle is exclusively determined by the thermomechanical properties of the torsion module and assumed to be consistent for repeated tests. This characterization experiment includes two consecutive steps. In the first step, the torsion module is actuated by heating SMA A for ten minutes to follow a temperature reference, as shown in Figure 2.17, followed by a natural cooling process for five minutes. In the next step, the torsion module is actuated in the positive direction by heating and then cooling SMA B in the same way. The temperature of the SMA torsion spring in the heating process is controlled by a PI controller given by: $i_r = K_p^T e^T + K_i^T \int e^T dt$, where $e^T = T_r - T$, and i_r, T_r, T, K_p^T, and K_i^T are the electric current, temperature reference, temperature measurement, proportional gain, and integral gain, respectively.

The rotation angle of the torsion module is shown in Figure 2.18. It shows that the full motion range is 466°. The heating and cooling processes are slow to ensure a quasi-static motion of the torsion module. Figure 2.19 shows the temperature change for both SMA torsion springs. It shows

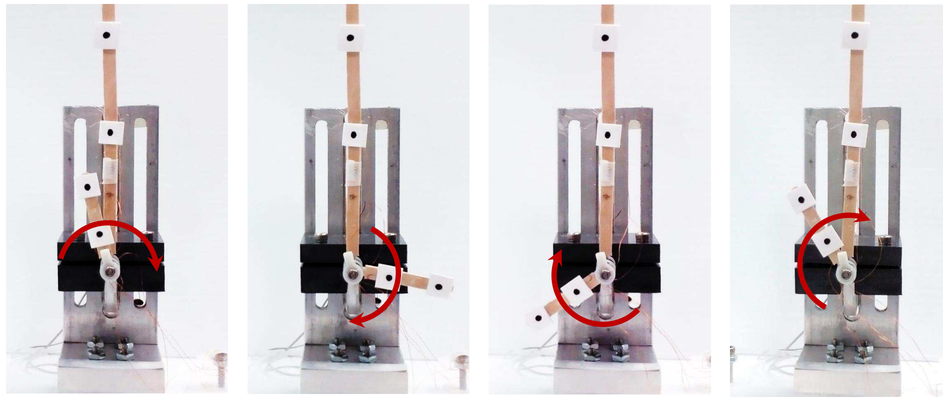

Figure 2.17: Snapshots of the torsion module moving clockwise as the arrow indicates when SMA A is heated.

that when one SMA torsion spring is heated, the temperature of the other increases slowly, probably due to the heat transfer between them via the ambient air and the device structure. From Figures 2.18 and 2.19, it is observed that the angular extremum is achieved when the temperature of the SMA torsion spring is about 70°C. Since the motion of the two steps are theoretically identical due to the same heating and cooling processes, only the heating and cooling processes for SMA A are used for friction torque characterization. The angle of the torsion module as a function of the temperature of SMA A is plotted in Figure 2.20. By applying the least-square approach, the quasi-static model is used to fit the experimental results. The estimated friction torque is listed in Table 2.4. As shown in Figure 2.20, the quasi-static model predicts the rotation angle of the SMA torsion module well.

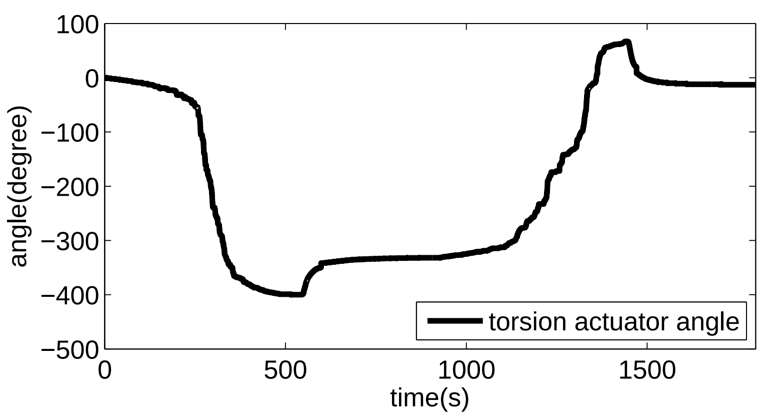

Figure 2.18: Rotation of the torsion module in one cycle.

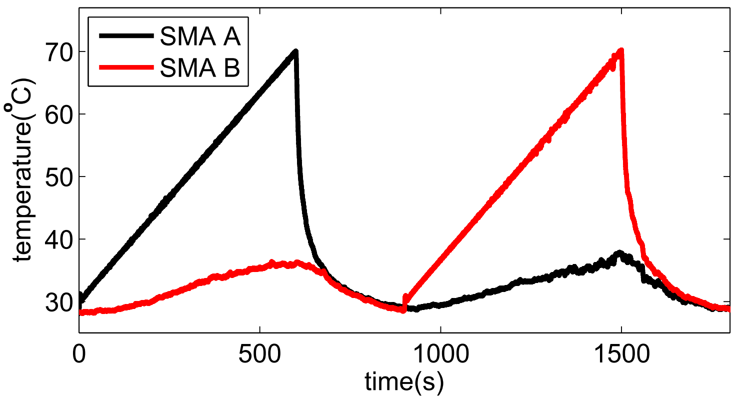

Figure 2.19: Temperature of the SMA torsion springs in one cycle.

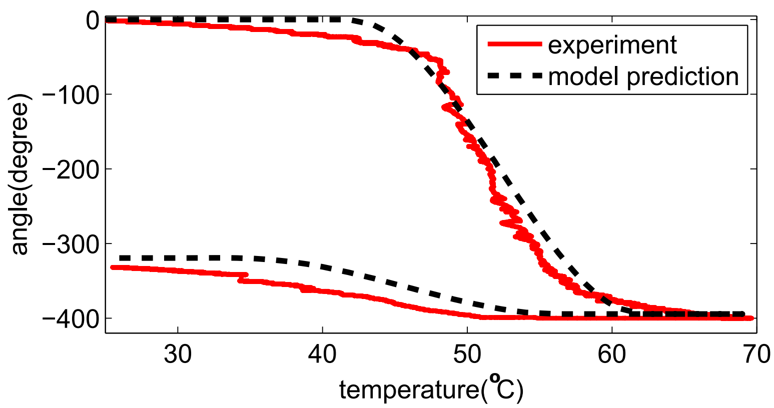

Figure 2.20: Rotation angle of the torsion module versus the temperature of SMA A when SMA A is heated and then naturally cooled (RMSE is 16.7588° and R^2 value is 0.9867).

2.4 Experimental Studies

2.4.1 Controller Design

To control SMA actuators, several linear and nonlinear controllers have been proposed to achieve precise tracking and disturbance rejection based on temperature or strain change feedback [87–89]. In the developed system, the measurable variables are the temperature of the springs and the rotation angle of the torsion module which is also the system output. Hence, we use a double-channel cascade PI controller (red and blue blocks) with feed-forward compensation (green block), as shown in Figure 2.21. The purpose of the double-channel controller is to promptly reduce tracking overshoot due to slow natural cooling by actively heating the antagonistic SMA element [87]. In Figure 2.21, the reference of the angular speed is assumed to be negative, so the feed-forward compensation

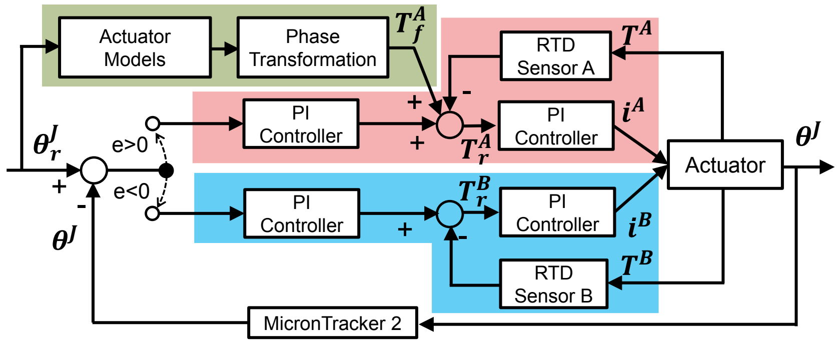

Figure 2.21: Block diagram of the double-channel cascade PI controller.

is applied on SMA A and SMA B is used to reduce overshoot. In the double-channel controller, a switching function determines which spring needs to be heated based on the output error given by: $e^J = \theta_r^J - \theta^J$, where e^J, θ_r^J, and θ^J are the error, reference, and measurement of the rotation angle, respectively. When $e^J < 0$, SMA A is continuously heated and SMA B is not heated. When $e^J > 0$, the controller stops heating SMA A and starts heating SMA B to suppress the overshoot of the rotation angle.

In the green block, the theoretical temperature is calculated as the feed-forward compensation based on the angular position reference and the quasi-static model. If the home position of both springs is known, the angular position reference for SMA A, θ_r^A, can be obtained based on θ_r^J, and the solution of ξ_r^A and τ_r^A can be solved using the quasi-static model. By substituting ξ_r^A and τ_r^A into the phase transformation Equations (2.4) and (2.5), the required temperature of SMA A, T_f^A, is obtained as the feed-forward compensation. In each channel, the first PI controller computes the temperature compensation based on the rotation angle feedback, and the control law is given by: $T_b = K_p^J|e^J| + K_i^J \int |e^J|dt$, where T_b is the temperature compensation, and K_p^J and K_i^J are the proportional gain and integral gain, respectively. The second PI controller computes the electric current required to track the temperature reference, T_r, and the control law is given by: $i_r = K_p^T e^T + K_i^T \int e^T dt$, where $e^T = T_r - T$, T is the temperature measurement, i_r is the current reference, and K_p^T and K_i^T are the proportional gain and integral gain, respectively. All the controller gains are tuned by trial and error.

2.4.2 Feedback Control Results

The experimental setup used for characterization, as shown in Figure 2.16, is used to evaluate the working performance of the torsion module.

Sinusoidal Tracking: The results of three sinusoidal tracking tests are shown in Figures 2.22(a) to (c). Since the developed model assumes a quasi-static motion, the feed-forward compensation is not applied in these relatively dynamic tests. When the tracking frequency is low (0.017 Hz and 0.025 Hz), the root-mean-square error (RMSE) is small and the performance is satisfactory. When the tracking frequency is increased to 0.05 Hz, phase shift is observed, primarily due to the output saturation of the current source. In the current system, the maximum electric current for Joule heating is set to be 1.9A. Thus, it is predictable that higher tracking frequency can be achieved if a more powerful current source is used and electrical wires with better heat resistance are adopted. Active cooling using water is also under consideration, since it has been proven to be beneficial to improving the bandwidth of SMA actuators [90]. The two channels are frequently switched when the measured rotation angle oscillates around the position reference and the sign of the tracking error frequently changes, resulting in the alternate spikes of heating current in Figures 2.22(a) to (c).

Step Input Response: The results of step input tests are shown in Figure 2.22(d). Since SMA B is heated when SMA A is at low temperature during the first several steps (0s to 65s in the upper case and 0s to 125s in the lower case), the antagonistic torque applied by SMA A is relatively small, so the response of the torsion module is fast with a rise time of about 4 s for the upper case and 2 s for the lower case. The rise time for the remaining steps increases and the longest rise time is about 20 s, since the antagonistic SMA torsion spring which is heated before the torsion module reverses is still at high temperature. Considering that most surgical procedures do not require high-speed motion, the torsion module can meet the application requirements, since the steady state error of each step diminishes to zero within finite time. Slight oscillation about $\pm 1.5^\circ$ occurs when the reference angle is 0° and 40°, probably due to the nonlinear dynamics of SMA springs. When the torsion module works in an environment with sufficient damping, the oscillation can potentially be suppressed. The feed-forward compensation is either not applied in these tests.

Quasi-Static Tracking: The proposed controller is evaluated by performing two quasi-static tracking tests. The position reference is a sinusoidal cycle and its period is as long as 600 s to

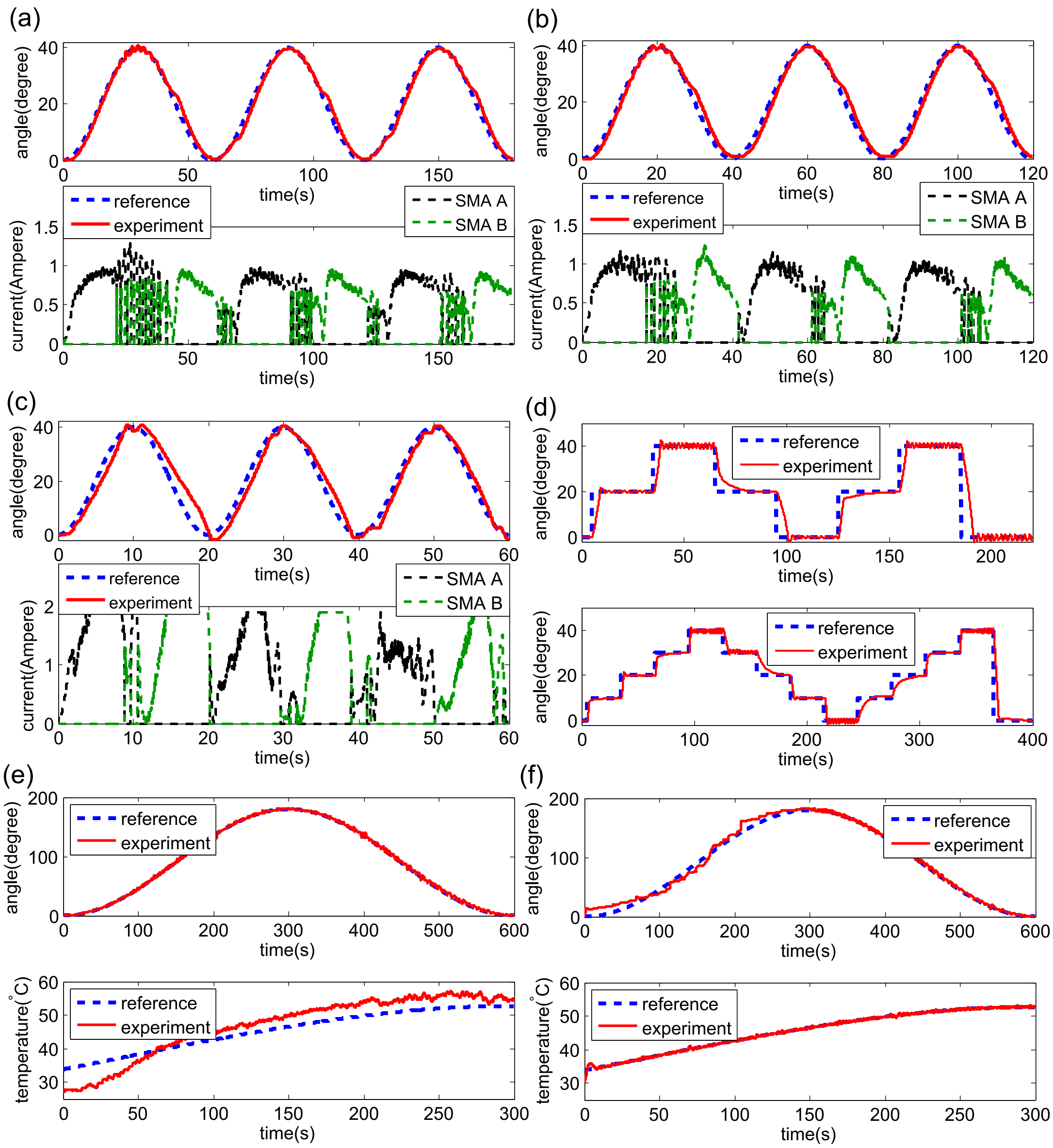

Figure 2.22: Experimental results: (a) Sinusoidal tracking at 0.017 Hz frequency (RMSE is 1.67°), (b) Sinusoidal tracking at 0.025 Hz frequency (RMSE is 2.05°), (c) Sinusoidal tracking at 0.050 Hz frequency (RMSE is 3.60°), (d) step input response with the time step of 30s and step size of 20° (upper) and time step of 30s and step size of 10° (lower), (e) Quasi-static tracking with both feed-forward and feedback compensation from 0s to 300s (RMSE is 1.86°) and only feedback compensation from 300s to 600s (RMSE is 2.24°), and (f) Quasi-static tracking with only feed-forward compensation applied from 0s to 300s (RMSE is 8.19°) and only feedback compensation applied from 300s to 600s (RMSE is 2.58°).

ensure a quasi-static motion. In the first test, both the feed-forward and feedback compensation are applied in the first half cycle and only the feedback compensation is applied in the second half cycle. Figure 2.22(e) shows negligible difference in the tracking error between these two halves, implying that the model-based feed-forward compensation cannot improve the tracking performance significantly. However, the feed-forward compensation shows its significance when the motion feedback system is unavailable. Since it is challenging to incorporate miniature encoders, vision feedback is usually used. But since vision systems are not robust, it is very likely that visual features are lost due to occlusion during procedures. Thus, in the second test, only the feed-forward compensation is applied in the first half cycle, which simulates a failure of the vision system, and only the feedback compensation in the second half cycle, which simulates a recovery of the vision system, due to model uncertainties, such as the temperature change in the antagonistic spring and unmodeled deformation of spring turns. Although the tracking error is larger than that in the second half cycle, we can effectively avoid unpredictable rotation when the vision system fails. When only the feed-forward compensation is applied, the torsion module works in the open-loop mode and the relatively small tracking error also validates the derived quasi-static model. In both cases, the feed-forward compensation is only applied in the first half cycle, since the derived model assumes that the antagonistic spring is at room temperature, which is invalid in the second half cycle as the antagonistic spring still maintains a relatively high temperature after being heated in the first half cycle.

2.4.3 Proof-of-Concept Demonstration

Figure 2.23(a) shows the setup for the gelatin evacuation demonstration. A digital electrosurgery generator (Bovie Medical Corp., Melville, NY, USA) is used to provide the electocautery tips with electric current to cauterize the gelatin tissue around the robot tip. A suction device (Invacare Corp., Elyria, OH, USA) is used to remove the cauterized tissue through a drainage tube and store it inside a sealed cup, as shown in Figure 2.23(b). The demonstration includes the following steps. First, the robot is manually inserted into the gelatin until its tip reaches the red core. After the robot is fixed by a support device, the bending tip deflects and the robot tip rotates within the red core by actuating the SMA bending tip and the SMA torsion module. Meanwhile, the electrocautery tips are energized to cauterize the gelatin tissue and the aspirator removes the melted tissue. The snapshots

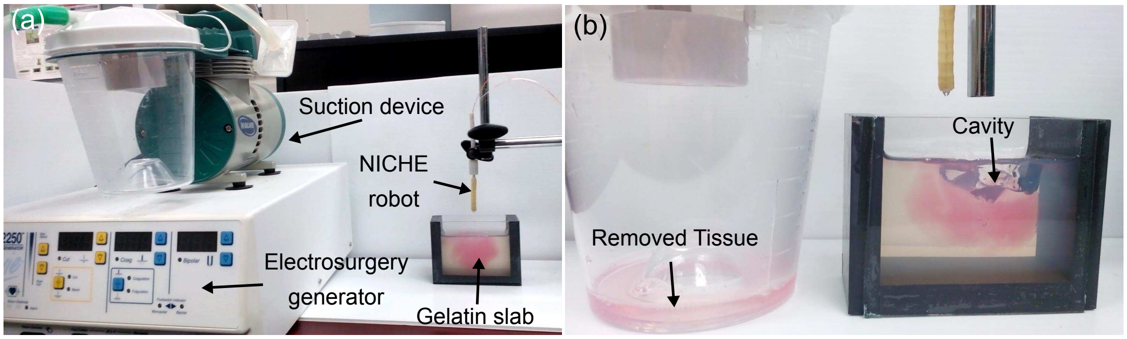

Figure 2.23: Experimental setup for the gelatin evacuation demonstration: (a) NICHE robot connected to a suction device and a electrosurgery generator and (b) gelatin evacuated from the slab and transferred into the cup.

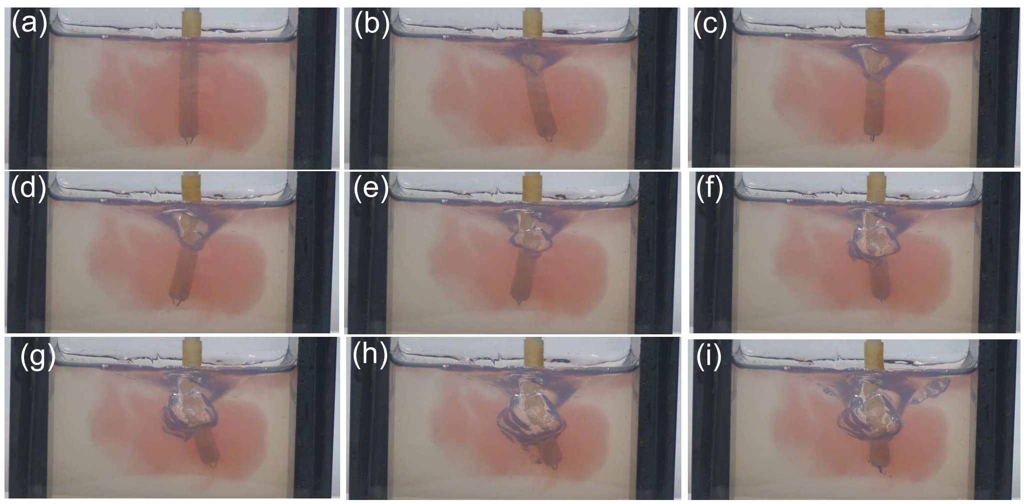

Figure 2.24: Snapshots of the gelatin evacuation demonstration with (a) and (b) showing the deflection of the bending tip and (b)→(i) showing the articulation of the end effector.

of this process are shown in Figure 2.24. Since after a volume of tissue is removed, the gelatin tissue above it will fill up the empty space due to gravity, a cavity is gradually formed starting from the top surface of the gelatin slab.

2.5 Discussion and Conclusions

In this chapter, an innovative SMA torsion module is proposed based on SMA torsion springs to develop a meso-scale neurosurgical robot for intracerebral hemorrhage evacuation. Due to the alternate shape recovery of two antagonistic, tightened SMA torsion springs at high temperature, a compact torsion module is developed. All the electric components are enclosed inside the module for insulation. The SMA torsion module is analytically modeled to find out the optimal pre-deformation of the springs and achieve the maximum motion range. The model parameters can be experimentally characterized so that a feedback controller with model-based feed-forward compensation can be implemented. Several experimental studies are conducted to evaluate the working performance of the torsion module. The positioning accuracy of the NICHE robot is estimated to be 0.7 mm by multiplying the low-speed tracking error of about 2° (see Figure 2.22) and the maximum rotation radius of about 20 mm (see Figure 2.6). This accuracy is comparable to the accuray of commercial neurosurgical systems, such as the Stealth^{TM} Navigus^{TM} system [81]. The module is able to rotate by more than 360°, but the motion range becomes smaller in gelatin phantom due to the external loading applied by gelatin tissue and the cooling effect of gelatin tissue. The NICHE robot is developed by integrating the SMA torsion module with an SMA bending tip and a rigid stem. All the structural components are 3D-printed in bio-compatible plastic material to enable a disposable, bio-compatible robotic system. By equipping the robot with a suction tube and electrocautery tips at the end effector, the NICHE robot is able to perform evacuation procedures.

CHAPTER 3

LOW-CURRENT SMA BENDING MODULE

The SMA torsion and bending modules for meso-scale surgical robotics are presented in the previous chapter. However, the electric current required for SMA actuation is high. To improve the system safety and enable an MRI-compatible robotic system, this chapter will present a conductive heating actuation technique to significantly reduce the requirement of electric current. This technique is applied on the SMA bending modules to develop an MRI-compatible robotic catheter for atrial fibrillation (AFib), which is a common heart-related health problem among American population [91]. In related works, the positioning error of the SMA bending module under vision-based feedback control is less than 0.5° [23].

AFib is primarily caused by ectopic electrical discharge from pulmonary veins (PVs) in the left atrium (LA) [92]. Therefore, a radiofrequency (RF) ablation procedure can potentially treat AFib by ablating the tissue around PVs and blocking ectopic electrical signals [93, 94]. However, it is challenging to precisely manipulate a completely passive catheter in the confined atrium to perform the ablation procedure. Multiple trials involving insertion, retraction, and base rotation have to be performed to reach an ablation target and apply appropriate contact force [94]. To overcome this challenge, tendon-driven mechanisms have been applied to develop commercially available catheters with steerable tips [95, 96]. However, the coupling effect of tendon-driven mechanisms has made it very challenging to develop a steerable catheter with high DoFs.

The rest of this chapter is organized as follows. Section 3.1 presents the design and fabrication of the low-current SMA bending module and the robotic catheter. Section 3.2 models the magnetic and thermomechanical properties of the low-current SMA bending module. Section 3.3 presents several experimental studies to evaluate the developed bending module and robotic catheter. Section 3.4 concludes the chapter.

3.1 Hardware Development

This section presents the hardware development of the low-current SMA bending module and the robotic catheter. I would like to acknowledge Dr. Xuefeng Wang, currently an Assistant Professor at the University of Alabama, Tuscaloosa, for collaborating on the design and fabrication of the low-current SMA bending module.

3.1.1 Bending Module Design

The robotic catheter based on SMA bending modules is comprised of a flexible stem and a steerable tip covered by an 3D-printed elastomeric sleeve, as shown in Figure 3.1. The flexible stem is a 9 French outer diameter braid-reinforced tube with high flexibility and kink resistance (Duke Extrusion, Santa Cruz, California, USA). The steerable tip consists of multiple SMA bending modules, as shown in Figure 3.2(a). Each SMA bending module is made of a pair of 190 μm diameter SMA wires bonded between two rigid module links, as shown in Figures 3.2(b) to (d). Each link has an outer diameter of 2.9 mm and possesses a 1.3 mm diameter through channel. Since the two SMA wires bend antagonistically when they tend to recover their memorized curved shapes at high temperature, the bending module can be actuated bi-directionally by individually heating each SAM wire. When two SMA bending modules are assembled together via protrusions and recesses on adjacent module links, these two modules bend in two orthogonal directions, as shown in Figure 3.2(b). If a positive adapter is utilized, the length of the steerable tip can be adjusted, as shown in Figure 3.2(c). If a negative adapter is assembled between two SMA bending modules, these two modules can bend in the parallel direction, as shown in Figure 3.2(d).

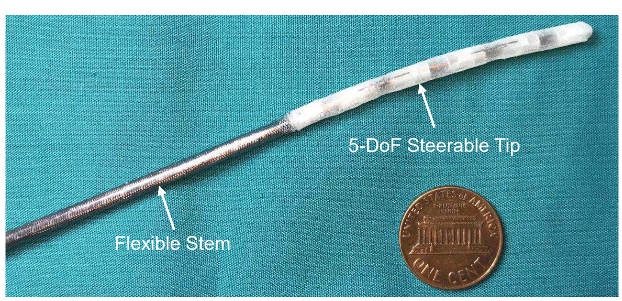

Figure 3.1: Robotic cardiac catheter consisting of a flexible stem and a steerable tip.

To develop a reliable SMA bending module and an MRI-compatible robotic catheter, the technique of conductive heating actuation is proposed. As shown in Figure 3.2(e), a 30 μm diameter enameled nichrome wire is folded into two strands and tightly routed around the bending segment of the SMA wire to form nichrome coils. By applying electric current to the nichrome coils, the temperature of the nichrome coils will increase due to Joule heating. Meanwhile, the temperature of the SMA wire wrapped within the nichrome coils will increase as well due to conductive heat transfer between the nichrome coils and the SMA wire. Due to the high resistivity and small cross-section of the nichrome wire, the electric current required for energizing the SMA wire is very low. Since the electromagnetic fields induced by the two nichrome strands containing opposite electric current are small and canceled by each other, the MRI-compatibility of the SMA bending module can be significantly improved. Due to the low electric current, ultra-thin enameled magnet wires (44 AWG) can be soldered to the nichrome coils for supplying electric current. As a result, sufficient free space is allowed inside the catheter channel to pass through surgical tools when multiple SMA bending modules are integrated to form a multi-DoF steerable tip. The SMA training procedure is the same as that presented in Section 2.1.4. The memorized shape of the SMA wire is 90° for a curvature of 149.25 m^{-1}.

3.1.2 Bending Module Fabrication

A set of jigs are designed and 3D printed to route the nichrome wire around the bending segment of the SMA wire, as shown in Figure 3.3(a). Both the upper frame and the lower frame contain an array of teeth with a groove along its axis. When they are assembled face to face, the space between the teeth form a helical routing path with a 800 μm pitch, and a channel goes through the center. To route the nichrome wire, the straight segment at one end of the SMA wire is fixed inside the groove of the base frame using the fixture, a bolt, and a nut, as shown in Figure 3.3(a). By manually straightening the bending segment using pliers, the straight segment at the other end of the SMA wire is fixed in the same way. Afterwards, the upper frame and lower frame are attached to the base frame, so that the bending segment of the SMA wire is constrained inside the channel between the two frames. Meanwhile, a nichrome wire is folded into two strands and tied onto the tip of a 90 μm diameter superelastic wire at the folding point. After taping the two ends of the nichrome

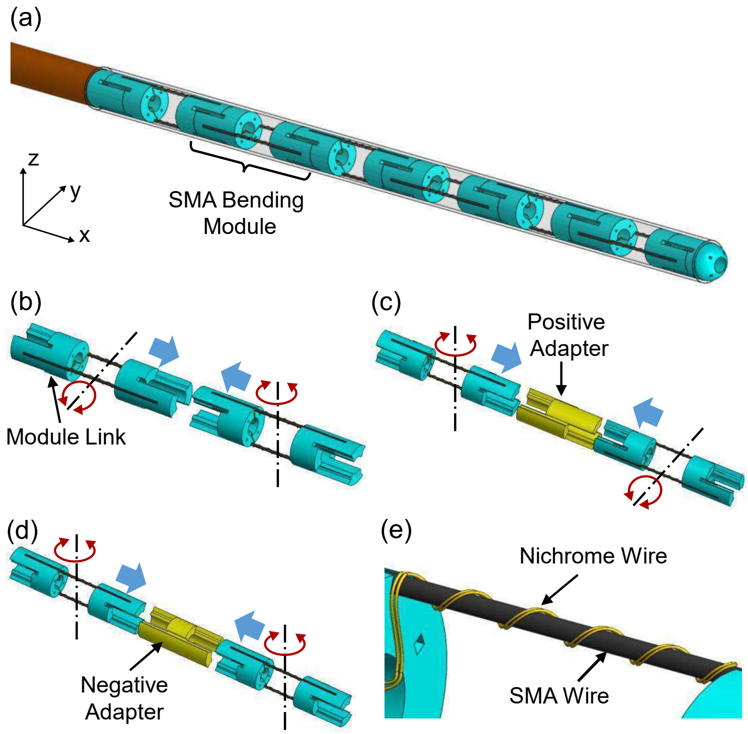

Figure 3.2: Design of the robotic catheter: (a) steerable tip comprised of multiple SMA bending modules, (b) assembly of two bending modules with orthogonal bending directions, (c) assembly of two bending modules via a positive adapter, (d) assembly of two bending modules via a negative adapter, and (e) nichrome coils routed around an SMA wire of the bending module. The red arrows show bending directions and the blue arrows show assembly directions.

wire on the base frame, the superelastic wire with the nichrome wire is repeatedly passed through the space between adjacent teeth and routed around the SMA wire along the helical path, as shown in Figure 3.4(a). Appropriate pulling force is applied to the superelastic wire after it passes through the teeth each time, so that a series of nichrome coils are tightly wrapped around the SMA wire. In the end, the upper frame and lower frame are removed, and super glue is applied to fix the nichrome coils on the SMA wire.

To assemble two SMA wires with nichrome coils onto two module links in an antagonistic way, two sets of assembly jigs are developed. As shown in Figure 3.3(b) and Figure 3.4(b), a module link is fixed between a base frame and a coupler. The grooves on the link for fixing the SMA wires face upward and downward, respectively, by matching the protrusions of the link to the recess of the coupler. Meanwhile, the SMA wires are heated by a heat gun to recover their memorized curved configurations. By fitting the straight segment at one end of each SMA wire into the link groove, pressing the upper frame and lower frame into the flat recess on the base frame, and applying epoxy adhesive to the link grooves, the two SMA wires can be fixed onto the link in an antagonistic way. After removing the module link from the base frame, the bending segments of the two SMA wires on the module are manually straightened and the module link is assembled to a coupler, as shown in Figure 3.3(c). Afterwards, the left frame and right frame are assembled together with the coupler to fit the SMA wires into the grooves formed between the two frames. After assembling the other module link and the other coupler and pressing the SMA wires into the grooves on the module link, as shown in Figure 3.4(c), epoxy adhesive is applied to fix the SMA wires. The fabrication is completed by removing the jig sets after the adhesive cures, as shown in Figure 3.4(d).

3.2 Actuator Modeling

3.2.1 Electromagnetic Field

When an electric current is applied to a metallic wire, such as an SMA wire or a nichrome wire in our study, the induced electromagnetic field at a spatial point is given by [97]:

$$\boldsymbol{B}(\boldsymbol{r}) = \frac{\mu_0}{4\pi}\int\left[\frac{\boldsymbol{J}(\boldsymbol{r}', t_r)}{|\boldsymbol{r}-\boldsymbol{r}'|} + \frac{1}{c}\frac{\partial \boldsymbol{J}(\boldsymbol{r}', t_r)}{\partial t}\right] \times \frac{(\boldsymbol{r}-\boldsymbol{r}')}{|\boldsymbol{r}-\boldsymbol{r}'|^2}\mathrm{d}^3\boldsymbol{r}' \tag{3.1}$$

where $\boldsymbol{r}$, $\boldsymbol{r}'$, $\boldsymbol{J}$, t, and c represent a point in the world space, a point along the electric current flow, current density, time, and speed of light, respectively. t_r is the retarded time and it is given by: $t_r = t - \frac{\boldsymbol{r}-\boldsymbol{r}'}{c}$. Equation (3.1) indicates that the magnetic field is caused by the current density and

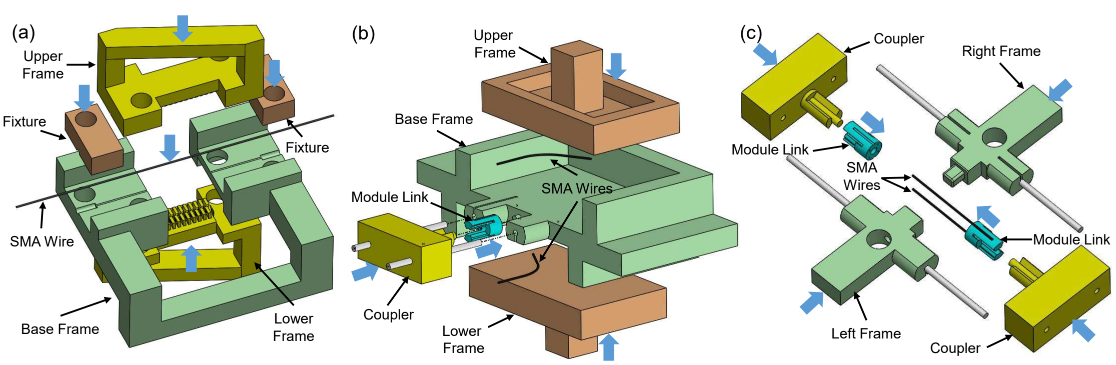

Figure 3.3: Fabrication of the SMA bending module: (a) fixing an SMA wire onto the jigs followed by routing a nichrome wire, (b) assembling two SMA wires to a module link, and (c) connecting the module link with SMA wires to another link. The blue arrows indicate assembly directions.

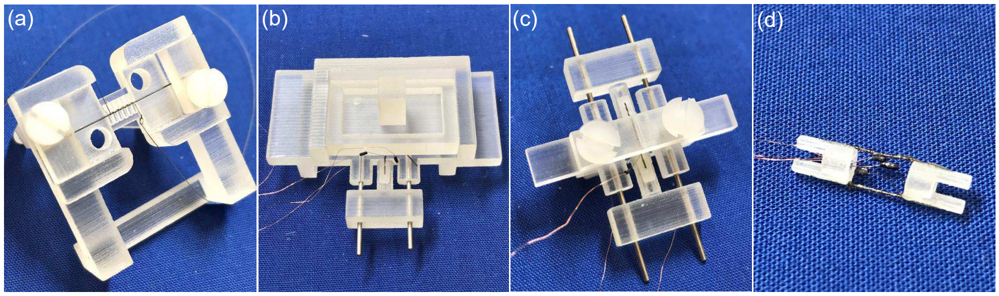

Figure 3.4: Photos showing the fabrication of the SMA bending module: (a) nichrome wire routed around the SMA wire, (b) two SMA wires assembled with one module link, (c) assembling another module link, and (d) prototype of the SMA bending module.

current density variation. When the SMA bending module is manipulated within a cardiovascular system under intra-operative MRI guidance, the distance from the region of interest (ROI) to the bending module is within several centimeters. Therefore, when the current density is modulated by a control system, we have:

$$\frac{1}{c}\frac{\partial \boldsymbol{J}}{\partial t} \leq \frac{2\boldsymbol{J}}{ct_s} \ll \frac{\boldsymbol{J}}{|\boldsymbol{r}-\boldsymbol{r}'|} \tag{3.2}$$

where t_s is the time step for the digital control system. From Equations (3.1) and (3.2), the magnetic field generated by the current density variation is negligible, since it is much smaller than that generated by the current density. Thus, for a metallic wire under direct Joule heating, the magnetic field magnitude around it is given by: $B_m = \frac{\mu_0 I}{2\pi d}$, where μ_0, I, and d are the permeability of free space, electric current magnitude, and the shortest distance to the SMA wire from a spatial point, respectively. In preliminary studies, up to 2 A electric current is required to actuate an SMA bending module under direct Joule heating actuation in water at room temperature. However, the same bending module with nichrome coils under conductive heating actuation requires much lower current, which will be presented in the following sections. Therefore, the strength of the induced electromagnetic field is significantly reduced. Meanwhile, the nichrome coils work as a solenoid to constrain the electromagnetic field inside the SMA wire. Since the nichrome coils are made of a folded nichrome wire containing two strands, the electric current flows are opposite to each other in the two parallel strands and the induced electromagnetic fields cancel each other, further reducing the overall strength of the magnetic field around the SMA bending module.

3.2.2 Heat Transfer

To model an SMA wire with nichrome coils under conductive heating actuation, a few assumptions are made: a) The individual temperature of the nichrome coils and SMA wire is homogeneous; b) Heat is dissipated into air through free convection at room temperature; c) The thermal effect of super glue is negligible due to its negligible volume. The length of the nichrome wire around an SMA wire of a unit length, l_r, is given by: $l_r = 2\sqrt{p_r^2 + \pi^2 d_s^2}/p_r$, where p_r and d_s are the pitch of the nichrome coils and SMA wire diameter, respectively. The heat generated on the nichrome coils is transferred to the SMA wire via contact conductance in addition to raising the temperature of the nichrome coils and the dissipation into air. Thus, the heat transfer model for nichrome coils is given by:

$$\frac{16\beta_r I^2}{\pi^2 d_r^4 C_r \rho_r} = \dot{T}_r + \frac{4h_a(T_r - T_a)}{d_r \rho_r C_r} + \frac{4h_c(T_r - T_s)}{\pi d_r \rho_r C_r} \tag{3.3}$$

where T_r, T_a, h_a, d_r, ρ_r, C_r, β_r, I, T_s, and h_c are the temperature of nichrome coils, air temperature, heat convection coefficient for free air, nichrome wire diameter, nichrome density, specific heat capacity of nichrome, nichrome resistivity, heating current, SMA wire temperature, and the coefficient of thermal contact conductance, respectively. The heat transferred to the SMA wire via contact conductance increases the SMA wire temperature and induces SMA phase transformation in addition to the dissipation into air [90, 98, 99]. By assuming the contact area between the nichrome coils and the SMA wire of a unit length is equal to $2l_r d_r$, the heat transfer model for the SMA wire is given by:

$$\frac{8h_c l_r d_r (T_r - T_s)}{\pi d_s^2 \rho_s C_s} = \dot{T}_s + \frac{4h_a(T_s - T_a)}{d_s \rho_s C_s} + \frac{L_s \dot{\xi}}{C_s} \tag{3.4}$$

where ρ_s, C_s, L_s, and ξ are the SMA density, specific heat capacity of SMA, latent heat of phase transformation, and martensite volume fraction of SMA, respectively. The value of h_c depends on the contact force between the SMA wire and nichrome coils, and it is influenced by the applied super glue. Therefore, it needs to be experimentally estimated.

3.2.3 SMA Constitutive Model

The Liang-Rogers model is used to model the thermomechanical properties of the SMA bending module. As the strain change induced by thermal expansion is negligible, the SMA constitutive model is given by [83]:

$$\sigma - \sigma_0 = E(\epsilon - \epsilon_0) - \epsilon_L E(\xi - \xi_0) \tag{3.5}$$

where σ, ϵ, E, and ϵ_L are the SMA stress, strain, Young's modulus, and maximum recoverable strain, respectively. The subscript '0' denotes the initial condition. E is given by: $E = E_A + \xi(E_M - E_A)$, where E_M and E_A are the Young's modulus values in the austenite state (A) and martensite state (M), respectively. The martensite volume fraction, ξ, during SMA heating is given by:

$$\xi = \frac{\xi_0}{2}\{cos[\frac{\pi}{A_f - A_s}(T_s - A_s - \frac{\sigma}{C_A})] + 1\} \tag{3.6}$$

where A_s and A_f are the transformation start and finish temperatures for the heating process, respectively. C_A is the stress influence coefficient.

3.3 Experimental Studies

3.3.1 Fatigue Tests

To evaluate the working performance of the SMA bending module and the durability of the super glue as a bonding layer between the SMA wire and nichrome coils, a series of fatigue tests are conducted. As shown in Figure 3.5(a), one link of a SMA bending module is fixed onto a fixture with two vision markers and a moving link with another two vision markers is fixed onto the other

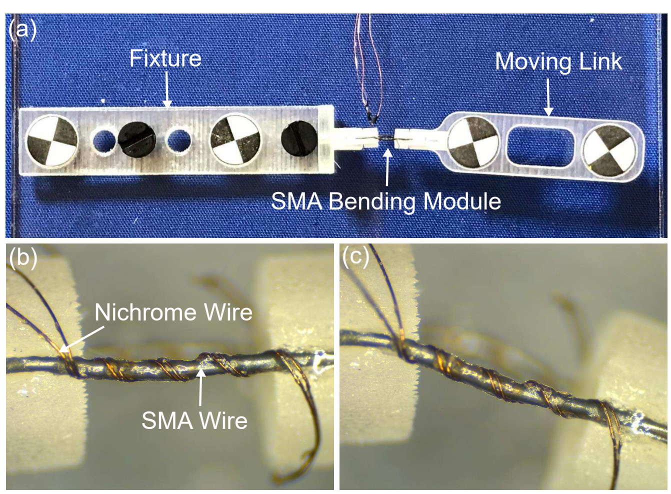

Figure 3.5: Fatigue tests of the SMA bending module: (a) experimental setup, (b) microscopic view before actuation, and (c) microscopic view before actuation after 200 cycles.

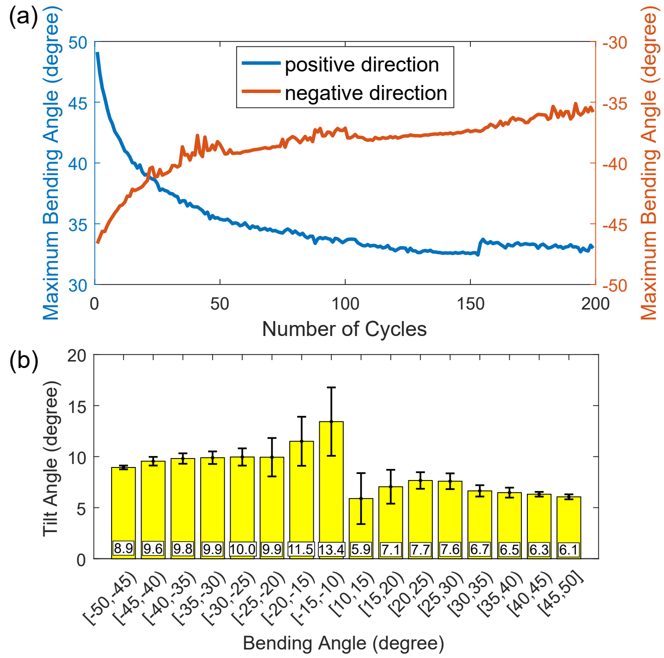

Figure 3.6: Experimental results of fatigue tests: (a) maximum bending angles versus bending cycles and (b) twist angles of the SMA bending module versus bending angles.

link of the bending module. Meanwhile, a MicronTracker stereo camera (Claron Technology Inc., Toronto, Ontario, Canada) is used to track the position of the four vision markers to compute the bending angle of the bending module. By alternately applying 40 mA current for 5 s to the nichrome coils around the upper SMA wire and the lower SMA wire with a 30 s natural cooling interval between two heating periods, the bending module is actuated bi-directionally for repeated cycles. A stereo microscope (Model S6D, Leica, Wetzlar, Germany) is used to examine the SMA wire with nichrome coils. It is observed that the nichrome coils are still tightly bonded with the SMA wire after 200 cycles, as shown in Figures 3.5(b) and (c). These tests have demonstrated that super glue can be used as a reliable bonding agent between the SMA wire and nichrome coils, due to the high service temperature up to 82°C and flexibility of the super glue. It is assumed that the surgical procedures where the SMA bending module is used, can be completed by actuating it for far fewer than 200 cycles. Thus, the developed SMA bending module is robust.

Figure 3.6(a) shows the maximum bending angles versus bending cycles at 40 mA heating current. The maximum bending angle decreases significantly in the first 50 cycles and converges to a stable value of about 33° and 35.5° for the actuation of the lower and upper SMA wires, respectively. This is primarily due to the change of the thermomechanical behavior of SMA during cyclic loading [100], which causes the accumulation of dislocations around defects in SMA microstructure and results in an increase of residual martensite volume fraction and a decrease of stress during forward phase transformation (M $\rightarrow$ A). It is also observed that the bending module twists when it deflects. To define the twist angle, the vision markers on the moving link are projected to the plane perpendicular to the vector through the vision markers on the fixture. The twist angle is the angle between the horizontal plane and the vector through the two projection points. Figure 3.6(b) shows the twist angles of the bending module versus the bending angles. Since the straight configuration is a geometric singularity for computing the twist angle, the computation of the twist angle when the bending angle is close to 0 has a relatively large error due to the limited tracking precision of the stereoscopic camera. Thus, the twist angles for the bending angles from -10° to 10° are not shown. It is observed that the average twist angle is about 11.4° and 6.7° for the negative (upper SMA wire) and positive bending (lower SMA wire), respectively. In addition to the moment arm from the bending force to the link axis, the twisting is also caused by the uncertainty when aligning SMA wires during fabrication, as shown in Figures 3.3(b) and (c).

3.3.2 SMA Actuation Comparison

In the second study, the SMA bending module under conductive heating actuation is compared with the same module under direct Joule heating actuation in terms of their heating and cooling response. The experimental setup is shown in Figure 3.7(a). After the bending module consisting of one SMA wire is manually set in a straight configuration, one link of the bending module is fixed onto a fixture and the other link is bonded with an adapter with a conic tip on the side to press a load cell. When the SMA wire is thermally actuated, the recovery motion of the bending module is blocked by the load cell and the block force is measured. In the first case, electric current from 10 mA to 20 mA with a 5 mA step and from 20 mA to 38 mA with a 2 mA step is applied to the nichrome coils around the SMA wire for 40 s, followed by a 40 s natural cooling period. In the second case, electric current from 0.1 A to 0.9 A with a step of 0.1 A is applied to the SMA wire for direct Joule heating actuation for 40 s, followed by a 40 s natural cooling period. Each test was repeated by three times. Figures 3.7(b) and (c) show the change of the block force for these two cases at several typical current levels. It is observed that the electric current required for conductive heating actuation is about 20% of that required for direct Joule heating actuation to achieve the same level of stable block force.

By defining the time required to achieve 63% of the maximum force increase during heating and 63% of the maximum force drop during cooling as the heating time and cooling time, respectively, the average heating time and cooling time with standard deviations for four groups of stable block force are shown in Figures 3.8(a) and (b). It is observed that the conductive heating actuation requires more heating time, probably due to the large nichrome coil pitch in the current design. Since the electric current required for the conductive heating actuation is much smaller, the heating response can potentially be improved by increasing the electric current. The cooling time for the

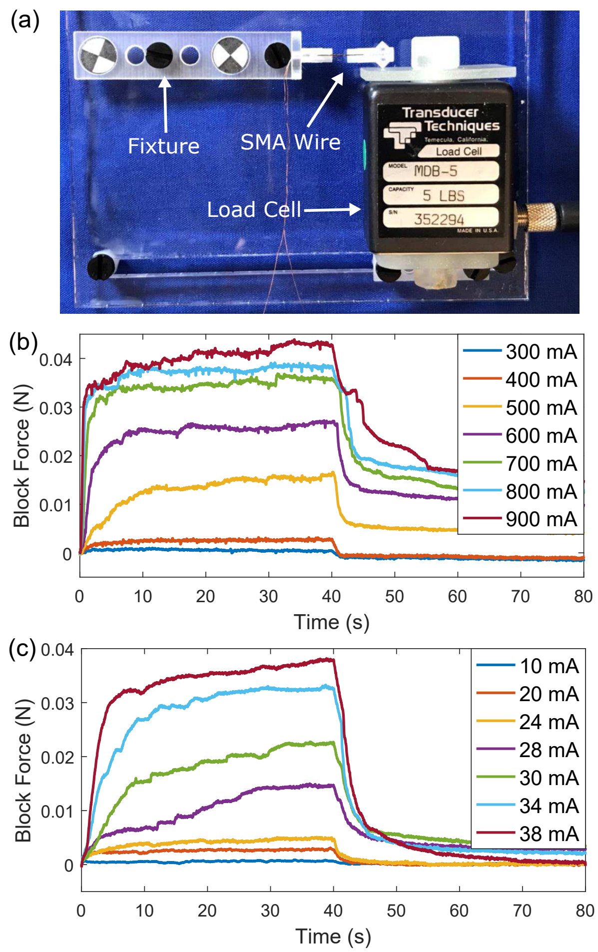

Figure 3.7: Comparison between Joule heating actuation and conductive heating actuation: (a) experimental setup to measure the block force, (b) block force under Joule heating actuation, and (c) block force under conductive heating actuation.

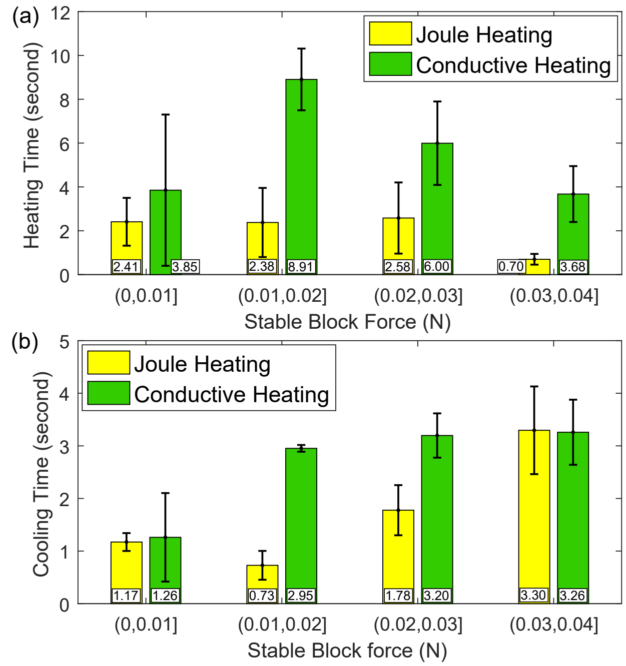

Figure 3.8: Comparison between Joule heating actuation and conductive heating actuation in terms of heating response (a) and natural cooling response (b).

conductive heating actuation is slightly longer than that for the direct Joule heating actuation, probably due to the larger heat capacity of the SMA wire with nichrome coils and the impediment of natural convection by super glue.

3.3.3 Estimation of Contact Conductance Coefficient

Since the training method for the SMA wire is the same as the method presented in the related work [23], the parameter values of the SMA constitutive model are taken from this work and listed in Table 3.1 with geometric parameters. For the heat transfer model, the value of the heat convection coefficient in free air, h_a, is approximately equal to 5 W/(m^2·K) [101]. To estimate the conductance coefficient between the SMA wire and nichrome coils, h_c, an experiment is performed. The experimental setup is similar to Figure 3.5(a), except that the bending module is only equipped by one SMA wire with nichrome coils. The bending module is heated by a heat gun to deflect to the maximum bending angle which is measured by the stereoscopic camera. Afterwards, the bending module is manually straightened. By applying electric current to the nichrome coils for 20 s at different current levels, the SMA wire bends to different stable angles at different current levels

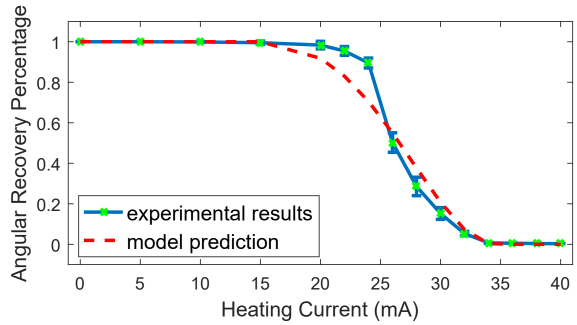

Figure 3.9: Angular recovery percentage of the SMA wire versus electric current applied to the nichrome coils. RMSE and R^2 value of the experimental results with respect to the model prediction are 0.0704 and 0.9775, respectively.

Table 3.1: Properties of SMA wire and nichrome wire

variable	value	unit	variable	value	unit
d_r	0.03	mm	A_s	31.5	°C
d_s	0.19	mm	A_f	64.5	°C
p_r	0.8	mm	C_A	30	MPa/°C
h_a	5	W/(m^2·K)	h_c	0.34	W/(m^2·K)

and undergoes stepwise shape recovery towards the maximum bending angle. The current increases from 0 to 20 mA at a 5 mA step and from 20 mA to 40 mA at a 2 mA step. Figure 3.9 shows the average angular recovery percentage versus the current magnitude for three individual tests, computed from the initial bending angle (θ_0), maximum bending angle (θ_m), and stable bending angle (θ_i) at each current level. Since the SMA stress is zero, Equation (3.5) can be simplified into: $\epsilon = \epsilon_0\xi$. Since the length of the bending segment of the SMA wire is constant, we have: $\xi = \frac{\theta_m - \theta_i}{\theta_m - \theta_0}$. At each stable bending angle, it is assumed that the SMA wire and nichrome coils are in the quasi-static status, so a quasi-static model is derived from Equations (3.3) and (3.4) and then combined with the SMA constitutive model to estimate the value of h_c using the least-square approach. The estimated value of h_c is listed in Table 3.1. Figure 3.9(a) shows the model prediction. The RMSE and R^2 value are equal to 0.0704 and 0.9775, respectively. The estimated value of h_c is relatively small, since there is a adhesive layer between the SMA wire and nichrome coils, and the actual contact area is smaller than the assumption made for Equation (3.4). Overall, the model has successfully captured the thermomechanical properties of the SMA bending module and the model can potentially be used for design optimization and model-based control in the future.

3.3.4 Proof-of-Concept Demonstration

To evaluate the working performance of the developed cardiac catheter with an SMA-actuated steerable tip, a catheter prototype is inserted into the right atrium through the inferior vena cava for a proof-of-concept demonstration, as shown in Figure 3.10. When the catheter tip is actuated, its motion can be viewed via a viewing channel through the superior vena cava. The initial posture of the catheter tip is shown in Figure 3.10(b). Afterwards, 50 mA electric current under pulse width modulation (PWM) was applied to individually actuate the first two distal bending modules and the PWM intensity was controlled by an operator via a keyboard. Figures 3.10(c) and (d) show the tip moving upward and downward, respectively, by actuating the first distal bending module. In this procedure, the PWM intensity was increased from 0 to 100% and then decreased to 0 for the nichrome coils responsible for bending the tip upward, followed by the increase of PWM intensity from 0 to 100% for the nichrome coils responsible for bending the tip downward. While keeping the tip downward, the second distal bending module was actuated to bend the tip leftward and rightward in a similar way, as shown in Figures 3.10(e) and (f), respectively.

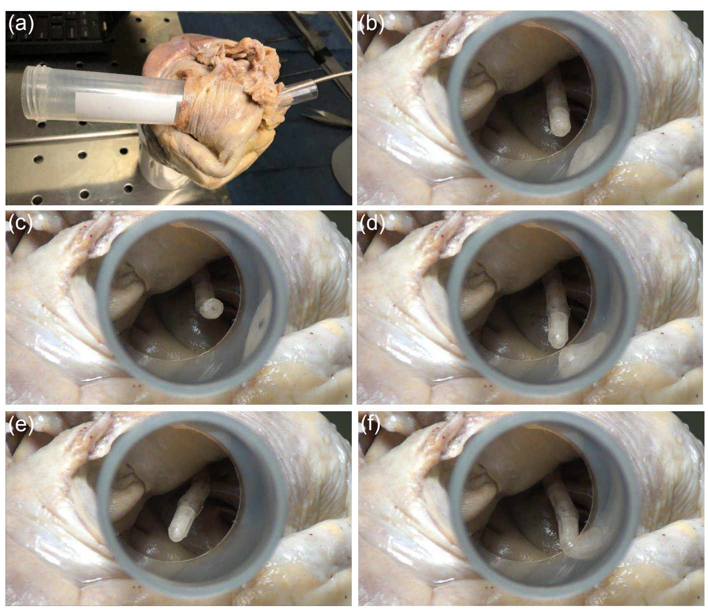

Figure 3.10: Manipulation of the steerable robotic catheter inside the right atrium: (a) catheter inserted through the inferior vena cava and viewed from the superior vena cava, (b) straight steerable tip before actuation, (c) tip moving upward, (d) tip moving downward, (e) tip moving leftward, and (f) tip moving rightward.

3.4 Discussion and Conclusions

In this paper, an SMA bending module requiring low electric current for actuation is developed. By integrating multiple SMA bending modules with a flexible tube, a steerable, MRI-compatible robotic catheter is developed for AFib treatment. Each SMA bending module consists of a pair of antagonistic SMA wires, which memorize curvatures opposite to each other. To reduce the electric current required for SMA actuation and minimize the induced electromagnetic field, a conductive heating actuation technique is developed by routing a folded, enameled nichrome wire around SMA wires using customized jigs. After modeling the SMA bending module, the working performance of the SMA bending module shows the durability of the conductive heating technique. The electric current required for SMA actuation is reduced by about 80% compared with direct Joule heating actuation for the same level of block force output. A proof-of-concept demonstration have shown the potential of using the developed catheter as an alternative tool for the treatment of AFib. Although the maximum bending angle of the SMA bending module decreases when it performs cyclic motion, it will not be an issue if feedback control is implemented and reference angles are smaller than the stable maximum bending angle. In addition, the actuation speed can be improved by adjusting the electric current under feedback control.

CHAPTER 4

FIBEROPTIC ROTATION SENSOR

The compact torsion module presented in Chapter 2 is promising for surgical robotics by using the SMA actuation technique. Due to the nonlinear and hysteretic thermomechanical properties of SMA as well as unknown external loading applied on the SMA torsion module, a motion feedback mechanism is required to estimate the rotation of the SMA torsion module and control it in a closed-loop manner. To develop a robust, compact, and low-cost sensing system, this chapter will present the development of a fiberoptic rotation sensor based on light intensity modulation.

The rest of this chapter is organized as follows. Section 4.2 presents the design and fabrication of the fiberoptic rotation sensor. Section 4.3 models the working principle of the sensor based on light intensity modulation (LIM). Section 4.4 presents several experimental studies to optimize the sensor design, verify the model, calibrate the sensor, and evaluate its working performance. Section 4.5 concludes the chapter.

4.1 Sensor Design and Fabrication

The fiberoptic rotation sensor is designed as a sensing module that can be readily mounted on the SMA torsion module. Three generations of the fiberoptic rotation sensor have been developed. In the first generation, one optical fiber set is utilized, and the measurement range is smaller than 180°. To improve the measurement range and precision, multiple fiber sets are used in the second- and third-generation sensors.

4.1.1 First generation: One Fiber Set

As shown in Figure 4.1, the first-generation fiberoptic rotation sensor consists of an optical fiber set and a rotary head mounted on the sensor shaft inside the sensor housing. The length and diameter of the first-generation rotation sensor are 21 mm and 8 mm, respectively. As shown in Figure 4.1(a) and Figure 4.2(a), the sensor shaft can be connected to the shaft of the SMA torsion module via the

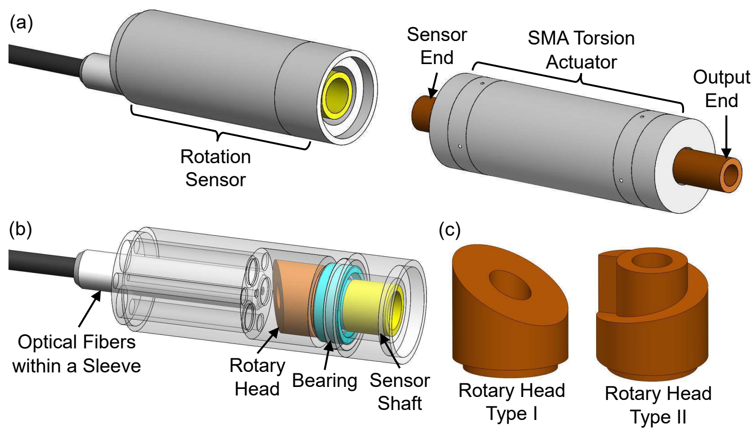

Figure 4.1: Design of the first-generation fiberoptic rotation sensor: (a) fiberoptic rotation sensor to be integrated with the SMA torsion module, (b) fiberoptic rotation sensor consisting of an optical fiber set, a rotary head, and a shaft, and (c) two designs of the rotary head with different reflective surface profiles.

friction between them. A metallic micro bearing is used to enable frictionless rotation of the rotary head, as shown in Figure 4.1(b). Thus, the friction applied on the torsion module by the rotation sensor is negligible. Meanwhile, the tip of the fiber set is encased inside the lumen in the bottom of the sensor housing using UV-cured epoxy. Except for the rotary head, bearing, and optical fiber set, all other components are 3D-printed in plastic material.

The proximal side of the rotary head close to the fiber set is a reflective surface with a varying profile. Thus, the distance traveled by the light beam from the tip of the fiber set to the reflective surface changes versus the rotation angle of the SMA torsion module. The optical fiber set is an off-the-shelf product containing both transmitting and receiving optical fibers (Keyence Corporation, Japan). A signal conditioner (Model FS-V31M, Keyence Corporation, Japan) is used to supply 640 nm wavelength light using a red light-emitting diode (LED) as a light source and convert received light into an analog voltage output in the range of 1 V to 5 V. Two models of the fiber sets are evaluated in this study. The model FU-46 fiber set contains two 125 μm diameter receiving fibers and two 125 μm diameter transmitting fibers in a plus configuration. The model FU-24X fiber set contains one 175 μm diameter transmitting fiber surrounded by eight 175 μm diameter receiving fibers. Since the light reflective rate of the reflective surface is determined by the color and surface texture of the rotary head, brass and aluminum are individually used to fabricate the rotary head to quantitatively compare their working performance.

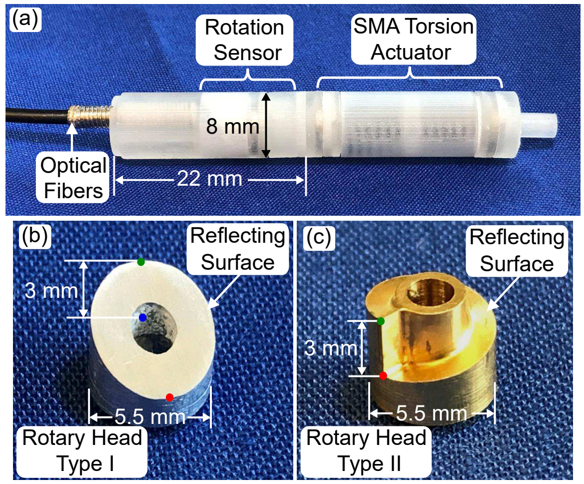

Figure 4.2: Fiberoptic rotation sensor prototype: (a) SMA torsion module integrated with a fiberoptic rotation sensor, (b) type I rotary head made of aluminum, and (c) type II rotary head made of brass.

Two different profiles are designed for the reflective surface of the rotary head, as shown in Figure 4.1(c). The type I rotary head has a tilted, flat reflective surface and the type II rotary head has a 1.25 mm wide one-revolution spiral path around its circumference as the reflecting surface. Figures 4.2(b) and (c) show a type I rotary head made of aluminum and a type II rotary head made of brass, respectively. Both designs have an outer diameter of 5.5 mm. There is a 2 mm diameter hole in the center of the rotary head and a 1.2 mm diameter hole in the bottom of the sensor housing to pass through lead wires and slender tools, such as a suction tubing and electrocauterization wiring. In Figures 4.2(b) and (c), the green dot and red dot represent the highest point and lowest point on the reflective surface, respectively. The blue dot represents the projection of the green dot onto a horizontal plane passing through the red dot. For both rotary heads, the height between the highest point and lowest point is 3 mm. A 5-axis CNC milling machine is used to fabricate the rotary heads and the reflective surface is manually polished using sandpapers with polishing compound. Compared to the type I rotary head, it takes more effort to fabricate and polish the type II rotary head due to its more complex reflective surface.

4.1.2 Second/Third Generation: Multiple Fiber Sets

Figure 4.3(a) shows the exploded view of the NICHE robot equipped with the second-generation fiberoptic rotation sensor. Compared with the first generation, several changes have been made as follows: 1) Three (see Figure 4.3(b)) or more fiber sets are used and installed in the sensor housing; 2) only the model FU-24X fiber set is utilized as the sensing element since it outperforms the model FU-24 fiber set, which will be discussed in Section 4.3.1; 3) the brass type I rotary head is used as the sensor rotor, since it outperforms rotary heads of other designs and materials, which will be discussed in Section 4.3.1. To address the challenge in manually polishing the reflective surface, a new method is proposed to fabricate the type I rotary head for the third-generation sensor. The rotary head is made of a 3D-printed plastic base with a tilted top surface and a brass mirror, which are bonded together using super glue, as shown in Figures 4.4(a) and (b).

The fabrication of the brass mirror includes the following steps: 1) Elliptical discs with an elliptical hole per disc is cut from a 0.8 mm thick polished brass sheet using wire electric discharge machining (EDM); 2) since the polished surface is contaminated during machining, debris are removed by rinsing the discs using acetone and isopropyl alcohol (IPA); 3) the discs are bonded to a glass wafer around the center using wax on a substrate bonder (Logitech, Glasgow, UK), as shown in Figure 4.4(c); 4) the glass wafer with brass discs on it is mounted to a PM5 silicon wafer polisher (Logitech, Glasgow, UK) to polish the brass discs for 2 hours using a Colloidal Silica type polishing suspension (MetLab Corporation, Niagara Falls, NY, USA), as shown in Figure 4.4(d); 5) the brass discs are separated from the glass wafer by melting the wax on the wafer bonder, followed by

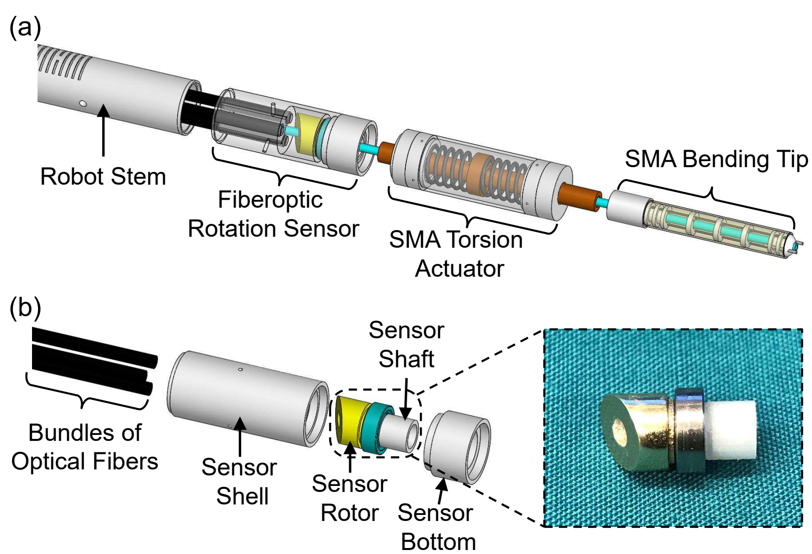

Figure 4.3: Design of the second-generation fiberoptic rotation sensor: (a) exploded view of NICHE robot assembly and (b) exploded view of the fiberoptic rotation sensor with the subset showing the assembly of the rotor, shaft, and bearing.

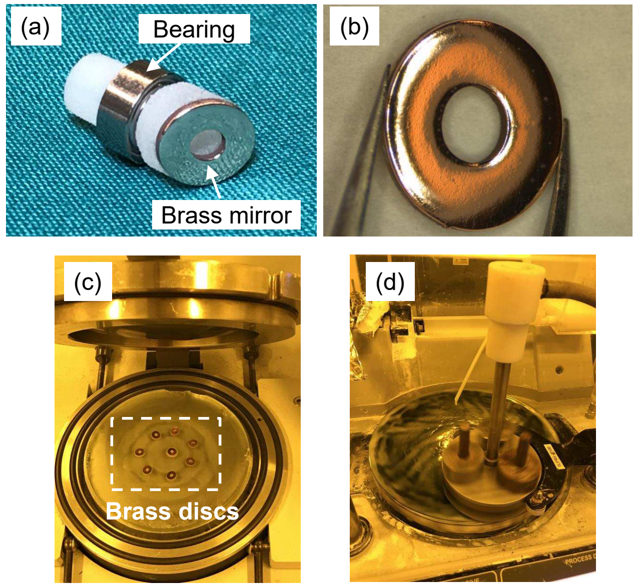

Figure 4.4: Fabrication of the reflective sensor rotor: (a) 3D-printed rotor with a brass micro mirror, (b) microscopic view of the brass micro mirror, (c) bonding brass disks onto a glass wafer before polishing, and (d) polishing brass disks using a wafer polisher.

soaking the wax using nonwoven wipers; 6) the brass discs are rinsed by trichloroethylene (TCE), acetone, and IPA to remove the remaining wax and debris. Compared to previous methods, this method allows batch fabrication and processing to achieve higher surface smoothness, improved efficiency, and more consistent results.

4.2 Light Intensity Modulation Modeling

4.2.1 Coordinate Frame Definition

Figures 4.5(a) to (c) show the schematics of an optical fiber set transmitting a light beam towards the type I and type II rotary heads, respectively. The red line represents the center of the light beam with the maximum intensity and the pink shadow represents beam divergence. The distance traveled by the light beam before reaching the reflective surface is determined by the relative rotation between the rotary head and the fiber set. To model the working principle, the transmitting and receiving fibers are assumed to be coaxial in the fiber set, due to the compact arrangement and small diameter of the optical fibers. As shown in Figures 4.5(a) and (b), a local coordinate frame $\{F_s\}$ is fixed on the rotary head. The $\mathrm{x_s}$-axis points to the lowest position on the reflective surface (red dot) and the

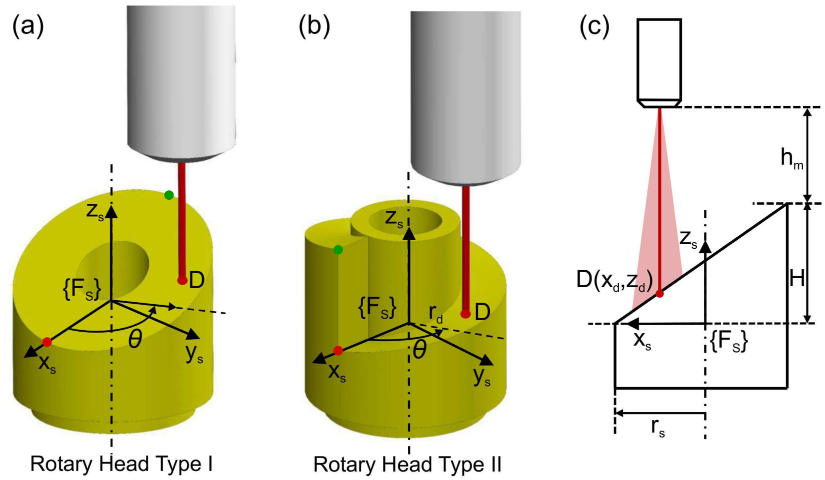

Figure 4.5: Geometrical optics for the reflective rotor: (a) optical fibers transmitting a light beam towards the type I rotary head, (b) optical fibers transmitting a light beam towards the type II rotary head, and (c) light beam towards the reflecting point, D, on the type I rotary head in $\mathrm{x_s}$-$\mathrm{z_s}$ plane.

$\mathrm{z_s}$-axis is aligned with the rotation axis pointing to the optical fibers. For the easiness of modeling, the rotation of the rotary head with respect to the fixed optical fibers is regarded as an equivalent rotation of the optical fibers about the $\mathrm{z_s}$-axis in the opposite direction.

Since the optical fibers are parallel to the rotation axis, the reflecting point, D, on the reflective surface has a constant radius, r_d, with respect to the rotation axis. Thus, the position of D, $[x_d, y_d]$, is given by:

$$\begin{bmatrix} x_d \\ y_d \end{bmatrix} = \begin{bmatrix} r_d C_\theta \\ r_d S_\theta \end{bmatrix} \tag{4.1}$$

where θ is the rotation angle of the optical fibers with respect to the $\mathrm{x_s}$-axis, and C_θ and S_θ denote the *cos* and *sin* functions of θ, respectively. The distance between the lowest position (red dot in Figure 4.5) and highest position (green dot in Figure 4.5) on the reflective surface along the $\mathrm{z_s}$-axis is denoted as H. Both rotary heads have the same radius and it is denoted as r_s. Figure 4.5(c) shows the schematic of the type I rotary head in the $\mathrm{x_s}$-$\mathrm{z_s}$ plane, which is used to derive the position of D along $\mathrm{z_s}$-axis as follows:

$$z_d = \frac{H(r_s - x_d)}{2r_s} \tag{4.2}$$

For the type II rotary head, since the reflective surface is a spiral path, the position of D along the z_s-axis is proportional to θ, which yields:

$$z_d = \frac{\theta H}{2\pi} \tag{4.3}$$

Therefore, the traveled distance of the light beam when it reaches the reflective surface is given by:

$$h = h_m + H - z_d \tag{4.4}$$

where h_m is the distance from the origin of $\{F_s\}$ to the tip of fiber set along the z_s-axis.

4.2.2 LIM for the First Generation

Figure 4.6 shows the principle of the light intensity modulation for the first-generation rotation sensor with one fiber set. The reflecting plane is tangential to the reflective surface through the reflecting point. Due to the reflecting plane, the light beam is transmitted virtually by optical fibers beneath the reflecting plane, as shown in Figure 4.6. The tip centers of the transmitting fibers, receiving fibers, and virtual transmitting fibers are denoted by A, B, and A', respectively. Point C is a projected point to the reflected light beam from A or B. The distance from the virtual transmitting fibers to the receiving fibers along the reflective light beam is given by:

$$\overline{A'C} = h + hC_{2\alpha} \tag{4.5}$$

where α is the tilt angle of the reflecting plane and $\alpha = atan2(H, 2r_s)$. The distance from the receiving fibers to C is given by:

$$\overline{BC} = hS_{2\alpha} \tag{4.6}$$

As shown in Figure 4.6, the intensity distribution of the light beam at the tip of the virtual transmitting fibers, I_t, is in the form of a Gaussian distribution around A', which yields:

$$I_t = I'_{t0} e^{-\frac{r^2}{(w_t/2)^2}} \tag{4.7}$$

where r is the distance to A', I'_{t0} is the maximum light intensity at A', and w_t is the Gaussian width

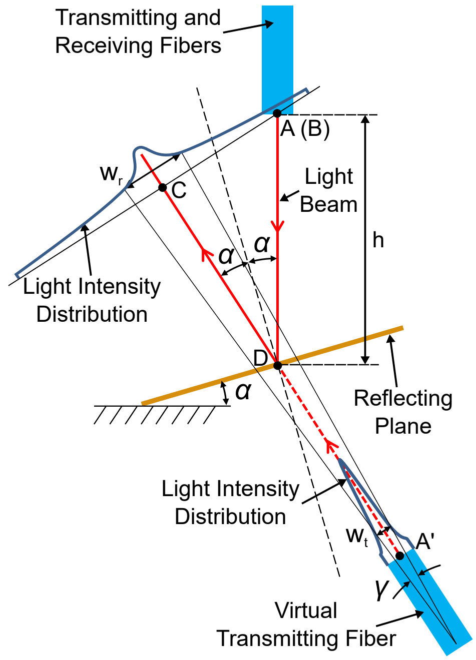

Figure 4.6: Modulation of the light intensity received by the optical fibers for the first-generation sensor.

at $1/e$ of the maximum intensity. It is hypothesized the intensity distribution of the transmitted light beam remains in the form of a Gaussian distribution, while its width changes nonlinearily verus the distance to the tip center of the transmitting fibers [102]. Therefore, the light intensity distribution of the reflected light beam around C is given by:

$$I_r = I_{r0} e^{-\frac{r^2}{(w_r/2)^2}} \tag{4.8}$$

where I_{r0} is the maximum light intensity at C and w_r is the Gaussian width at $1/e$ of the maximum intensity. Note that I'_{t0} is smaller than the maximum light intensity at A for the transmitting fiber, since the light reflective rate for the reflective surface is smaller than one. By approximating the nonlinear relationship between w_r and $\overline{A'C}$ by a conical beam profile [103], we have:

$$w_r = w_t + 2\overline{A'C}\tan\gamma, \tag{4.9}$$

where γ is a divergence angle determined by the fiber set and light source. The total light flux for a particular point along the path of the transmitted light beam, Φ, is given by [103]:

$$\Phi \approx \int_0^\infty I(r) 2\pi r dr = \pi w^2 I_0/4 \tag{4.10}$$

where I_0 is the maximum light intensity at this point and w is the half width at $1/e$ of the maximum intensity. Since the total light flux remains as a constant along the path of the transmitted light beam, the total light flux around A', Φ_t, is equal to the total light flux around C, Φ_r, which yields:

$$\Phi_t = \Phi_r \Rightarrow I_{r0} = w_t^2 I'_{t0}/w_r^2 \tag{4.11}$$

It is assumed that the light intensity at the tip of the fiber set is uniform due to the small diameter of the receiving fibers. Since the voltage output of the signal conditioner is proportional to the light flux received by its photo sensors connected to the receiving fibers, the voltage output, U_s, is given by:

$$U_s = k_v \sigma_r A_r I_r C_{2\alpha}^2 \tag{4.12}$$

where k_v represents the conversion rate from light flux to voltage output by photo sensors, σ_r represents the attenuation of light flux in optical fibers, A_r is the cross-section area of the receiving fibers.

4.2.3 LIM for the Second/Third Generation

The model for the first-generation sensor with one fiber set is extended for the second/third-generation sensor by considering the contributions made by multiple optical fiber sets. As shown in Figure 4.7(a), a local coordinate frame $\{F_s\}$ is fixed on the sensor rotor with the $\mathrm{x_s}$-axis pointing to the lowest point on the reflective surface and the $\mathrm{z_s}$-axis aligned with the rotation axis. Figures 4.7(a) and (b) show that three and four optical fiber sets are equally spaced around the rotor and emit light beams towards the reflective surface, respectively.

Generally, when M optical fiber sets are employed, the rotation angle of each fiber set with respect to the $\mathrm{x_s}$-axis is given by: $\theta_i = \theta + \frac{i-1}{M} 2\pi$, where $i \in \{1, 2, ..., M\}$. The measurement precision will probably increase when more optical fiber sets are employed. In the current system, three fiber sets are used to keep the device compact. In the actual system, the clockwise rotation of the sensor rotor in the top view of Figure 4.7(a) is defined to be positive. As shown in Figures 4.7(a), (b), and (c), A_i, B_i, A'_i, and D_i denote the the tips of the transmitting fibers, receiving fibers, virtual transmitting fibers, and the reflecting point on the reflective surface for the i^{th} optical fiber set,

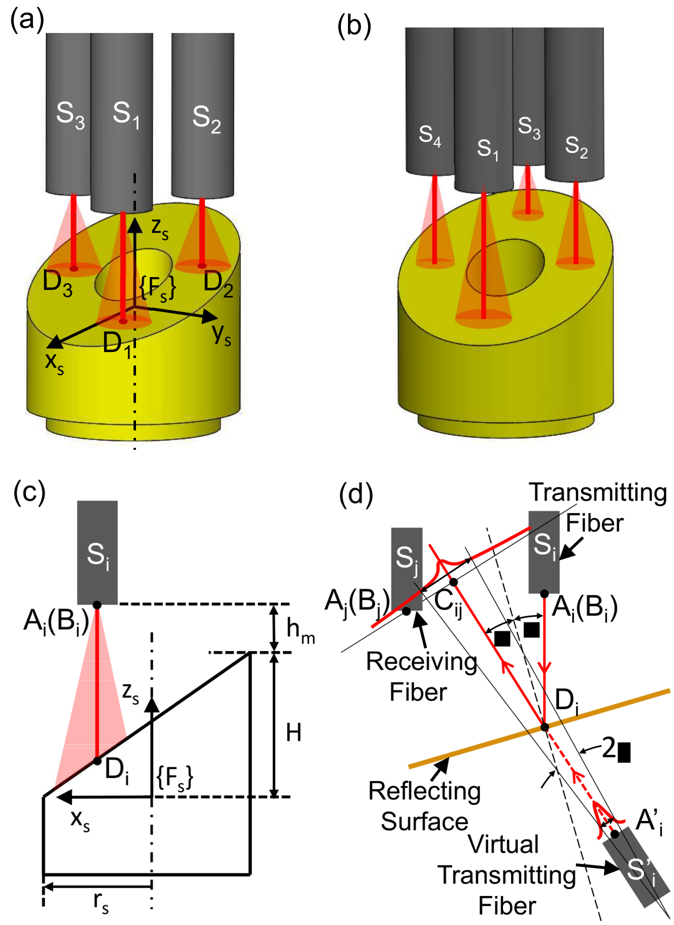

Figure 4.7: Working principle of the second-generation sensor: (a) three optical fiber sets pointing to the reflective sensor rotor, (b) four optical fiber sets pointing to the reflective sensor rotor, (c) one optical fiber set transmitting light to the sensor rotor in the x_s-z_s plane, and (d) light beam transmitted and received by two different optical fiber sets in the second-generation sensor.

respectively. Based on the geometry of the sensor rotor, as shown in Figure 4.7(b), the position of A_i, B_i, and D_i is given by:

$$\boldsymbol{A_i} = \boldsymbol{B_i} = \begin{bmatrix} r_d C_{\theta_i} & r_d S_{\theta_i} & h_m + H \end{bmatrix} \tag{4.13}$$

$$\boldsymbol{D_i} = \begin{bmatrix} r_d C_{\theta_i} & r_d S_{\theta_i} & \frac{r_s - r_d C_{\theta_i}}{2r_s} H \end{bmatrix} \tag{4.14}$$

where r_d is the distance from the center of the fiber set to the rotation axis, r_s is the radius of the sensor rotor, h_m is the distance from the optical fibers to the highest point on the reflective surface along the z_s-axis, and H is the distance between the lowest point and the highest point on the reflective surface along the z_s-axis. Therefore, the travel distance of the light beam before reflection can be denoted by $\overline{A_iD_i}$ and $\overline{A_iD_i} = \overline{A_i'D_i}$ due to the property of light reflection, as shown in Figure 4.7(c).

Intuitively, the light intensity received by the receiving fibers is modulated by $\overline{A_iD_i}$ as a function of the rotation angle, θ_i. Due to the light beam divergence, the light beam emitted by a transmitting fiber has effect on all the optical fiber sets. Hereby, I_{ij} denotes the light intensity that is generated and received by the i^{th} and j^{th} optical fiber set, respectively. Figure 4.7(c) shows the principle of LIM for the second-generation sensor. Point C_{ij} denotes the closet point to B_j along the i^{th} reflected light beam. As we have discussed in the previous subsections, the changes of $\overline{C_{ij}B_j}$ and $\overline{C_{ij}A_i'}$ due to the rotation of the sensor rotor affect I_{ij}. To compute I_{ij}, the vector form of the i^{th} reflected light beam is given by:

$$\boldsymbol{r}_i = \boldsymbol{D}_i + t\boldsymbol{v}_i \tag{4.15}$$

where $t \in \boldsymbol{R}$ and $\boldsymbol{v}_i$ denotes the vector normal to the reflective surface. Considering the definition of $\{F_s\}$, $\boldsymbol{v}_i$ is given by:

$$\boldsymbol{v}_i = \begin{bmatrix} S_{2\alpha} & 0 & C_{2\alpha} \end{bmatrix} \tag{4.16}$$

where α is the tilt angle of the reflective surface with respect to the bottom surface of the rotor and it is given by: $\alpha = atan2(H, 2r_s)$. Thus, the position of C_{ij} is given by:

$$\boldsymbol{C}_{ij} = \boldsymbol{D}_i + \frac{(\boldsymbol{B}_j - \boldsymbol{D}_i) \cdot \boldsymbol{v}_i}{\|\boldsymbol{v}_i\|^2}\boldsymbol{v}_i \tag{4.17}$$

Based on the position of C_{ij}, $\overline{C_{ij}B_j}$ and $\overline{C_{ij}A_i'}$ can be calculated. By following the same process from Equation (4.7) to Equation (4.11), the light distribution around A_i' and C_{ij} can be modeled. It is assumed that the total light flux received by a fiber set is the linear summation of the light flux from all the fiber sets. Therefore, the voltage output of the i^{th} signal conditioner is given by:

$$U_i = \sum_{j=1}^{M} k_v \sigma_r A_r I_{ji}(\overline{C_{ji}B_i}) C_{2\alpha}^2 \tag{4.18}$$

where the definitions of k_v, σ_r, and A_r are the same as the definitions for Equation (4.12). Thus, the sensor output is a vector comprised of the voltage outputs of all the fiber sets, which yields:

$$\boldsymbol{V}(\theta) = \begin{bmatrix} U_1 & U_2 & \cdots & U_M \end{bmatrix} \tag{4.19}$$

The sensitivity is thereby defined as: $S_\theta = \| \frac{d\boldsymbol{V}(\theta)}{d\theta} \|$. Figure 4.8(a) shows the simulation results of the normalized sensitivity versus rotation angle based on this definition and the developed model. Figure 4.8(b) shows the change of the normalized sensitivity versus the number of fiber sets. In this study, it is determined to use three fiber sets for the second-generation sensor since it can achieve sufficiently high average sensitivity while maintaining the compact footprint of the device.

4.3 Preliminary Studies and Calibration

4.3.1 Performance Comparison

To optimize the sensor design, several experimental studies are performed using the first-generation sensor with one fiber set. Figure 4.9 shows the experimental setup comprised of a fiberoptic rotation sensor and a DC motor equipped with a 1024:1 gearhead (Faulhaber, Switzerland). The motor is capable of rotating the sensor shaft via a connective shaft between them. Meanwhile, a high-resolution optical rotary encoder (CUI Inc., USA) is mounted on the connective shaft to directly measure the rotation angle. The rotation sensor is rotated back and forth stepwise by one revolution with a 1° step size per second. The home position is manually set at a rotation angle where the voltage output by the fiberoptic rotation sensor is close to the minimum. A moving average filter is

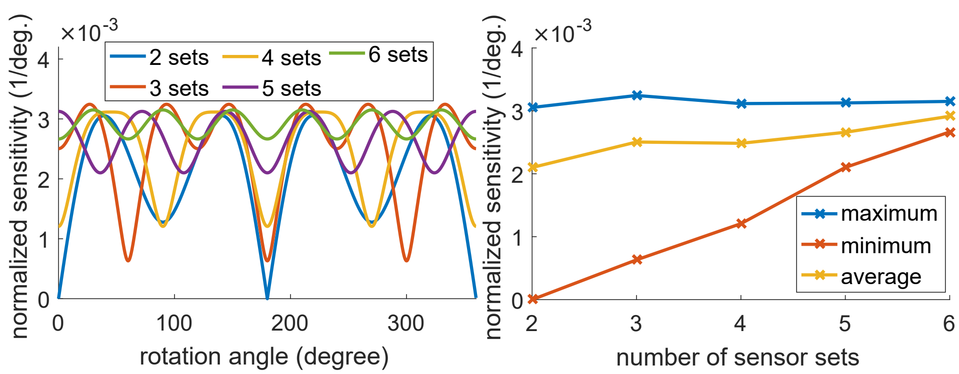

Figure 4.8: Simulation results of sensitivity: (a) normalized sensitivity versus rotation angle for different fiber sets and (b) normalized sensitivity versus number of fiber sets.

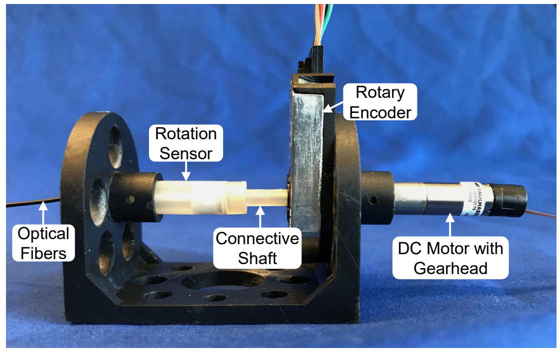

Figure 4.9: Experimental setup for comparing the working performance of different designs and verifying the developed model for the first-generation sensor.

employed to smooth the voltage output of the signal conditioner.

In the first study, the performances between a brass type I rotary head and a aluminum type II rotary head are compared using the model FU-24X optical fibers. Figure 4.10(a) shows that a large measurement range can be achieved by both devices, while the voltage output of the sensor with the brass rotary head is slightly larger, probably due to the different light reflective rates for reflective surfaces with different colors and surface textures. The difference in the output voltage is also probably caused by the discrepancy in polishing the reflective surface.

In the second study, the performances between two models of optical fibers are compared using the brass type I rotary head. Figure 4.10(b) shows that the model FU-24X fiber set has a larger measurement range than the model FU-46 fiber set. This is probably because the model FU-24X fiber set contains more receiving optical fibers, resulting in higher sensitivity than the model FU-46 fiber set when h is large. Although the rate of the change of h is small when h is small for the type I rotary head, the sensitivity of the optical fibers increases rapidly when the target becomes closer. Hence, the voltage output oscillates around the peak when h is close to the minimum, as shown in Figure 4.10(b). The choppy output is more obvious for the model FU-46 fiber set, probably because its sensitivity becomes too high when h is small.

In the third study, the performance between a type I rotary head and a type II rotary head, both of which are made of brass, are compared using the model FU-24X optical fiber. Figure 4.10(c) shows that the voltage output for the type II rotary head has a rapid drop when the rotation angle passes 200° due to the step change in the spiral reflective path. The voltage output for the type II

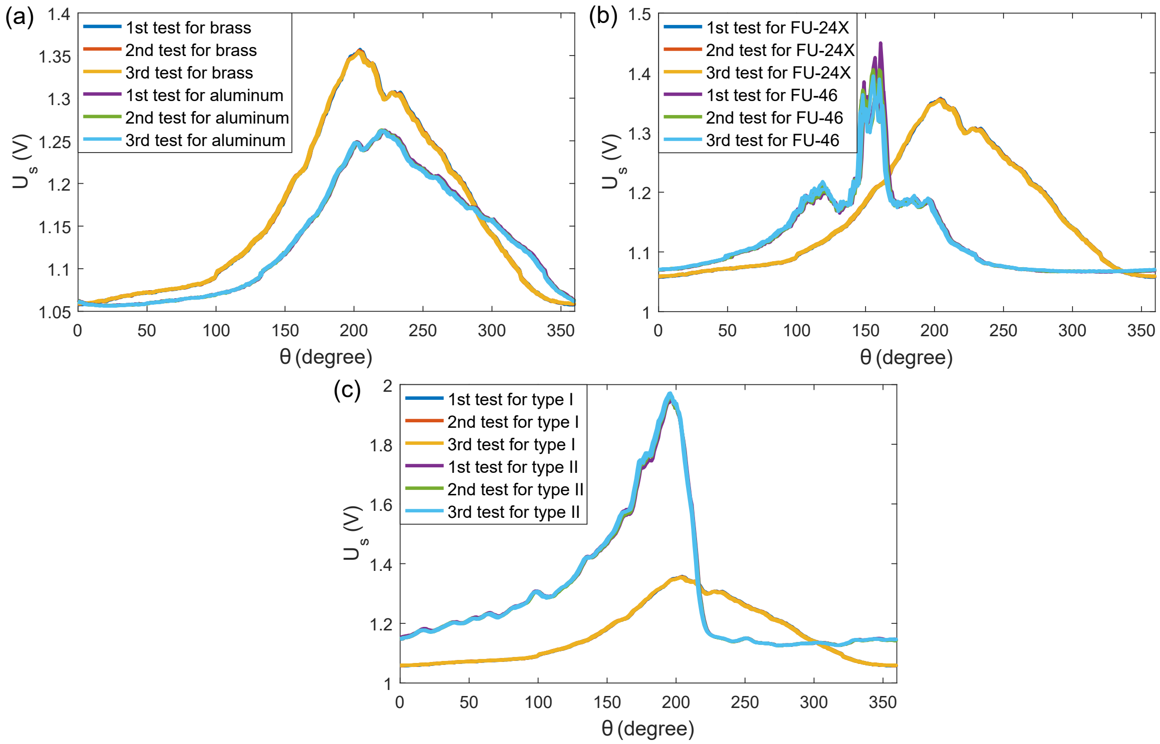

Figure 4.10: Experimental results for different designs of the first-generation sensor: (a) comparing two type I rotary heads made of brass and aluminum, (b) comparing two different off-the-shelf optical fiber sets, (c) comparing a brass type I rotary head and a brass type II rotary head.

rotary head is less smooth, probably due to the difficulty in polishing its spiral path. The voltage output for the type II rotary head is also larger, probably due to the light reflection at the sidewall other surfaces in addition to the spiral path. Figure 4.10(c) shows good uniformity among different tests and negligible hysteresis between positive motion and negative motion.

Thus, the combination of a brass type I rotary head and a model FU-24X optical fiber set is the optimal choice for a fiberoptic rotation sensor. Note that three individual tests were conducted in each of the above studies. A supplementary study is carried out by measuring the voltage output in 60 s when the rotation angle is fixed. It is observed that the output signal has an average fluctuation of 1.9 mV, 1.7 mV, and 2.2 mV with negligible drift over time when the rotation angle is fixed at 0°, 90°, and 180°, respectively. In each test, a black vinyl tape was wrapped outside the rotation sensor after 30 s to mimic the illumination change when the rotation sensor is used in *in vivo* clinical studies. It is observed that the output voltage is steady under the change of environmental illumination.

4.3.2 Model Verification

To verify the derived model for the fiberoptic rotation sensor, the least-squares approach is used to fit the derived model with experimental data presented in the previous subsection. According to the model equations in Section 4.2, several parameters need to be determined. The geometric parameters, including h_m, H, r_d and r_s, are determined in the design process. The fiberoptic parameter, γ, is obtained from the specification sheet of the off-the-shelf optical fiber sets. The value of w_t has a negligible effect on the voltage output since it is much smaller than the second item in Equation (4.9). By normalizing Equation (4.12) and the experimental data, the characterization of the other parameters including k_v, σ_r, A_r, and I'_{t0} is not required for model verification.

During the implementation of the least-squares approach, the home position is searched to achieve the best fitting result. By individually fitting the normalized model with the normalized experimental data for the type I rotary head and type II rotary head, the results are shown in Figures 4.11(a) and (b), respectively. The RMSEs for the brass type I rotary head and the brass type II rotary head are equal to 0.04 and 0.17, respectively, and the R^2 values for them are equal to 0.98 and 0.54, respectively. Therefore, the derived model has successfully modeled the response of a first-generation fiberoptic rotation sensor composed of the type I rotary head. Although there is a relatively large discrepancy between the model prediction and experimental data for the type II rotary head, the model has captured the major response of the sensor. The discrepancy is primarily caused by the following factors: a) roughness of the reflective surface, b) unmodeled light reflection

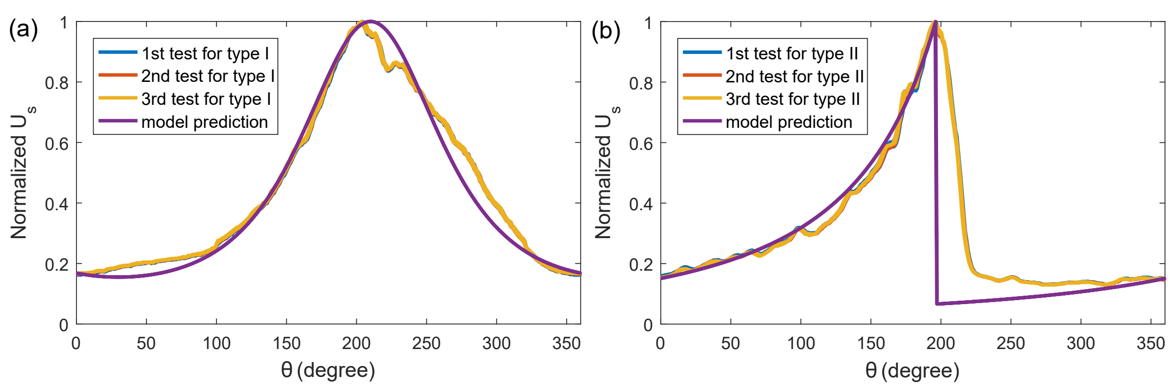

Figure 4.11: Normalized experimental results when the shaft of the first-generation sensor is rotated by 360°: (a) RMSE is 0.04 and R^2 value is 0.98 for the brass type I rotary head and (b) RMSE is 0.17 and R^2 value is 0.54 for the brass type II rotary head.

by the sidewall of the rotary head, and c) unmodeled transition of the diverged light beam from the highest position to the lowest position on the spiral path. The better model prediction for the type I rotary head is another reason why it is used for the fiberoptic rotation sensor.

4.3.3 Calibration of the First Generation

Based on the above studies, a first-generation fiberoptic rotation sensor equipped with a brass type I rotary head and a model FU-24X optical fiber set is developed. The experimental data for the type I rotary head in Figure 4.10(c) is used to calibrate the mapping from voltage output to rotation angle. The experimental data for the negative motion is linearly interpolated at the rotation angle for the positive motion. As a result, the dashed line in Figure 4.12(a) shows the average of interpolated results for the negative motion and the original results for the positive motion. Regions 1 and 3 and region 2 in Figure 4.12(a), corresponding to the basin and peak in Figure 4.10(c), respectively, do not have a strict one-to-one mapping from voltage output to rotation angle, so linear fitting is applied individually. For the remaining regions, a look-up table is made based on the experimental data and the rotation angle and the voltage output between two sampled data points is computed by linear interpolation.

To evaluate the working performance of the developed fiberoptic rotation sensor, the sensor is actuated by a DC motor to follow sinusoidal references with different amplitude, A_s, and periodic

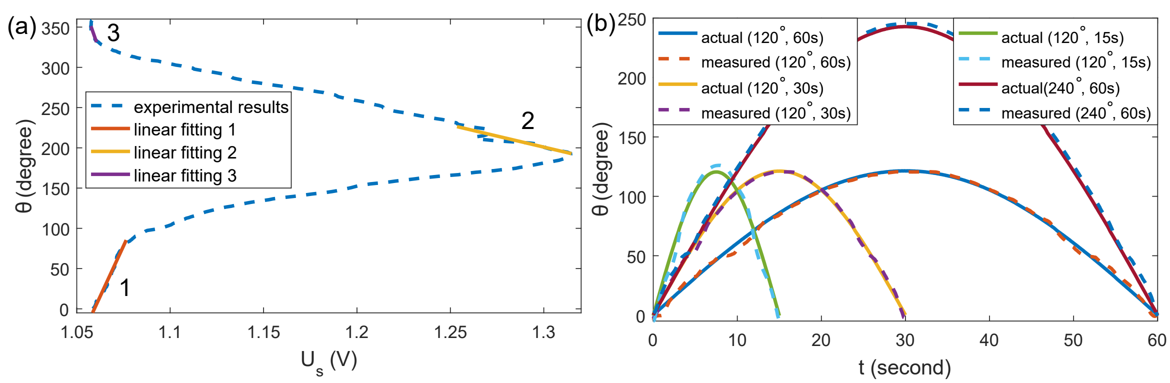

Figure 4.12: Calibration of the first-generation sensor: (a) rotation angle versus sensor output (R^2 values for the linear fitting 1, 2, and 3 are 0.98, 0.88, and 0.55, respectively) and (b) comparing the measurements of the rotary encoder and the developed fiberoptic rotation sensor (RMSEs are 2.27°, 2.06°, 4.36°, and 5.99° for the tests when (A_s, T_s) is equal to (120°, 120 s), (120°, 60 s), (120°, 30 s), and (240°, 120 s), respectively).

time, T_s, using the setup shown in Figure 4.9. The comparison between the measurements of the fiberoptic rotation sensor and the rotary encoder is shown in Figure 4.12(b). It is observed that the measurement is less precise when the rotation speed is increased (T_s is equal to 30 s), probably due to the slight decentration of the rotary head at high speed. When A_s is increased to 180°, two rotation angles probably exist for a particular voltage output. Thus, the timing of using the linear fitting results in region 2 is assumed to be pre-known based on the commands to the DC motor. The measurement error is further increased when A_s is equal to 240°, due to the error in the linear fitting for region 2.

4.3.4 Calibration of the Second/Third Generation

Figure 4.13 shows the experimental setup for the calibration of the second-generation fiberoptic rotation sensor. A DC motor with a 128:1 gearhead (Maxon Motor, Sachseln, Switzerland) is connected to the sensor shaft via a connecting link. Thereafter, the rotary head of the sensor is rotated by the DC motor to follow a pre-designed trajectory. In the calibration tests, the stepwise trajectory increases to 360° and then decreases to 0° at the speed of 0.1° per step per second for eight cycles. During each step, the voltage output of each optical fiber set in the last 200 ms is averaged as the voltage output for a particular rotation angle. Figure 4.14(a) shows the voltage output of three optical fiber sets, denoted as sensor A, B, and C, for the eight cycles. It is observed that the amplification gains are different for these three fiber sets. The system shows good repeatability, as the root-mean-square deviation with respect to the average is 2.0 mV, 1.1 mV, and 1.7 mV for the positive rotation

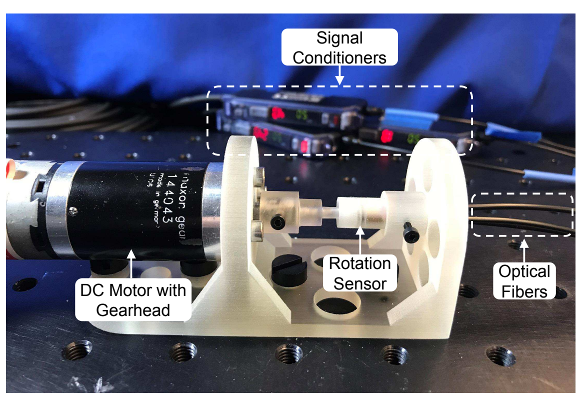

Figure 4.13: Experimental setup for calibrating the second-generation fiberoptic rotation sensor.

and 1.7 mV, 1.0 mV, and 1.5 mV for the negative rotation for sensor A, B, and C, respectively. The systems also shows negligible hysteresis, since the difference of the average voltage is only 0.7 mV, 1.6 mV, and 2.1 mV between positive and negative rotation for sensor A, B, and C, respectively. Figure 4.14(b) shows that the voltage output for the motion range from 0° to 360° forms two closed loops for the positive and negative rotation, respectively, and the two loops overlap with each other. Therefore, all the results for the eight positive cycles and eight negative cycles are averaged for the calibration purpose. Due to the different amplification gains, the voltage change compared to the minimum voltage output is computed and then normalized by the range of the voltage change, so

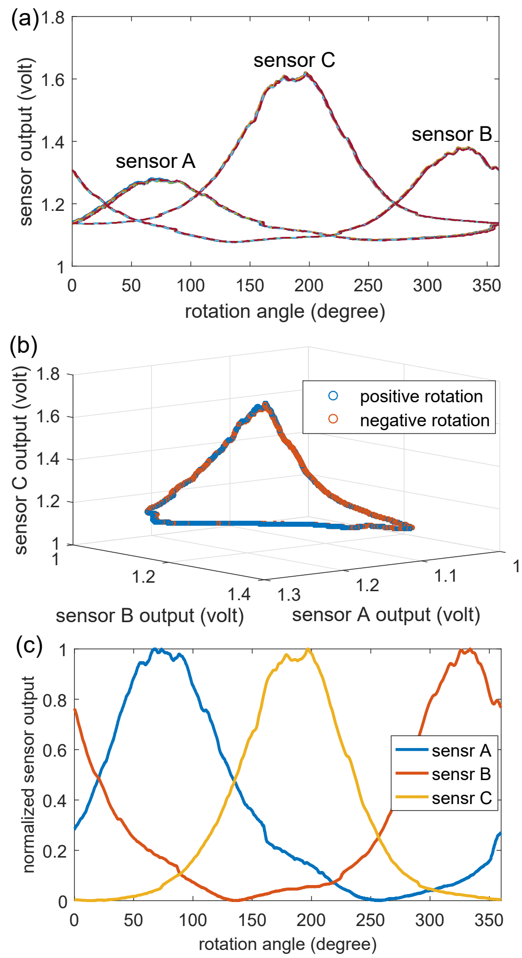

Figure 4.14: Calibration of the second-generation sensor: (a) voltage output of three fiber sets (A, B, and C) versus rotation angle when the sensor shaft rotates from 0° to 360° and then to 0° for eight cycles, (b) 3D space formed by the voltage output of the three fiber sets with showing negligible hysteresis, and (c) normalized average voltage output of the three fiber sets.

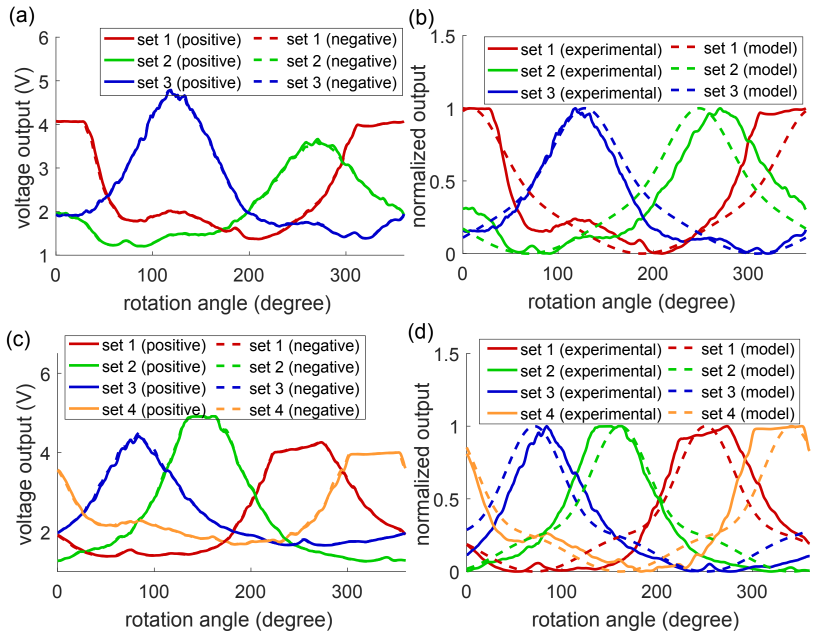

Figure 4.15: Calibration of the third-generation sensor: (a) voltage output of the three-set sensor, (b) normalized output of the three-set sensor, (c) voltage output of the four-set sensor, and (d) normalized output of the four-set sensor.

that the significance of the three optical fiber sets is equal when the normalized results are used for calibration. Figure 4.14(c) shows the normalized voltage change with respect to the rotation angles. The spacing between two neighboring peaks is about 120°, which satisfies the developed model.

The same experimental setup and protocol are used to calibrate the third-generation sensor, except that the step size is 1° per second. The performance of two sensors consisting three fiber sets and four fiber sets, respectively, is compared. Figures 4.15(a) and (c) shows the average voltage outputs for the three-set sensor and four-set sensor, respectively. The average hysteresis between positive and negative rotation is 5.1 mV and 7.7 mV for the three-set sensor and four-set sensor, respectively. The voltage outputs are normalized and compared with the model predictions, as shown in Figures 4.15(b) and (d). The RMSE is 0.1453 and 0.1149 for the three-set sensor and four-set sensor, respectively. The R^2-value is 0.9044 and 0.9433 for the three-set sensor and four-set sensor, respectively. Compared to the second generation (see Figure 4.14), the maximum voltage output by the fiber set in the third-generation sensor is increased by about 6 times, due to the improved reflective rate of the machine polished brass mirror.

4.4 Experimental Evaluation and Demonstration

4.4.1 Measurement Algorithm

The voltage output of the developed sensor obtained in the calibration tests forms a calibration space, denoted by $\boldsymbol{V}_c = \begin{bmatrix}\boldsymbol{V}_1 & \boldsymbol{V}_2 & \dots & \boldsymbol{V}_N\end{bmatrix}^\intercal$, corresponding to a series of rotation angles, denoted by $\boldsymbol{\theta}_c = \begin{bmatrix}\theta_1 & \theta_2 & \dots & \theta_N\end{bmatrix}^\intercal$. N represents the volume of the calibration space and it is determined by the step size during calibration. Due to the high tracking precision of the DC motor, $\boldsymbol{\theta}_c$ is equal to the angle references during the calibration tests. When multiple sets of optical fibers are used, $\boldsymbol{V}_k = \begin{bmatrix}U_{k1}^n & U_{k2} & \dots & U_{kM}\end{bmatrix}^\intercal$, where $k \in \{1, 2, \dots, N\}$.

To determine the rotation angle for a given set of voltage output by all the fiber sets, denoted as $\boldsymbol{V}_t = \begin{bmatrix}U_1 & U_2 & \dots & U_M\end{bmatrix}^\intercal$. $\boldsymbol{V}_t$ is recursively compared with all the elements in $\boldsymbol{V}_c$ to search the optimal estimation of the rotation angle, $\hat{\theta}_l$, which produces the minimum cost for the l^{th} element in $\boldsymbol{V}_c$. The cost between $\boldsymbol{V}_k$ and $\boldsymbol{V}_t$ is defined as the Euclidean distance between them and it is given by: $C_k = \|\boldsymbol{V}_k - \boldsymbol{V}_t\|$. An optimal rotation angle can be determined as the weighted average of a pool of rotation angles with the minimum costs and each weight is the reciprocal of the individual cost. The computation load increases proportionally as the pool size increases, but the improvement of the measurement precision is insignificant if the step size during calibration is small. To reduce the computation load, only the space near the previous optimal rotation angle needs to be explored, due to the finite rotation speed of the SMA torsion module under finite heating current. It is observed that when the search range is $\pm5°$, $\pm10°$, and $\pm20°$, the computation takes about 0.66, 1.35, 2.90 ms on average, respectively, using a desktop computer (Intel® Core™ i7-7700 CPU @ 3.60 GHz).

When the fiberoptic rotation sensor is used for the motion feedback of the SMA torsion module, the rotation angle is measured using the above method at each time step. However, since the calibrated rotation range is from 0° to 360°, the boundary change between 0° and 360° needs to be taken care of. When the torsion module rotates and passes the boundary, there will be an abrupt change in the angle measurement. When the angular position stays around the boundary, the measurement may jump between the two sides of the boundary due to measurement noise. To solve this issue, when the change of the angle measurement is larger than a threshold, the angle measurement is updated by keeping adding 360° to or subtracting 360° from the measurement until the change is smaller than the threshold.

4.4.2 Precision Evaluation

To evaluate the working performance of the developed rotation sensor, the rotary motion in each calibration cycle is measured based on the averaged, normalized calibration results and compared with the actual rotation angles. The histograms of measurement errors for the positive rotation and negative rotation are shown in Figures 4.16(a) and (b), respectively. In each case, the histogram of measurement errors has a Gaussian-like distribution. The RMSE and maximum error are equal to 1.13° and 8.10° for the positive rotation, respectively. The RMSE and maximum error are equal to 1.10° and 8.60° for the negative rotation, respectively. In Figure 4.16(c), the average measurement errors are plotted together with the calibrated sensitivity versus the rotation angle. It is observed

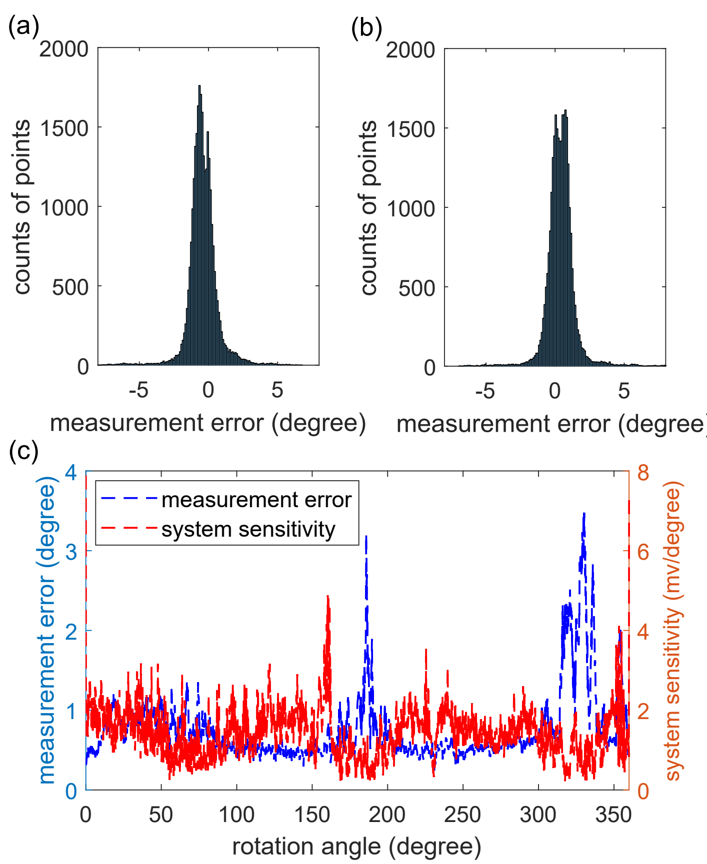

Figure 4.16: Measurement error analysis for the second-generation sensor: (a,b) error histograms of the measurements based on the average, normalized calibration results for (a) positive rotation and (b) negative rotation, and (c) average measurement error and system sensitivity versus rotation angle.

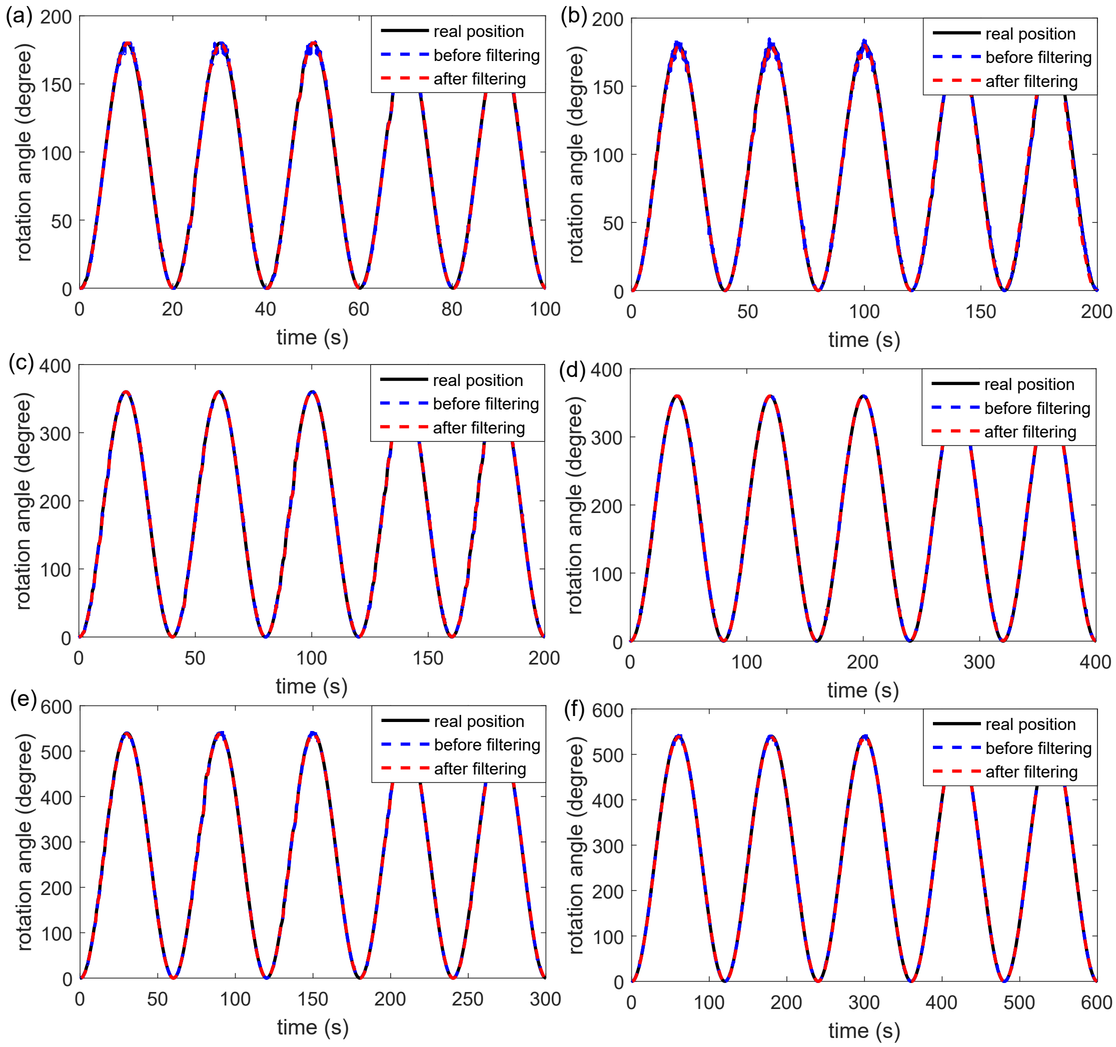

Figure 4.17: Evaluation tests for the second-generation sensor: (a) $A_\theta = 180°$ and $T_\theta = 20\ s$, (b) $A_\theta = 180°$ and $T_\theta = 40\ s$, (c) $A_\theta = 360°$ and $T_\theta = 40\ s$, (d) $A_\theta = 360°$ and $T_\theta = 80\ s$, (e) $A_\theta = 540°$ and $T_\theta = 60\ s$, and (f) $A_\theta = 540°$ and $T_\theta = 120\ s$. The rotation angles are relative to the initial position.

that the higher the sensitivity, the higher the measurement precision. Thus, the sensitivity and measurement error has an inverse correlation, as shown by the crests and troughs in Figure 4.16(c).

The calibration setup shown in Figure 4.13 is used to evaluate the measurement precision of the second-generation fiberoptic rotation sensor. The DC motor is actuated to follow sinusoidal references with different amplitudes, A_θ and periodic time, T_θ. The angles measured by the fiberoptic rotation sensor are compared with the readings provided by the motor encoder. Due to the finite speed of the SMA torsion module under finite heating current, a moving average filter is applied to the measurements. Figure 4.17 shows the angle measurements before and after applying the low

Table 4.1: Experimental results of sensor evaluation

	Motion amplitude	Periodic time	RMSE	Maximum error
Unit	degree	second	degree	degree
1	180	20	1.30	3.48
2	180	40	1.29	6.06
3	360	40	1.38	5.42
4	360	80	1.04	4.14
5	540	60	1.77	6.19
6	540	120	1.59	7.29

pass filter. The profiles show the relative angular position with respect to the home position. It is observed that the measurement error is relatively large in the range corresponding to the crests of the measurement errors in Figure 4.16(c). Table 4.1 summarizes the working performance and it is observed that the measurement error increases when the rotation speed increases, probably due to the reduced reliability of the frictional coupling between the shaft of the sensor and the shaft of the torsion module for faster rotation.

The calibration results are used to evaluate the measurement precision during the calibration

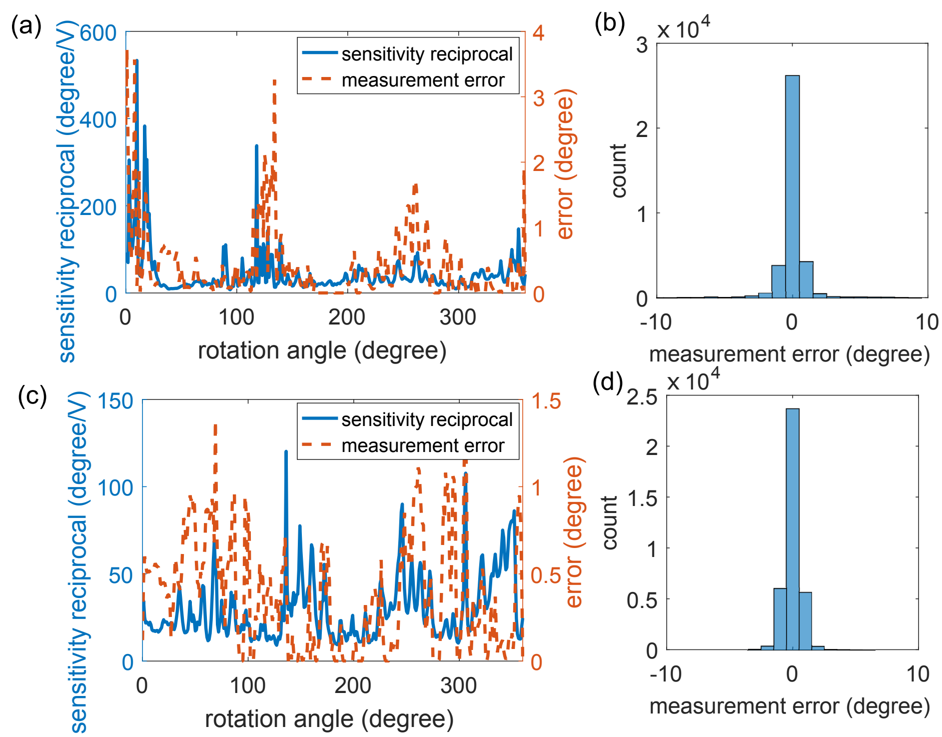

Figure 4.18: Measurement error analysis for the third-generation sensor: (a,c) average measurement error and sensitivity versus rotation angle for three-set sensor (a) and four-set sensor (c), and (b,d) error histograms for three-set sensor (b) and four-set sensor (d).

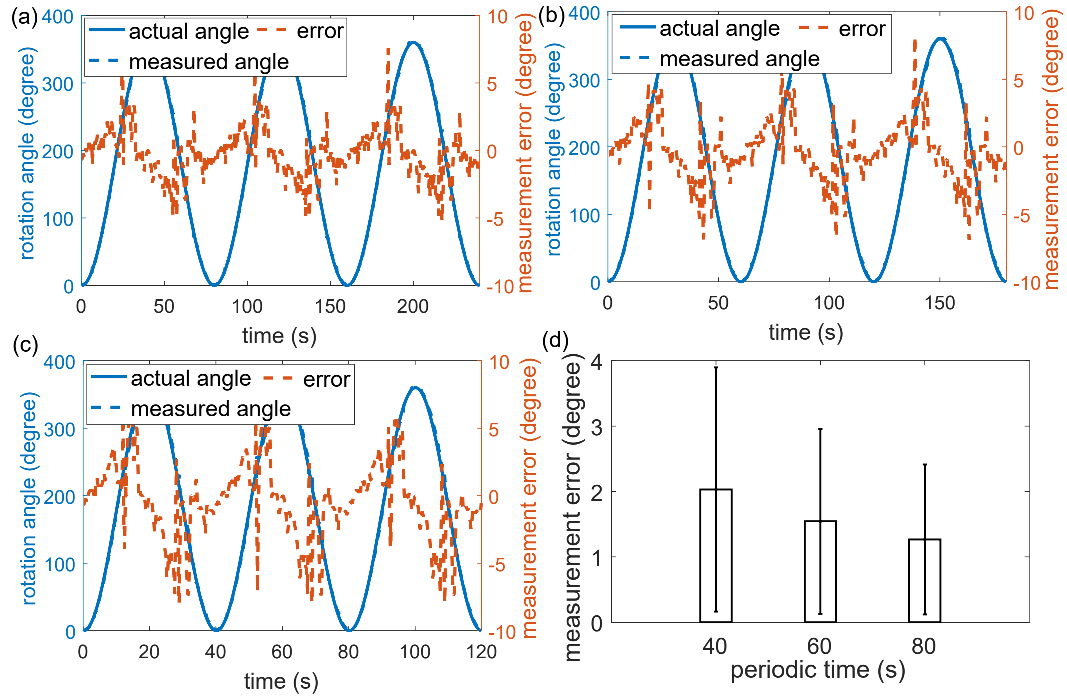

Figure 4.19: Evaluation tests for the second-generation sensor: (a) $T_\theta = 80\ s$, (b) $T_\theta = 60\ s$, (c) $T_\theta = 40\ s$, and (d) measurement error comparison.

studies. Figures 4.18(a) and (c) show the average measurement error over the cycles and sensitivity versus the rotation angle. Same as the second generation, it is observed that the measurement error is higher at rotation angles where the sensitivity is lower. The histograms of measurement errors for the three-set sensor and four-set sensor are shown in Figures 4.18(b) and (d), respectively. Table 4.2 shows that the average measurement error is similar when using four fiber sets; however, the maximum error is reduced significantly by about 59%, since the minimum sensitivity is increased by about 3.6 times. Their working performance is also compared with the second-generation sensor. It is observed that although the maximum error is similar, the average error is reduced by 66.7% by using the machine polished reflector in the third-generation. The measurement precision of the third-generation sensor is evaluated for sinusoidal trajectories based on the calibration results, as shown in Figure 4.19. The sensor shaft is rotated by the DC motor by following sinusoidal trajectories with an amplitude of 360° and different periodic time, T_θ. The average error is 1.27°, 1.54°, and 2.03° with a standard deviation of 1.15°, 1.41°, and 1.87° for the period time of 80 s, 60 s, and 40 s, respectively.

Table 4.2: Comparison between 3-set sensor and 4-set sensor

	2nd generation 3-set sensor	3rd generation 3-set sensor	3rd generation 4-set sensor	Unit
Average error	1.2	0.40	0.37	degree
Maximum error	3.49	3.61	1.47	degree
Minimum sensitivity	0.21	1.8	8.3	mV/degree

4.4.3 Control with the First Generation

To evaluate the capability of the first-generation rotation sensor in controlling the SMA torsion module, an experimental setup was developed as shown in Figure 4.20(a). The fiberoptic rotation sensor is mounted on the SMA torsion module using super glue. After fixing the torsion module with the rotation sensor on the setup, the output end of the shaft of the torsion module is connected to a rotary encoder (US Digital®, USA) via a connective shaft. Stepwise position references are designed with a 30 s step time and a 40° step size for three steps. A PI controller is developed based on the feedback of fiberoptic rotation sensor to selectively heat one of the SMA springs for positive rotation. The PI controller calculates the required heating intensity and the heating intensity is converted to the PWM intensity of the voltage input to a MOSFET (International Rectifier, USA) between the SMA spring and the power supply. Figure 4.20(b) shows the comparison between the designed references and the measurements by the rotary encoder. It shows that the SMA torsion module can achieve relatively precise tracking with an average steady-state error of 0.21°. The difference in the transient response for the three steps is caused by the nonlinearity of the SMA torsion module. In addition, a NICHE robot is equipped with a fiberoptic rotation sensor for proof-

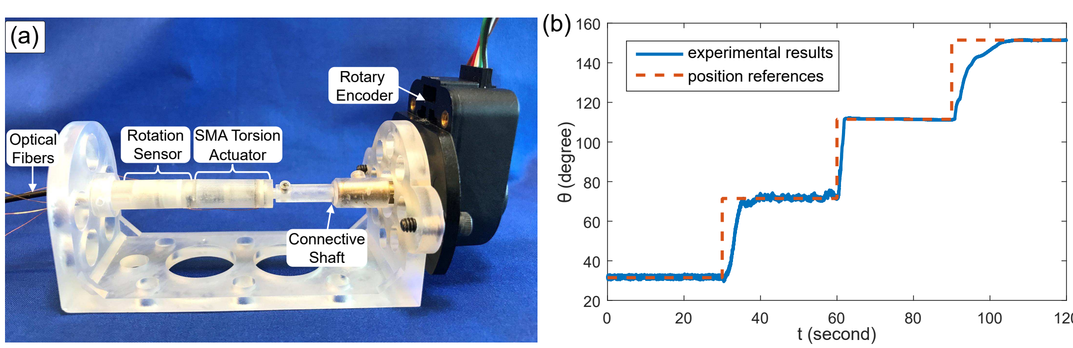

Figure 4.20: Feedback control of the SMA torsion module integrated with the first-generation sensor: (a) experimental setup and (b) comparing the actual rotation angles with stepwise references.

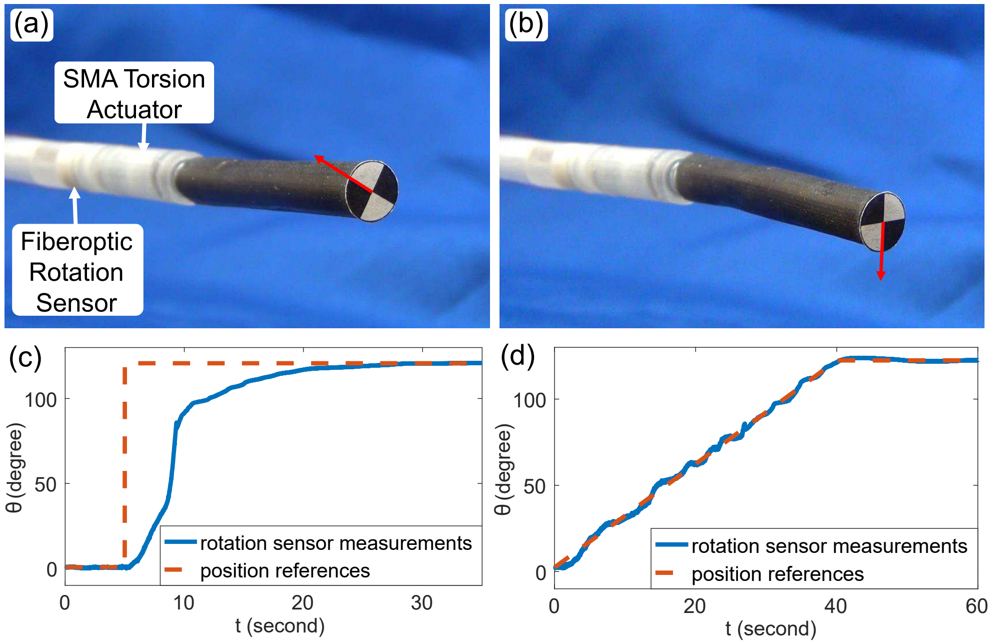

Figure 4.21: Feedback control of the tip articulation of the NICHE robot integrated with the first-generation sensor: (a-b) initial (a) and final (b) robot configuration for a 120° step input to the SMA torsion module, (c) measurements of the fiberoptic rotation sensor for the step input, and (d) measurements of the fiberoptic rotation sensor for the linear position references.

of-concept demonstrations. Figures 4.21(a) and (b) show the rotation of the SMA torsion module for a 120° step input under a PI controller. Figure 4.21(c) shows the measurements of the fiberoptic rotation sensor and the steady-state error is 0.16° at 35 s. A similar demonstration is performed with linear references. As shown in Figure 4.21(d), the average tracking error is 1.27° and the steady-state error is 0.19° at 60 s. Note that the actual tracking error is probably larger than the error based on the measurements of the fiberoptic rotation sensor due to measurement errors.

4.4.4 Control with the Third Generation

To evaluate the working performance of the third-generation sensor, a NICHE robot integrated with the third-generation sensor is fixed on a holder and a vision marker is placed at the robot tip, as shown in Figure 4.22(a). A stereo camera is used to track the 3D position of the vision marker. The power supply outputs a constant 2 A electric current and the heating intensity is controlled by a PI controller using PWM, as described in Section 4.4.3. The upper limit of the duty cycle is set to be 30% to prevent overheating.

To begin with the experiment, the bending tip is deflected by applying 1 A electric current for 5 s and the bending tip can maintain a slightly deflected configuration after the natural cooling of the bending tip. Therefore, the vision marker follows a circular path when the torsion module is energized. Figure 4.22(b) shows an image of the NICHE robot in the initial configuration acquired by the stereo camera. The tracking reference is a 250° step input and the experiment is repeated by three times. Before each test, the torsion module will be returned to the home position using the method in Section 2.3.2. Figure 4.22(c) shows an image of the NICHE robot when it reaches the target configuration. From the data acquired by the stereo camera, it is observed that the vision

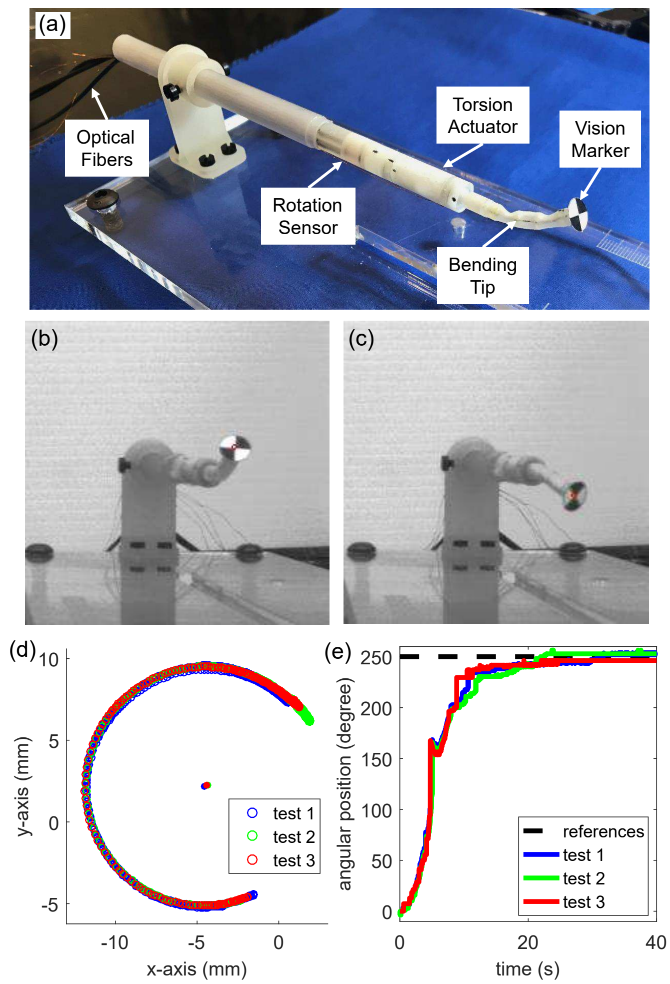

Figure 4.22: Feedback control of the tip articulation of the NICHE robot integrated with the third-generation sensor: (a) experimental setup, (b) robot at the initial configuration, (c) robot at the final configuration, (d) position of the vision marker in the x-y plane during robot tip articulation, and (e) measurements by the third-generation fiberoptic rotation sensor.

marker has a negligible position variation in the z-axis and the position change in the x-y plane is shown in Figure 4.22(d). The 2D position data in the three tests is individually fitted by a circle, so that the rotation center can be estimated, as shown by the dots in Figure 4.22(d). Thus, the rotation range can be computed based on the estimated rotation center and the position of the vision marker. Figure 4.22(e) shows the measurements by the fiberoptic rotation sensor. The average steady-state error is about 2.47° and the standard deviation value is about 3.62°. The rotation radius is estimated to be 7.5 mm, which means the positioning accuracy is about 0.32 mm. If the robot tip is deflected more to achieve the maximum rotation radius and workspace, as shown in Figure 2.6, the positioning error is about 0.86 mm. Therefore, the target positioning accuracy proposed in Chapter 2 can be satisfied for a constant rotation radius of the robot tip.

4.5 Discussion and Conclusions

In this chapter, a fiberoptic rotation sensor is proposed for the motion feedback of the SMA torsion module and the NICHE robot as presented in Chapter 2. The sensing module is primarily comprised of a reflective rotary head mounted on the sensor shaft as well as one or multiple sets of optical fibers. Each fiber set contains both transmitting and receiving fibers. The light beam emitted by each fiber set can be modulated by the reflective rotary head, which can rotate with the torsion module via the sensor shaft. Thus, the light intensity received by receiving fibers is modulated, resulting into varying analog output. The working principle is analytically modeled by considering the light flux into each fiber set from all fiber sets. The modeling shows that the sensitivity of the device can be improved by using more sets of optical fibers. To improve sensitivity, a brass mirror is fabricated and used as the reflective surface on the top of the rotary head in the latest generation. The developed fiberoptic rotation sensor is experimentally calibrated. Based on the calibration results, the developed sensor is capable of achieving high measurement precision down to about 1° for a large range of motion. Experimental studies show that the average error is reduced by increasing the reflective rate of the sensor reflector and the maximum error is reduced by using more optical fiber sets. When the SMA torsion module is controlled in the closed-loop mode using the fiberoptic rotation sensor, the NICHE robot can achieve sub-millimeter positioning accuracy.

CHAPTER 5

LARGE-CURVATURE FBG BENDING SENSOR

It is challenging to precisely control the SMA bending module presented in Chapter 3 in an open-loop manner due to the nonlinearity of SMA and uncertainties in environmental loading. This chapter presents a Fiber Bragg grating (FBG) bending sensor for the motion feedback of the SMA bending module as a prerequisite for potential closed-loop control. FBG shape sensing is promising for the SMA bending module, since it essentially satisfies the following requirements: 1) able to measure multiple degrees-of-freedom (DoFs) simultaneously; 2) miniature and lightweight for easy integration; 3) compatible with magnetic and radiative medical imaging environment. Since the SMA bending module is capable of large-curvature deflection for challenging manipulation in confined anatomical structures, the sensor should be able to measure large curvatures. In addition, the sensor should be relatively flexible to minimize its influence to the motion capability of SMA bending module, and robust to the temperature variation caused by SMA actuation.

The rest of this chapter is organized as follows. Section 5.2 presents the design, fabrication, and installation of the FBG bending sensor. Section 5.3 presents the working principle of the sensor, followed by the analysis of the sensitivity through model-based simulations. Section 5.4 presents several experimental studies to calibrate the sensor and evaluate the sensor integrated with the SMA bending module. Section 5.5 concludes the chapter.

5.1 Hardware Development

5.1.1 Sensor Design

The design of the FBG bending sensor integrated with the SMA bending module integrated is shown in Figure 5.1(a). As presented in Chapter 3, the SMA bending module consists of two rigid links and a pair of antagonistic SMA wires between the two links. The bending module can be deflected bi-directionally by heating individual SMA wires. By integrating multiple SMA bending modules. As shown in Figure 3.1, by threading a flexible sleeve outside the SMA bending module, the FBG

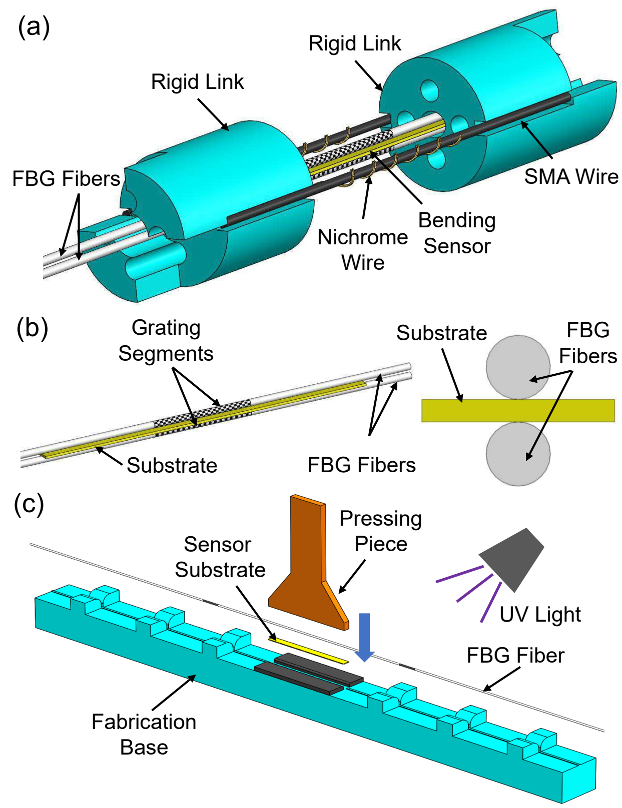

Figure 5.1: System design and fabrication: (a) SMA bending module integrated with the FBG bending sensor, (b) design of the FBG bending sensor, and (c) fabrication of the FBG bending sensor.

bending sensor is physically and thermally insulated from external tissue and blood.

Figure 5.1(b) shows the design of the FBG bending sensor. The sensor is comprised of two 190 μm diameter FBG fibers (FBGS, Jena, Germany) with a grating segment per fiber and each fiber is bonded onto one side of an ultra-thin superelastic Nitinol substrate using adhesive. Since the two FBG fibers are orthogonal to the two SMA wires, as shown in Figure 5.1(a), the two grating segments will be symmetrically heated when one of the SMA wires is thermally actuated, resulting in the equivalent change in the performance characteristics of the two FBG fibers. If the FBG fiber contain multiple grating segments and multiple substrates are used, a multi-DoF bending sensor can be developed. In this study, we focus on the development of an one-DoF FBG bending sensor for the SMA bending module. To integrate the sensor with the SMA bending module, a sliding hole is made in the center of each rigid link to accommodate the FBG bending sensor, as shown in Figure 5.1(a). The proximal end of the sensor is fixed inside the sliding hole of the proximal link, while the distal end is allowed to slide in the hole when the bending sensor is deflected. If both ends are fixed, the sensor will tend to buckle due to the flexibility of the sensor. The FBG fibers are connected to a signal interrogator (FBGS, Jena, Germany), which transmits a light beam into each FBG fiber. Due to the grating segment on the FBG fiber, light of a particular wavelength is reflected and measured by the interrogator. Once the sensor is deflected, the measured wavelength of the reflected light will be shifted. Based on the properties of the FBG fiber, the wavelength shift is proportional to the axial strain in the fiber, which is further correlated to the curvature of the bending sensor. The details of the working principle will be explained in Section 5.2.

5.1.2 Sensor Fabrication

The ultra-thin Nitinol substrate is 76.2 μm in thickness and 800 μm in width. It is fabricated by cutting a strip from a superelastic Nitinol film (Kellogg's Research Labs, Hudson, NH, USA) using wire EDM. As show in Figure 5.2(a), the heat affected zone on the substrate is negligible. To bond FBG fibers onto the substrate, a jig in 3D-printed in plastic material and used to ensure the alignment between the fibers and substrate during the bonding process, as shown in Figure 5.1(c). The first step is to place the substrate inside the recess in the center of the jig. Flexible ultraviolet (UV)-cured glue (Solarez, Vista, CA, USA) is then applied along the centerline of the substrate. By pressing the FBG fiber into the grooves on the jig, the FBG fiber is aligned with the substrate. Since the

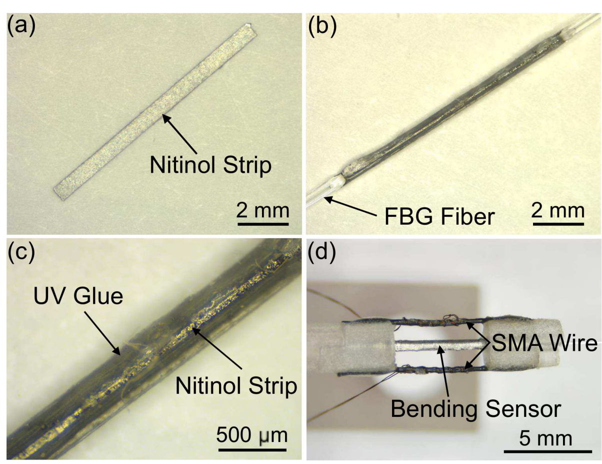

Figure 5.2: System prototypes: (a) superelastic Nitinol strip, (b) FBG bending sensor, (c) zoom-in sagittal view of the sensor, and (d) SMA bending module integrated with the sensor.

grating segment is located between the two markers on the fiber, the centers of the grating segment and the substrate can be manually aligned. By shining UV light for 30 s while pressing the fiber against the substrate using a pressing piece, the FBG fiber is bonded with the substrate. The other FBG fiber can be bonded in the same way. Thereafter, UV-cured glue is evenly applied along the two FBG fibers and then cured to secure the bonding. In the end, the fabricated sensor is inserted through the sliding holes of the SMA bending module. Super glue is used to fix the proximal end in the sliding hole and grease is applied on the distal end to reduce the friction in the sliding hole. Figures 5.2(b) and (c) show the overview and close-up view of the substrate with an FBG fiber on one side. Figure 5.2(d) shows the SMA bending module equipped with the FBG bending sensor.

5.2 Sensor Modeling

5.2.1 Fiber Bragg Grating

The wavelength of the reflected light in an FBG fiber is determined by the effective refractive index of the grating as well as the grating period. Both are linearly affected by the axial strain and temperature. It is assumed the initial axial strain is zero. Thus, the wavelength shift is given by [104]:

$$\Delta\lambda = k_T \Delta T + k_\epsilon \epsilon_f^0 \tag{5.1}$$

where $\Delta\lambda$, ΔT, and ϵ_f^0 are the wavelength shift, temperature change, and axial strain, respectively. k_T and k_ϵ are the coefficients for the influence of temperature and strain, respectively. When the SMA wires of the bending module are energized, the temperature of the grating segments will vary due to natural convection. Due to the orthogonal placement of the SMA wires and FBG fibers (see Figure 5.1), the temperature changes of the two grating segments are equivalent, which will be verified in Section IV.B. Thus, the temperature influence can be compensated by using the difference between the wavelength shifts of the two fibers as the sensor output, which yields:

$$y = \Delta\lambda_1 - \Delta\lambda_2 = k_\epsilon(\epsilon_{f1}^0 - \epsilon_{f2}^0) \tag{5.2}$$

where y, $\Delta\lambda_i$ and ϵ_{fi}^0 (i = 1 or 2) are the sensor output, wavelength shift, axial strain, respectively. The curvature is assumed to be consistent along the grating segments. Thus, the modeling objective is to find the relationship between y and the sensor curvature, κ.

5.2.2 Strain Transfer Model

Since the adhesive and the coating layer of the FBG fibers are flexible, the shear stress across them is the primary stress that induces normal strain in the fibers. Thus, a strain transfer model is developed to model the working principle of the proposed sensor. A simplified analytical model is adapted from [69] and shown in Figure 5.3(a). The analytical model consists of a substrate in the middle with an adhesive layer, a coating layer, and a fiber core on each side. The properties of these layers are denoted by variables with subscripts 's', 'a', 'c', and 'f', respectively. If a subscript contains 'i' (1 or 2), the corresponding variable is particularly for the upper or lower layers, respectively. When the sensor is deflected as shown in Figure 5.2(b), positive and negative normal strain will be induced on the top surface of the substrate and the bottom surface of the upper fiber core, respectively. The potential relative displacement between these two surfaces will induce shear stress in the coating layer and adhesive, which compresses the substrate and stretches the fiber core in return. Hence, positive axial strain will be induced in the upper fiber core. The same principle can be applied to explain the negative axial strain in the lower fiber core. The adhesive and coating on the two sides and above the core of the FBG fiber are neglected, as their contributions to axial strain in the fiber core is negligible [105].

In this work, it is assumed that only longitudinal shear stress is transferred in the coating and adhesive. For each circular sub-layer of the coating, the shear force applied on its upper surface is equal to that applied on its lower surface. Thus, the shear stress, τ_c, is inversely proportional to the radius of the sub-layer, r, which yields: $\tau_c(r,\theta,x) = \frac{r_c}{r}\tau_{ac}(\theta,x)$, where τ_{ac} and r_c are the shear force and radius at the coating-adhesive interface, respectively. The definitions of θ and x are shown in Figure 5.3. The difference between the displacements of the substrate-adhesive interface and the core-coating interface, Δu_i, is given by:

$$\Delta u_1 = u_s^{+s} - u_{f1}^{-s} \tag{5.3}$$

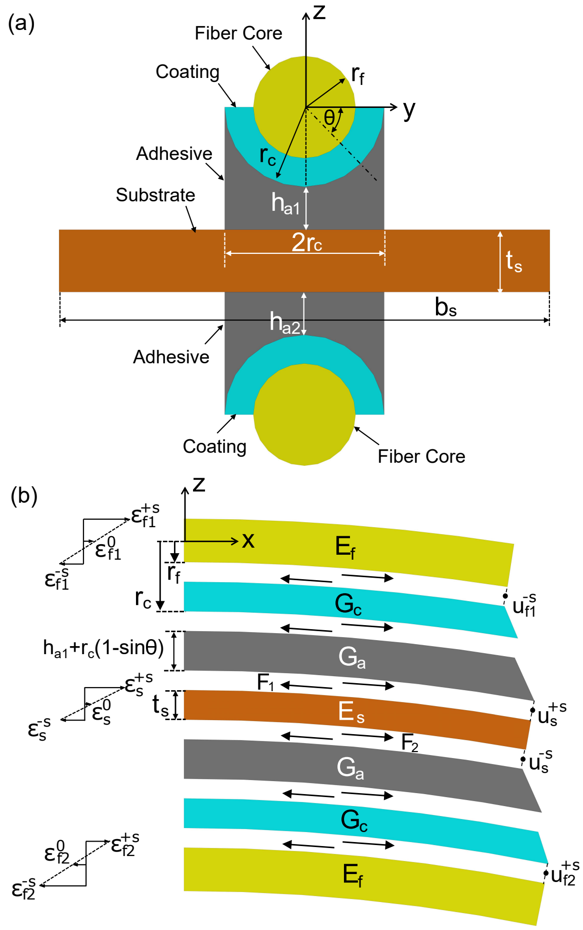

Figure 5.3: Analytical model of the FBG bending sensor: (a) cross-section view and (b) sagittal view.

$$\Delta u_2 = u_{f2}^{+s} - u_s^{-s} \tag{5.4}$$

where u_s^{+s}, u_s^{-s}, u_{f1}^{-s}, and u_{f2}^{+s} are the displacement at the top surface of the substrate, bottom surface of the substrate, bottom surface of the upper fiber core, and top surface of the lower fiber core, respectively. Based on the assumptions of linear elasticity and uniform strain in the half length of the substrate, shear stress in the coating and adhesive is determined by Δu_i, and the shear force is given by [69]:

$$F_i = \frac{L_s}{2} \int_0^{\pi} \frac{\Delta u_i}{\frac{h_a + r_c - r_c \sin\theta}{G_a} + \frac{r_c}{G_c} \ln(\frac{r_c}{r_f})} r_c d\theta \tag{5.5}$$

where L_s, h_{ai}, r_f, r_c, G_a, and G_c are the sensor length, adhesive thickness, fiber core radius, adhesive-coating interface radius, shear modulus of the adhesive, and shear modulus of the coating, respectively. Note that adhesive thickness, h_{ai}, is probably different for the upper and lower layers due to fabrication variance. In the curved configuration shown in Figure 5.3(b), the shear force in the upper layers stretches the fiber core and compresses the substrate, while the shear force in the lower layers compresses the fiber core and stretches the substrate. Thus, the induced axial strain in the substrate, ϵ_s^0, upper fiber core, ϵ_{f1}^0, and lower fiber core, ϵ_{f2}^0, are respectively given by:

$$\epsilon_s^0 = \frac{-F_1 + F_2}{b_s t_s E_s}, \ \ \epsilon_{f1}^0 = \frac{F_1}{\pi r_f^2 E_f}, \ \ \epsilon_{f2}^0 = \frac{-F_2}{\pi r_f^2 E_f} \tag{5.6}$$

where b_s, t_s, E_s, and E_f are the substrate width, substrate thickness, substrate Young's modulus, and fiber core Young's modulus, respectively. Since the displacements at the coating-core interface and the substrate-adhesive interface are caused by the bending and axial deformation, the displacements are given by:

$$u_s^{+s} = \frac{L_s}{2}(\frac{t_s}{2}\kappa + \epsilon_s^0), \ \ u_s^{-s} = \frac{L_s}{2}(-\frac{t_s}{2}\kappa + \epsilon_s^0) \tag{5.7}$$

$$u_{f1}^{-s} = \frac{L_s}{2}(-r_f\kappa + \epsilon_{f1}^0), \ \ u_{f2}^{-s} = \frac{L_s}{2}(r_f\kappa + \epsilon_{f2}^0) \tag{5.8}$$

By substituting Equations (5.7) and (5.8) into Equation (5.5), and then substituting the results into Equation (5.6), the axial strain of the fiber cores and substrate can be derived. The difference between the axial strain of the two fibers is thereby calculated and the sensor output is given by:

$$y = S\kappa = \frac{k_\epsilon K_f(I_1 + I_2 + 4K_s I_1 I_2 + 2K_f I_1 I_2)(\frac{t_s}{2} + r_f)}{1 + (K_s + K_f)(I_1 + I_2) + (2K_s + K_f)K_f I_1 I_2}\kappa \tag{5.9}$$

where

$$K_s = \frac{L_s^2 r_c}{4 b_s t_s E_s}, \ \ K_f = \frac{L_s^2 r_c}{4\pi r_f^2 E_f} \tag{5.10}$$

$$I_i = \int_0^\pi \frac{1}{\frac{h_{ai} + r_c - r_c \sin\theta}{G_a} + \frac{r_c}{G_c}\ln(\frac{r_c}{r_f})} d\theta \tag{5.11}$$

The modeling results show that the proposed sensor has a constant sensitivity, denoted by *S*.

5.2.3 Simulations

Two special cases are considered. In case I, the two adhesive layers are assumed to have the same thickness. Thus, $I_1 = I_2 = I$ and the sensitivity is rewritten as:

$$S = \frac{k_\epsilon K_f I(t_s + 2r_f)}{4(1 + K_f I)} \tag{5.12}$$

In case II, only one FBG fiber is bonded with the substrate (unilateral design). Without loss of generality, the upper fiber in Figure 5.3 is assumed to be bonded. Thus, $I_1 = I$ and $I_2 = 0$, and the sensitivity can be rewritten as:

$$S = \frac{k_\epsilon K_f I(t_s + 2r_f)}{2(1 + K_s I + K_f I)} \tag{5.13}$$

These two equations show that the sensitivity is independent of E_s and b_s, but linearly changes against t_s. Since the bending sensor should possess sufficient sensitivity and low bending stiffness, and the bending stiffness of the substrate is proportional to b_s, E_s, and the cube of t_s, E_s and b_s is preferred to be small. Since t_s affects the bending stiffness more significantly than the sensitivity, t_s should be sufficiently small. Hence, the substrate is designed to be ultra-thin and fabricated from an ultra-thin superelastic Nitinol film. It is not practical to adjust some of the design parameters, including L_s, r_f, G_c, and G_f, since L_s is determined by the length of the bending module, and r_f, G_c, and G_f are determined by the off-the-shelf FBG fibers. The influence of G_a, h_a, are r_c on the sensitivity is investigated by conducting model-based simulations. The value of G_a can potentially be adjusted by mixing flexible and rigid UV-cured glue. By fixing the values of other parameters, which are provided by manufacturers and listed in Table 5.1, the sensitivity against G_a is simulated for both cases. h_a will be experimentally estimated in Section IV.A.

As shown in Figure 5.4(a), the sensitivity increases with increasing G_a and asymptotically converges to about 240.4 pm and 96.5 pm for case I and case II, respectively. This is because the shear force increases when the shear modulus increases for a certain amount of potential relative displacement. The value of h_a can potentially be adjusted by controlling the force applied to press the fiber

Table 5.1: Mechanical properties of FBG bending sensor

E_f	G_c	G_a	E_s	r_f	r_c	b_s	t_s	l_f	h_a
GPa	GPa	MPa	GPa	μm	μm	μm	μm	mm	μm
70	0.66	2.91	55	62.5	97.5	830	76.2	10	170

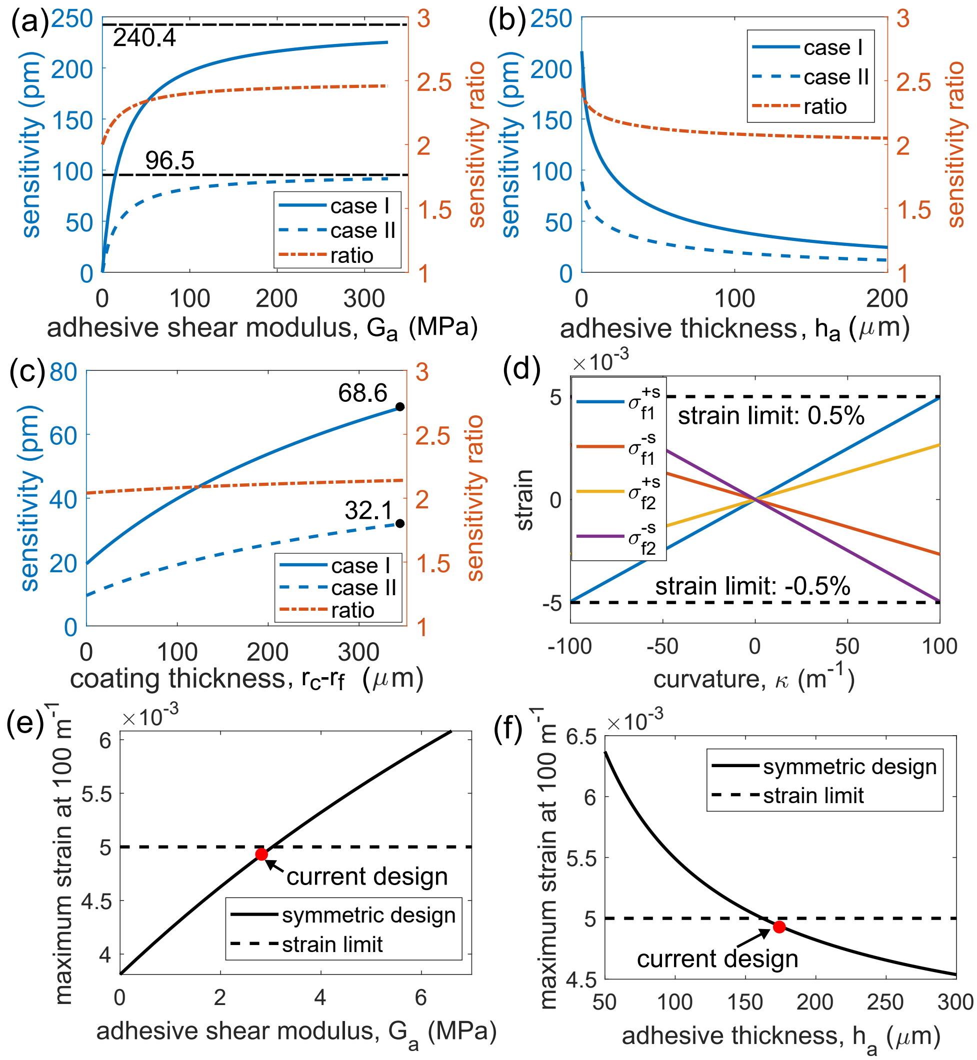

Figure 5.4: Simulation results: (a) sensitivity versus adhesive shear modulus, G_a, (b) sensitivity versus adhesive thickness, t_s, (c) sensitivity versus coating thickness, $r_c - r_f$, (d) strain at the upper and lower edges of the upper and lower fibers versus curvature for current design, (e) maximum strain in the fibers versus adhesive shear modulus at the curvature of 100 m^{-1}, and (f) maximum strain in the fibers versus adhesive thickness at the curvature of 100 m^{-1}. Ratio is the sensitivity of case I to case II. The red dot indicates the current design.

against the substrate during UV curing. As shown in Figure 5.4(b), the sensitivity decreases as the adhesive thickness increases and asymptotically converges to zero for both cases. This is because the shear strain decreases if the adhesive thickness increases, resulting in smaller shear force that induces smaller axial strain. The value of r_c can potentially be adjusted by customizing the coating. The lower and upper limits of r_c are set to be r_f and $\frac{b_s}{2}$, respectively. As shown in Figure 5.4(c), by increasing the coating thickness, $r_c - r_f$, the sensitivity is improved for both cases. Since the shear modulus of the coating is much higher than that of the adhesive, the average shear modulus increases when the coating thickness increases, resulting in the increase of the shear stress. These simulation results also show that the sensitivity ratio between case I and case II is almost two and the improvement of the sensitivity by adjusting G_a, h_a, and r_c is possible but limited. To keep the normal strain of the fibers under the strain limit (0.5% [70]), the strain at the upper and lower edges of the two fibers at different curvatures is simulated, as shown in Figure 5.4(d). It shows that the maximum strain (absolute value) occurs at the upper edge of the upper fiber and the lower edge of the lower fiber. The maximum strain can be kept within the strain limit at large curvatures due to the flexible adhesive and ultra-thin substrate . Figures 5.4(e) and 5.4(f) show the change of the maximum strain versus adhesive shear modulus and adhesive thickness, respectively, at the curvature of 100 m^{-1}.

5.3 Experimental Studies

This section presents the experimental evaluation of the FBG bending sensor. I would like to acknowledge Ms. Nancy J. Deaton for collaborating on the experiments and data analysis.

5.3.1 Model Evaluation

The developed model was experimentally evaluated by using a unilateral bending sensor. As shown in Figure 5.5(a), a mold with curved slots of different curvatures (0 to 66.67 m^{-1}) is 3D-printed in plastic material. After constraining the sensor inside a curved slot, the wavelength shift is measured. The test was repeated by three times for each curvature. Figure 5.5(b) shows the wavelength shift versus the slot curvature. Based on Equation (5.13), the adhesive thickness is estimated to be 170 μm using the least-square approach. The RMSE and R^2-value are about 123 pm and 0.9543, respectively. The close match between the model predictions and experimental results proves the validity of the developed model, which can serve as a tool to optimize the sensor design in the future. The difference between the model predictions and experimental results can be explained by the normal force applied by the sidewall of the slots on the sensor, asymmetry of the adhesive along the fiber, difference between the curvatures of the slots and the sensor due to the gap between them,

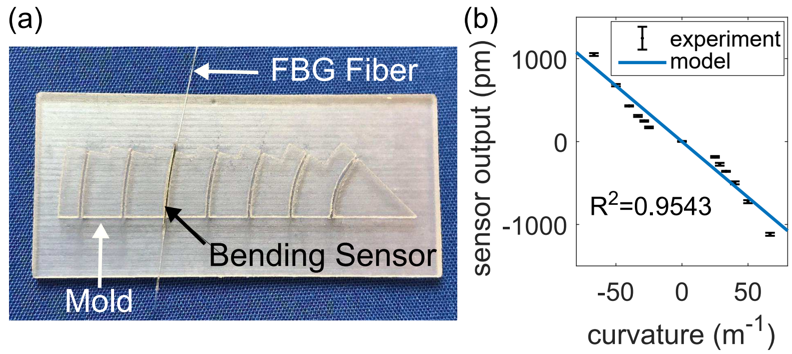

Figure 5.5: Experimental model evaluation: (a) bending sensor constrained in a curved slot on a model and (b) comparison between the experimental results with model predictions.

and model uncertainty. The adhesive thickness is primarily determined by the manual force applied on the fiber against the substrate, as shown in Figure 5.1(c). It may vary across fabricated sensors, but it is not an issue since each sensor can be individually calibrated. In addition, the influence of the difference in adhesive thickness on the sensitivity becomes insignificant when the adhesive is thicker than 100 μm, as shown in Figure 5.4(b).

5.3.2 Temperature Influence on Sensor Output

To evaluate the influence of temperature variation on FBG sensing, the grating segment of an FBG fiber was heated on a hot plate and an RTD sensor was bonded with the grating segment to measure the temperature. As shown in Figure 5.6(a), the wavelength shift changes against temperature linearly. By using linear regression, the sensitivity, RMSE, and R^2-value are estimated to be 13.22 pm/^{o}C, 5.37 pm/^{o}C, and 0.9994, respectively. Another test was performed to verify the equiv-

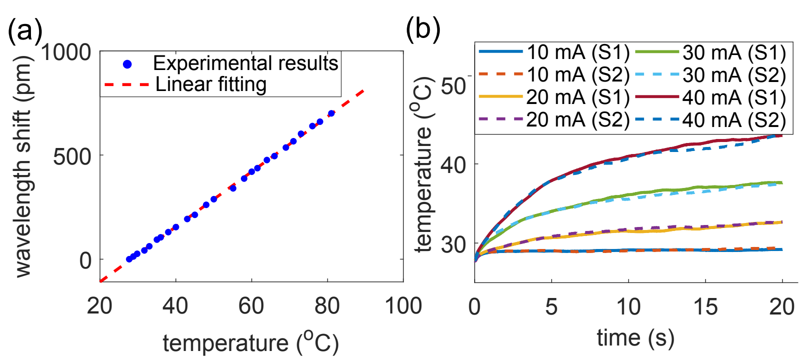

Figure 5.6: Analysis of temperature influence: (a) wavelength shift with temperature change and (b) temperature measurements of the two grating segments.

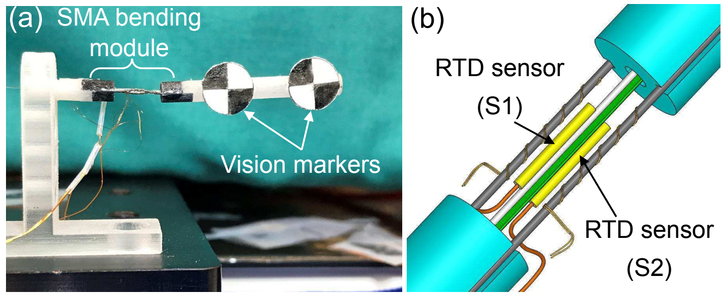

Figure 5.7: Experimental setup: (a) photo showing vision markers attached to the SMA bending module and (b) schematic showing the placement of RTD sensors.

alent temperature changes of the two grating segments in the SMA bending module. As shown in Figures 5.7(a) and (b), two RTD sensors are bonded on the two sides of the bending sensor. Constant electric current was applied to one SMA wire and the test was repeated by three times for each current level. Figure 5.6(b) shows the average temperature change versus time. The average difference between the temperature measurements of the two RTD sensors is about 0.073 ^{o}C, which proves the equivalent temperature changes of the two grating segments due to the orthogonal configuration of the FBG fibers and SMA wires.

5.3.3 Sensor Influence on Motion Range

To evaluate the influence of the developed sensor on the motion capability of the SMA bending module, the sensor was integrated with an SMA bending module. The bending module was actuated bi-directionally for 40 cycles, while the motion range was measured by tracking the two markers

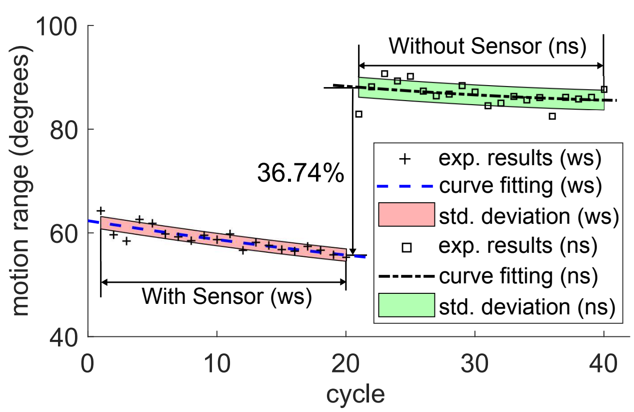

Figure 5.8: Motion range of the SMA bending module versus motion cycles (sensor is removed after the 21st cycle).

attached on the bending module using a stereoscopic camera, as shown in Figure 5.7(a). In each cycle, 40 mA current was alternately applied to one of the SMA wires for 5 s, followed by a 30 s natural cooling period. After the 20$^{\text{th}}$ cycle, the sensor was removed. Figure 5.8 shows the motion ranges versus test cycles. The two groups of results before and after the sensor was removed are individually modeled using a second-order polynomial regression. By comparing the predicted motion ranges at the 20$^{\text{th}}$ and 21$^{\text{st}}$ cycle, the decrease of the motion range of the SMA bending module is estimated to be 36.74%. This result proves that the SMA bending module maintains the majority of its motion range due to the relatively small bending stiffness of the developed sensor. The bending stiffness of the sensor can be reduced further by reducing the width and thickness of the substrate or using softer material as the substrate, as discussed in Section 5.2.3. When the FBG fibers were bonded by applying rigid adhesive through the substrate or at the two ends of the substrate, similar to the methods in related works [69, 72, 73, 106–108], the bending stiffness of the fabricated sensor became so high that the SMA bending module could hardly deflect due to the significant reinforcement effect of the rigid adhesive.

5.3.4 Evaluation of the Integrated Sensor

The sensor was integrated with the SMA bending module to evaluate its working performance. By applying a constant electric current to individual SMA wires, the bending module was deflected bi-directionally and the stable angle was measured by the stereoscopic camera. The experiment was performed after fatiguing the sensor/actuator assembly by 10 cycles. Figures 5.9(a) and (b) show the sensor output versus the bending angle in the relatively large and small motion ranges, when the electric current is increased from 0 to 38 mA and 0 to 30 mA, respectively. In both cases, hysteresis is observed, due to the friction applied on the sensor at the sliding end. The friction applied on the two fibers is opposite and reversed at the critical straight configuration. To reduce the friction and hysteresis, other smoother materials can be used to fabricate the rigid links, and a frictionless sheath can be placed inside the sliding hole. It is also observed that the sensitivity is not a constant value, probably due to the high sensitivity of FBG sensing to the torsional motion of the bending module [109]. Another reason is that the curvatures of the sensor and bending module are slightly different due to the tolerance between them and the difference varies against the bending angle.

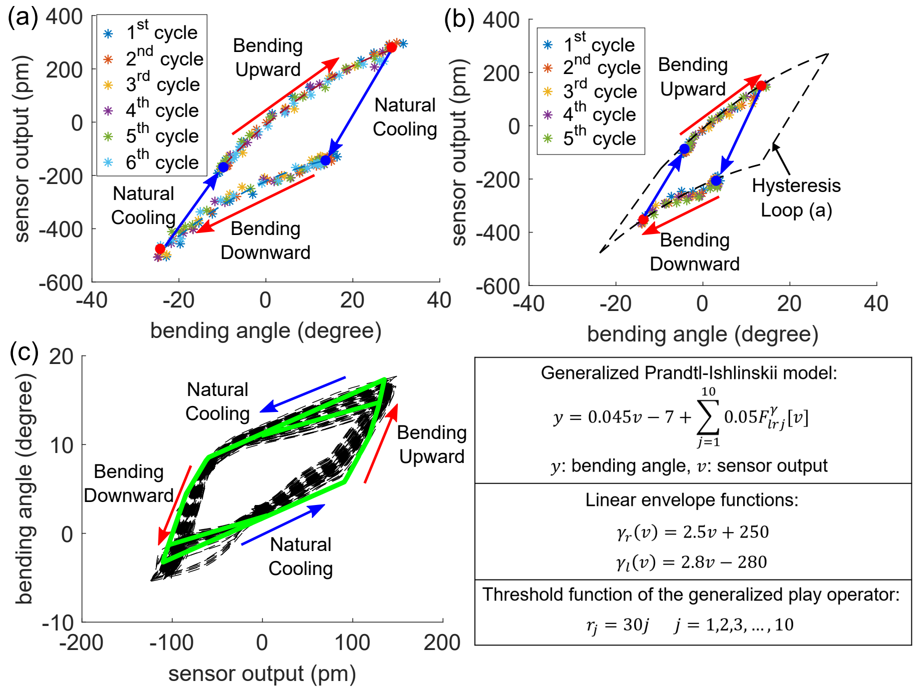

Figure 5.9: Calibration results of the FBG bending sensor integrated with the SMA bending module: (a) electric current increased from 0 to 38 mA, (b) electric current increased from 0 to 30 mA (hysteresis loop (a) denotes the hysteresis loop in figure (a)), (c) experimental results of 100 cycles with the Prandtl-Ishlinskii hysteresis model.

As shown in Figure 5.9(a), a piecewise phenomenological model is used to individually fit the results of the upward and downward bending using a second-order polynomial regression. The RMSE and R^2 values for individual cases are listed in Table 5.2. Since the maximum bending angle is about 29° and the distance between the two rigid links is about 6.5 mm, the maximum

Table 5.2: Results of model fitting and measurement error

motion type	direction	item	value	unit
large-range	upward	RMSE	13.16	pm
		R-squared	0.99	-
		error	-0.07±1.56	degree
	downward	RMSE	15.39	pm
		R-squared	0.98	-
		error	-0.11±2.19	degree
small-range	upward	RMSE	18.75	pm
		R-squared	0.98	-
		error	1.12±0.88	degree
	downward	RMSE	16.81	pm
		R-squared	0.92	-
		error	1.08±1.78	degree

measurable curvature is estimated to be 77.87 m^{-1}. Compared to the maximum measurable curvature reported in the literature (66.66 m^{-1} [73]), the developed sensor achieved 16.8% improvement in the measurement capability. As analyzed in Section 5.2, this improvement is attributed to the ultra-thin superelastic substrate and flexible adhesive, which control the strain of FBG fibers within the strain limit at large curvatures. Another 100 cycles were operated by alternately applying 30 mA to individual SMA wires. The bending angle versus the sensor output is modeled using the Prandtl-Ishlinskii model and least-square approach [110], as shown in Figure 5.9(c). The RMSE is about 1.98°, which proves the relatively high repeatability of the developed sensor. To evaluate the measurement accuracy of the sensor, the bending direction is assumed to be pre-known, and the piecewise phenomenological model is utilized to calculate the bending angle based on the sensor output. Table II shows the relatively small measurement error for all the cases in Figures 5.9(a) and (b).

5.4 Discussion and Conclusions

In this chapter, an FBG bending sensor is proposed for the motion feedback of the SMA bending module. Due to the large curvatures memorized by SMA wires, the SMA bending module is capable of large-curvature deflection. Therefore, the bending sensor should be able to measure large curvatures. This objective is achieved by bonding two FBG fibers with an ultra-thin superelastic substrate using flexible adhesive with low shear modulus. Thus, the induced strain in FBG fibers can be controlled within the strain limit at large curvatures. Since the two FBG fibers are orthogonal to the two SMA wires, the two fibers will be equally heated via natural convection when either SMA wire is heated. The working principle was analytically modeled, which indicates the trade-off between the maximum measurable curvature and sensitivity. The sensor integrated with the SMA bending module shows relatively small bending stiffness, high repeatability, and high measurement precision, although hysteresis is observed during cyclic motion. Experimental studies show that the sensor is able to measure the deflection of the SMA bending module up to a curvature of 77.87 m^{-1}, which is about a 16.8% improvement compared to the state of the art.

CHAPTER 6

NEUROSURGICAL ROBOTIC HEADFRAME

To manipulate a meso-scale surgical robot, a robotic guiding system is required. When a standalone robot is used, continuous imaging-based registration is required and patients have to be fully immobilized [111]. Standalone parallel robots have been explored to manipulate surgical tools with high precision [112, 113]. By installing a guiding system on a stereotactic frame, the imaging-based registration can be simplified and patient immobilization becomes unnecessary [114]. To reduce the system footprint and improve patient comfort, skull-mounted robotic headframes have been explored. Miniaturized Stewart platforms were developed as skull-mounted guiding systems for intracranial neurosurgery [115–117]. A tendon-driven skull-mounted parallel headframe with two rotational DoFs and two translational DoFs was developed for neurosurgery [118]. To perform intracranial neurosurgery using the NICHE robot presented in Chapter 2, this chapter will present a lightweight skull-mounted headframe based on a parallel platform.

The rest of this chapter is organized as follows. Section 6.1 presents the design, fabrication, and installation of the FBG bending sensor. Section 6.2 presents the working principle of the sensor, followed by the analysis of the sensitivity through model-based simulations. Section 6.3 presents several experimental studies to calibrate the sensor and evaluate the sensor integrated with the SMA bending module. Section 6.4 concludes the chapter.

6.1 Hardware Development

6.1.1 System Design and Installation

Figure 6.1(a) shows the robotic headframe prototype mounted on a human skull model. Typical intracranial neurosurgery uses pre-operative imaging to reconstruct the 3D anatomical structures around the surgical region, whereby surgeons can identify the target and plan an insertion trajectory that causes the minimum interruption to healthy tissue. The entry point on the skull is then determined and a burr hole is drilled at the entry point. To mount the developed headframe, its pedestal is

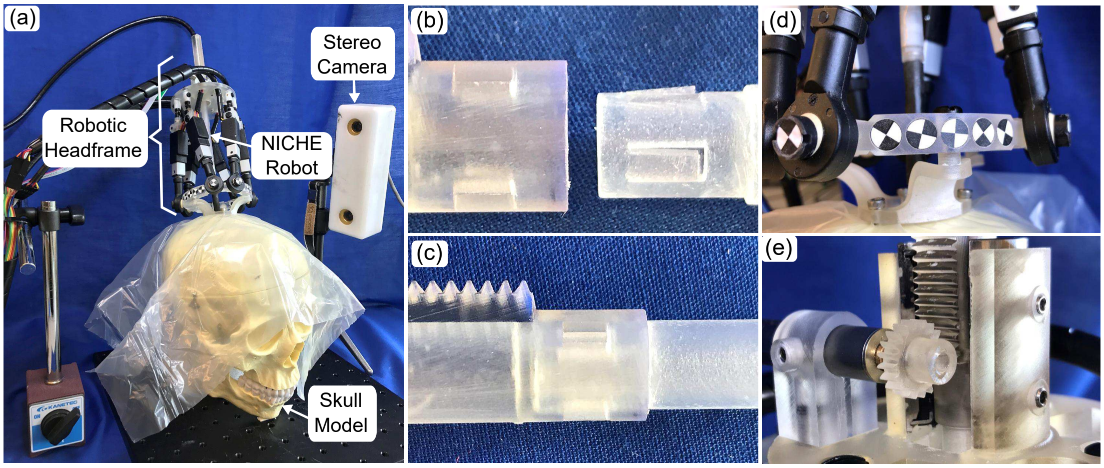

Figure 6.1: Robotic headframe prototype: (a) headframe mounted on a human skull model, (b) snap-fit mechanism, to attach the NICHE robot to the rack, (c) NICHE robot attached to the rack, (d) vision markers placed around the base plate of the headframe, and (e) rack actuated by a DC motor via a pinion.

concentrically aligned with the burr hole and fixed on the skull using three bone anchoring screws, as shown in Figure 6.2(a). Three petals branch out from the bottom rim of the pedestal as supporting structures for the installation of the Stewart platform, as shown in Figure 6.2(b). The Stewart platform contains six legs between the top plate and the base plate. Each leg consists of a passive universal joint, an active prismatic joint, and a passive ball joint. A sterile plastic drape with a hole is placed between the pedestal and the Stewart platform to protect the patient from contaminating agents carried by the robot. Meanwhile, as shown in Figure 6.1(b), Figure 6.1(c), and Figure 6.2(c), the NICHE robot is attached to the lower end of the rack on the linear actuation module via a snap-

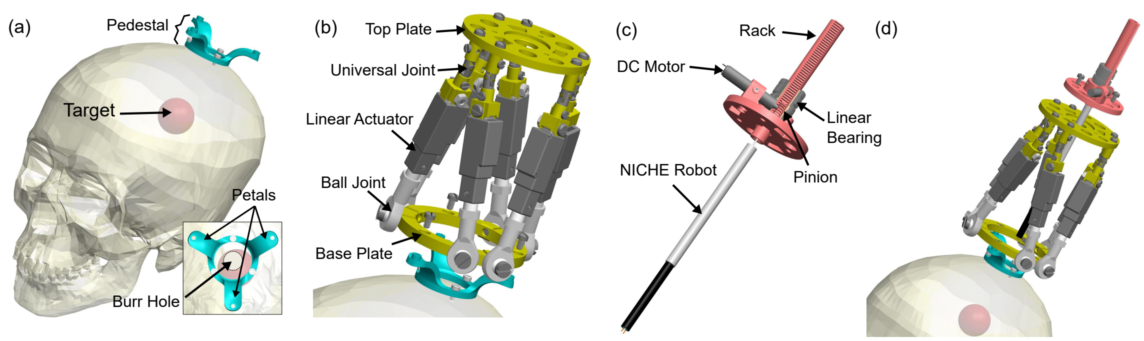

Figure 6.2: Installation of the skull-mounted headframe including: (a) fixing the pedestal using bone anchoring screws, (b) installing the Stewart platform on the pedestal, (c) attaching the NICHE robot to the rack, and (d) installing the linear actuation module interfaced with the NICHE robot onto the Stewart platform.

fit mechanism. As shown in Figure 6.1(e), the rack is coupled with a pinion and actuated by a DC motor with a 1024:1 gearhead (FAULHABER, Croglio, Switzerland), so that it is capable of inserting and retracting the NICHE robot. Electric wires and surgical accessories such as suction tubing can pass through the lumen of the rack and connect to the individual equipment. Finally, the linear actuation module interfaced with the NICHE robot is mounted on the top plate of the Stewart platform, as shown in Figure 6.2(d). After installation, the robotic headframe is registered using an imaging system and then actuated to align the NICHE robot with the planned insertion trajectory.

6.1.2 System Fabrication

To enhance safety and minimize the obstruction for surgeons, the headframe needs to be lightweight, compact, and as small as possible. The developed headframe is about 82 mm in diameter at the base plate and the top plate, and 190 mm tall from the bottom of the pedestal to the top of the linear bearing. Since the NICHE robot is lightweight (about 4.3 g), the payload applied on the headframe is negligible and 3D-printed plastic components (3D Systems, Rock Hill, SC, USA) can sufficiently ensure the structural stability. High manufacturing precision up to 50 μm per 25.4 mm can be achieved. Each prismatic joint is an off-the-shelf linear actuator (Actuonix Motion Devices, Victoria, BC, Canada). Since only fine posture adjustment of the NICHE robot is needed before insertion, all the linear actuators have a small full stroke of 10 mm. In addition, the selected linear actuators have high gear ratio, so that large force up to 45 N can be generated. The ball joints (Igus, Cologne, Germany) are entirely plastic and the universal joints (Huco Dynatork, Hertford, England) are plastic except for brass inserts. The overall load applied on the skull model by the headframe is about 316 g. As shown in Figures 6.1(a) and (d), several vision markers are placed around the circumference of the base plate of the headframe. Thus, a stereo camera can detect the vision markers and the position of the base plate can be estimated during the initial registration process.

6.2 Kinematic analysis

6.2.1 Inverse Kinematics

A conventional method is used to model the inverse kinematics of the robotic headframe. As shown in Figure 6.3(a), the base frame, $\{F_B\}$, and the tool frame, $\{F_T\}$, are located at the center of the upper surfaces of the base plate and the top plate, respectively. The x_b-axis points to one ball joint, the z_b-axis is perpendicular to the plate surface, and $\{F_T\}$ is aligned with $\{F_B\}$ along the z_b-axis at home configuration. Therefore, the position of ball joints with respect to $\{F_B\}$ and universal joints with respect to $\{F_T\}$ is given by:

$$
\begin{aligned}
\boldsymbol{p}_{bi}^{B} &= \begin{bmatrix} r_b C_{\theta_{bi}} & r_b S_{\theta_{bi}} & B_z \end{bmatrix}^T \\
\boldsymbol{p}_{ui}^{T} &= \begin{bmatrix} r_u C_{\theta_{ui}} & r_u S_{\theta_{ui}} & U_z \end{bmatrix}^T
\end{aligned}
\tag{6.1}
$$

where $i \in \{1, 2, 3, 4, 5, 6\}$, $\theta_{bi} \in \{0, \frac{\pi}{2}, \frac{2\pi}{3}, \frac{7\pi}{6}, \frac{4\pi}{3}, \frac{11\pi}{6}\}$, and $\theta_{ui} \in \{\frac{\pi}{6}, \frac{\pi}{3}, \frac{5\pi}{6}, \pi, \frac{3\pi}{2}, \frac{5\pi}{3}\}$. B_z and U_z are the vertical distance from $\{F_B\}$ and $\{F_T\}$ to the ball joints and universal joints, respectively. r_b and r_u are the distance from the center of the base plate and the top plate to the center of each ball joint and universal joint, respectively. C and S denote sin and cos functions, respectively. By

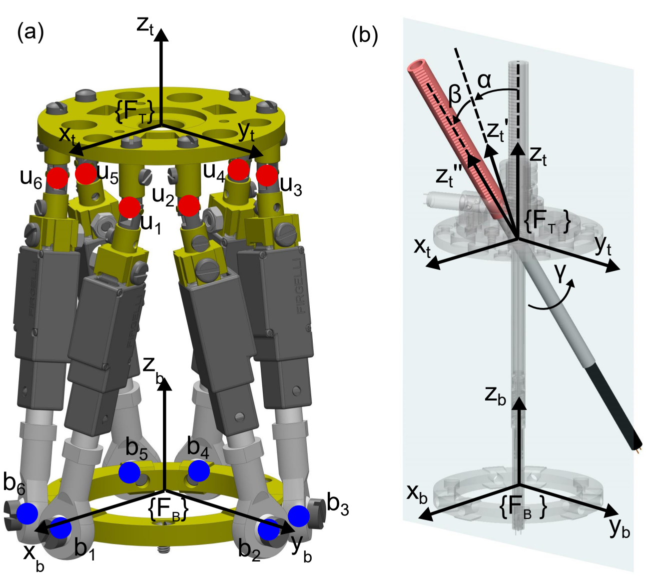

Figure 6.3: Definitions of coordinate frames: (a) coordinate frames for the Stewart platform and (b) Tait-Bryan rotation convection for the linear actuation module.

denoting q_i as the length of each linear actuator, $\boldsymbol{q} = \begin{bmatrix} q_1 & q_2 & q_3 & q_4 & q_5 & q_6 \end{bmatrix}^T$ is the joint space of the robotic headframe. At home configuration, all the linear actuators are at their shortest length.

For the easiness of motion planning in the next subsection, Tait-Bryan angles (α, β, and γ) are used to define the rotation of the NICHE robot with respect to $\{F_B\}$, as shown in Figure 6.3(b). The orientation of the NICHE robot can be decomposed into a series of rotation with respect to the x_t-, y_t'-, and z_t''-axis, and the rotation matrix is given by:

$$\boldsymbol{R}_T^B = \begin{bmatrix} C_\beta C_\gamma & -C_\beta S_\gamma & S_\beta \\ C_\alpha S_\gamma + C_\gamma S_\alpha S_\beta & C_\alpha C_\gamma - S_\alpha S_\beta S_\gamma & -C_\beta S_\alpha \\ S_\alpha S_\gamma - C_\alpha C_\gamma S_\beta & C_\gamma S_\alpha + C_\alpha S_\beta S_\gamma & C_\alpha C_\beta \end{bmatrix} \tag{6.2}$$

The displacement of $\{F_T\}$ with respect to $\{F_B\}$ is denoted by $\boldsymbol{P}_T^B = \begin{bmatrix} x & y & z \end{bmatrix}^T$. Therefore, $\boldsymbol{x} = \begin{bmatrix} x & y & z & \alpha & \beta & \gamma \end{bmatrix}^T$ is the task space of the robotic headframe. The inverse kinematics of the Stewart platform can be solved using the close-loop geometric relationship through each leg of the Stewart platform, which is given by:

$$\boldsymbol{f} = \begin{bmatrix} f_1 & f_2 & f_3 & f_4 & f_5 & f_6 \end{bmatrix}^T \tag{6.3}$$

where $f_i : q_i - \|\boldsymbol{R}_T^B \boldsymbol{p}_{ui}^T + \boldsymbol{P}_T^B - \boldsymbol{p}_{bi}^B\| = 0$.

6.2.2 Motion Planning

After the installation of the headframe interfaced with the NICHE robot, imaging registration can be performed to detect the position of the entry point and the target point with respect to the headframe. The Stewart platform is then actuated to align the NICHE robot with the planned insertion trajectory. As shown in Figure 6.4, since the NICHE robot points towards the entry point, the position of the entry point with respect to $\{F_B\}$, $\boldsymbol{p}_e^B$, is given by:

$$\boldsymbol{p}_e^B = -\|\boldsymbol{p}_e^T\| \boldsymbol{R}_T^B \hat{\boldsymbol{e}}_z + \boldsymbol{P}_T^B \tag{6.4}$$

where $\boldsymbol{p}_e^T$ denotes the position of the entry point with respect to $\{F_T\}$ and $\hat{\boldsymbol{e}}_{\boldsymbol{z}} = [0\ 0\ 1]^T$. similarly, the position of the target point with respect to $\{F_B\}$, $\boldsymbol{p}_t^B$, is given by:

$$\boldsymbol{p}_t^B = -\|\boldsymbol{p}_t^T\| \boldsymbol{R}_T^B \hat{\boldsymbol{e}}_z + \boldsymbol{P}_T^B \tag{6.5}$$

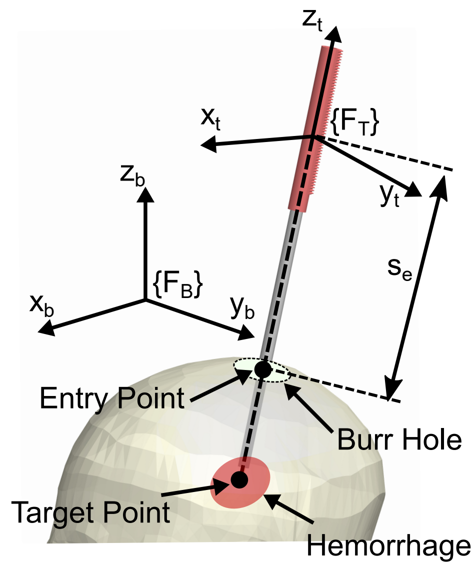

Figure 6.4: Kinematic relationship among the NICHE robot, entry point, and target point.

where $\boldsymbol{p}_t^T$ denotes the position of the target point with respect to $\{F_T\}$. Subtracting Equation (6.5) from Equation (6.4) yields:

$$\boldsymbol{p}_e^B - \boldsymbol{p}_t^B = (\|\boldsymbol{p}_t^T\| - \|\boldsymbol{p}_e^T\|)\boldsymbol{R}_T^B \hat{\boldsymbol{e}}_z \tag{6.6}$$

Since the target point, entry point, and origin of $\{F_T\}$ are simultaneously aligned along the insertion trajectory, $\|\boldsymbol{p}_t^T\| - \|\boldsymbol{p}_e^T\| = \|\boldsymbol{p}_e^T - \boldsymbol{p}_t^T\| = \|\boldsymbol{p}_e^B - \boldsymbol{p}_t^B\|$, where $\boldsymbol{p}_e^B$ and $\boldsymbol{p}_t^B$ are obtained during initial registration. Thus, the third column of $\boldsymbol{R}_T^B$ is solved as:

$$\begin{bmatrix} R_{13} & R_{23} & R_{33} \end{bmatrix}^T = \hat{\boldsymbol{v}}_{te}^B \tag{6.7}$$

where $\hat{\boldsymbol{v}}_{te}^B = \frac{\boldsymbol{p}_e^B - \boldsymbol{p}_t^B}{\|\boldsymbol{p}_e^B - \boldsymbol{p}_t^B\|}$. Therefore, the rotation angles α and β, and the tilt angle between the NICHE robot and the z_b-axis, ψ, are solved as:

$$\begin{aligned} \alpha &= atan2(-R_{23}, R_{33}) \\ \beta &= atan2(R_{13}, \sqrt{R_{23}^2 + R_{33}^2}) \\ \psi &= \arccos(\cos\alpha\cos\beta) \end{aligned} \tag{6.8}$$

The above results show that the rotation angle, γ, is a redundant DoF, since the NICHE robot is symmetric along its length. To compute $\boldsymbol{P}_T^B$, Equation (6.7) is substituted into Equation (6.4), which yields:

$$\boldsymbol{P}_T^B = \boldsymbol{p}_e^B + \|\boldsymbol{p}_e^T\|\hat{\boldsymbol{v}}_{te}^B \tag{6.9}$$

The above expression indicates that $\boldsymbol{P}_T^B$ is a vector from the entry point along $\hat{\boldsymbol{v}}_{te}^B$. $\|\boldsymbol{p}_e^T\|$ is a scaling factor for the length of $\boldsymbol{P}_T^B$ and it is represented by s_e in the following sections. Therefore, the 2-DoF redundancy of the headframe system can be represented by the parameter set $\{s_e, \gamma\}$.

6.2.3 Configuration Optimization

The kinematic redundancy can be used to optimize the headframe configuration. Due to the positioning error of the linear actuators, the objective is to minimize the influence of the error in the joint space on the positioning accuracy in the task space. The optimization is subject to several geometric constraints. Since the length of each linear actuator, q_i, varies between q_{min} and q_{max}, the first set of constraints is given by: $q_{min} \leq q_i \leq q_{max}$. Due to the finite length of the linear rack, the second constraint is given by: $L_{in} + r_h \leq l_{max}$, where $L_{in} = \|\boldsymbol{P}_T^B - \boldsymbol{p}_t^B\|$. L_{in} is the insertion distance, l_{max} denotes the length from the tip of the NICHE robot to the upper end of the rack, and r_h ensures that the articulated tip can cover the most area of the hemorrhage. The joint space can be related to the task space by differentiating Equation (6.3) with respect to time, which yields:

$$\boldsymbol{J}_q\dot{\boldsymbol{q}} - \boldsymbol{J}_x\dot{\boldsymbol{x}} = 0 \Leftrightarrow \dot{\boldsymbol{x}} = \boldsymbol{J}_x^{-1}\boldsymbol{J}_q\dot{\boldsymbol{q}} \tag{6.10}$$

where $\boldsymbol{J}_q = \frac{\partial \boldsymbol{f}}{\partial \boldsymbol{q}}$ and $\boldsymbol{J}_x = \frac{\partial \boldsymbol{f}}{\partial \boldsymbol{x}}$. Thus, the positioning error in the joint space, $\boldsymbol{\epsilon}_q$, can be mapped to the positioning error in the task space, $\boldsymbol{\epsilon}_x$, by:

$$\boldsymbol{\epsilon}_x = \boldsymbol{J}_x^{-1}\boldsymbol{J}_q\boldsymbol{\epsilon}_q \tag{6.11}$$

where $\boldsymbol{\epsilon}_q = [e_{q1}\ e_{q2}\ e_{q3}\ e_{q4}\ e_{q5}\ e_{q6}]^T$ and $\boldsymbol{\epsilon}_x = [e_x\ e_y\ e_z\ e_\alpha\ e_\beta\ e_\gamma]^T$. A popular performance index for redundant system optimization is the system manipulability, which was proposed to measure the motion capability from a specific configuration [119, 120]. Since the headframe will be fixed at the optimized configuration, it is not an appropriate index. Another popular performance index is the condition number, which implies how the error in the joint space induces the error in the task space [121]. In our application, the system redundancy should be employed to minimize the positioning error for the target point. The positioning error at the tip of the NICHE robot is given by:

$$\begin{aligned}\boldsymbol{\epsilon}_{p_t^B} &= L_{in}(\boldsymbol{R}_T^B(\alpha+e_\alpha,\beta+e_\beta,\gamma+e_\gamma) \\ &\quad - \boldsymbol{R}_T^B(\alpha,\beta,\gamma))\hat{\boldsymbol{e}}_z + [e_x\ e_y\ e_z]^T\end{aligned} \tag{6.12}$$

It is hypothesized that the linear actuation module is capable of precisely controlling the insertion distance due to the high ratio gearhead and high-resolution encoder integrated with the DC motor. Besides, small positioning error at the top plate will be amplified significantly at the tip of the NICHE robot. Thus, it is assumed that the tip positioning error is exclusively induced by the positioning error of the Stewart platform. By assuming small positioning error, the above expression is rewritten as:

$$\boldsymbol{\epsilon}_{p_t^B} = \boldsymbol{M}\boldsymbol{\epsilon}_x \tag{6.13}$$

where $\boldsymbol{M} = \left[\boldsymbol{I}_{3\times3}|L_{in}\boldsymbol{J}_m\right]$ and $\boldsymbol{J}_m = \frac{\partial[R_{13}\ R_{23}\ R_{33}]^T}{\partial[\alpha\ \beta\ \gamma]^T}$. Therefore, the Euclidean distance error for the target point is given by:

$$\epsilon = \boldsymbol{\epsilon}_q^T\boldsymbol{Q}\boldsymbol{\epsilon}_q \tag{6.14}$$

where $\boldsymbol{Q} = \boldsymbol{J}_q^T\boldsymbol{J}_x^{-T}\boldsymbol{M}^T\boldsymbol{M}\boldsymbol{J}_x^{-1}\boldsymbol{J}_q$. If all the linear actuators produce the same error, e_q, the positioning error in the joint space is given by: $\boldsymbol{\epsilon}_q = e_q\boldsymbol{I}_{6\times1}$. Therefore, to reduce the positioning error, the optimization objective is to minimize the cost function, C_{error}, as follows:

$$\bar{\boldsymbol{x}} = \arg\min_{\boldsymbol{x}}(C_{error}) \tag{6.15}$$

where $C_{error} = \boldsymbol{I}_{1\times6}\boldsymbol{Q}\boldsymbol{I}_{6\times1}$. The above optimization is subject to the aforementioned geometric constraints. A brute-force algorithm is used to search the best parameter set in a discrete space with a step size of 0.25 mm and 0.25 ° for s_e and γ, respectively. It costs up to over 20 minutes to search the optimal configuration for some pairs of target point and entry point on a desktop computer (Intel® Core™ i7-6700 CPU @ 3.4 GHz).

6.2.4 Workspace Simulation

After the headframe is mounted on the patient's skull, the headframe manipulates the NICHE robot to align it with the entry point and the target point. Therefore, the capability of the headframe in orienting the NICHE robot with its tip pointing to the entry point is important. The workspace of the headframe is defined as the collection of all possible poses of the NICHE robot when its tip points to the entry point. Because the pedestal is rigidly fixed on the skull, the distance from the entry point to the origin of $\{B\}$ along the z_b-axis is assumed to be constant. Since it is challenging to analytically compute the forward kinematics of a Stewart platform, which can include up to 40 real postures [122], the workspace of the headframe is simulated using brute-force search with the geometric constraints. If the entry point is perfectly aligned with the center of the pedestal in the $x_b - y_b$ plane, the workspace of the headframe is shown in Figures 6.5(a) and (b). Only the peripheral achievable poses are displayed. The simulation results show that the system has a cone-

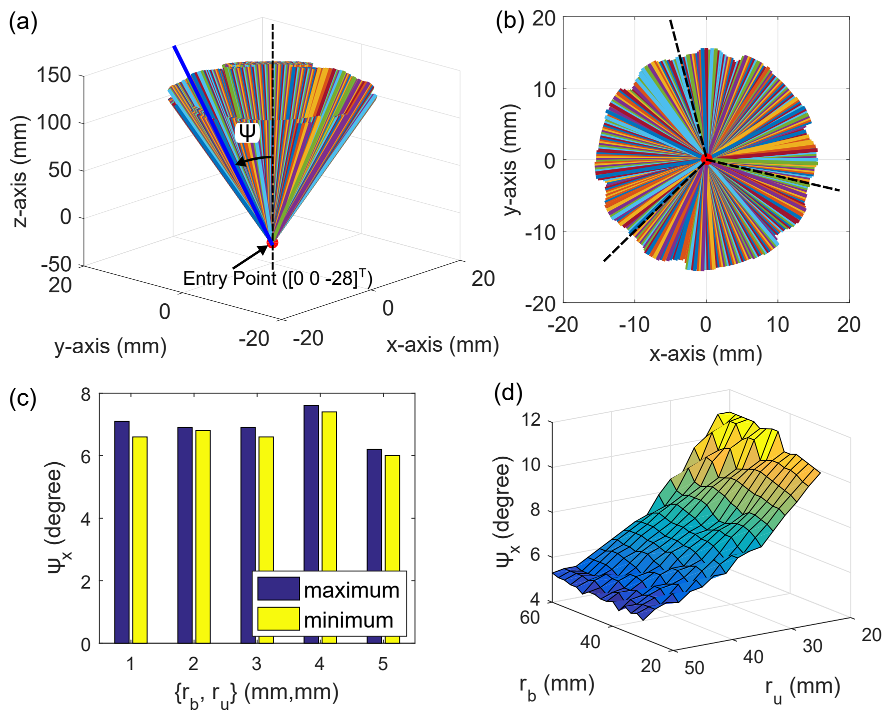

Figure 6.5: Workspace of the headframe when the entry point is fixed at $[0, 0, -28]^T$: (a) 3D view and (b) top view. (c) Maximum tilt angle in the x_b-axis when the lower bound varies between [110 mm, 150 mm] for different $\{r_b, r_j\}$. (1:{45,40},2:{45,30},3:{45,35},4:{40,35},5:{50,35}). (d) Maximum tilt angle along the x_b-axis versus r_b and r_u.

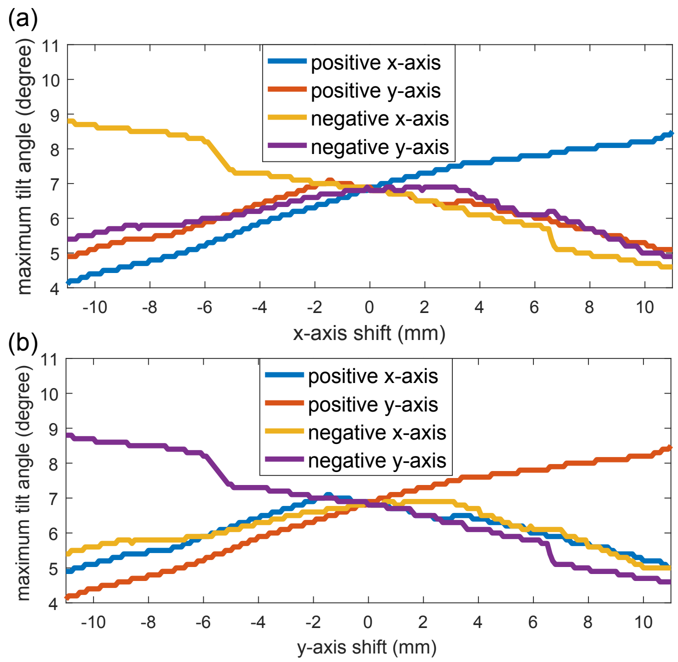

Figure 6.6: Maximum tilt angle in the positive and negative directions along x_b- and y_b-axis versus the entry point position: (a) entry point shifts along the x_b-axis and (b) entry point shifts along the y_b-axis.

shaped workspace which is symmetric about three axes. Along the positive x_b- and y_b-axis, the maximum tilt angles are the same as 6.9°. Along the negative x_b- and y_b-axis, the maximum tilt angles are the same as 6.8°.

It is critical to design the geometry of the Stewart platform to obtain a large workspace without significantly increasing the system volume. Three primary geometric variable are investigated, including the radius of the top plate, r_u, the radius of the bottom plate , r_b, and the range of leg length. Since the linear actuator has a 10 mm stroke, the range of leg length is determined by its lower bound, l_{lb}. l_{lb} can be adjusted by using adaptive components that connect linear actuators to universal and ball joints. The minimum value of l_{lb} is 110 mm. In the first simulation, it is observed that there is no significant change in workspace by increasing l_{lb}. Figure 6.5(c) shows the change in the maximum and minimum of the maximum tilt angle along x_b when l_{lb} changes between 110 mm and 150 mm for different combinations of $\{r_b, r_j\}$. Therefore, the minimum length of 110 mm is selected for a compact design. In the second simulation, it is observed that workspace is much more affected by r_u than r_b. Figure 6.5(d) shows that the maximum tilt angle along the x_b-axis significantly increases when r_u increases and is barely affected by the change of r_b. Therefore, a small bottom plate should be used to enable a small footprint of the headframe.

However, the center of the headframe pedestal and the entry point may be slightly misaligned since the installation is manually performed. It is critical to check the workspace of the headframe given slightly misaligned entry points. Based on the diameters of the pedestal hole and the NICHE robot, all possible positions of the entry point are constrained within a 11 mm diameter circular region in the $x_b - y_b$ plane. Figures 6.6(a) and (b) show the changes of the maximum tilt angles in the positive and negative directions along the x_b- and y_b-axis when the entry point shifts along the x_b- and y_b-axis, respectively.

6.3 Experiment and Demonstration

6.3.1 2D Positioning Accuracy

The first experimental study evaluates the positioning accuracy of the headframe for the entry point. In this study, as shown in Figure 6.7(a), the headframe is fixed on the top of a setup made of acrylic plates. A piece of grid paper (interval distance: 1 mm) is placed on the top of a 3 mm thick flexible plate made by a Form 2 3D printer (Formlabs Inc., Somerville, MA, USA) and fixed between the headframe pedestal and the top acrylic plate. Meanwhile, a stiff and slender rod with a conical tip is installed on the linear actuation module, so that it can be actuated to indent the grip and the indentation will show the actual entry point. As shown in Table 6.1, several different locations

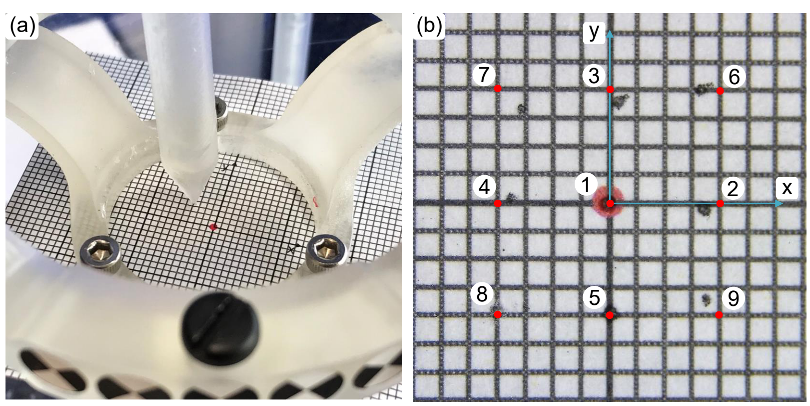

Figure 6.7: Experimental evaluation of 2D positioning accuracy: (a) a slender rod with a conical tip manipulated by the headframe and (b) indentation on the grip paper with red dots showing the planned entry points.

Table 6.1: Positioning error for entry points

	Planned Entry Point	Planned Target Point	Actual Indentation	Positioning Error	Euclidean Distance Error
Symbol	$(\mathbf{P}_e^B)^T$	$(\mathbf{P}_t^B)^T$	$(\mathbf{P}_i^B)^T$	$(\mathbf{d}_e^B)^T$	$\|\mathbf{d}_e^B\|$
Unit	[mm mm mm]	[mm mm mm]	[mm mm mm]	[mm mm mm]	mm
1	[0 0 -25]	[0 0 -100]	[-0.074 -0.056 -25]	[0.074 0.056 0]	0.093
2	[4 0 -25]	[0 0 -100]	[3.492 -0.186 -25]	[0.508 0.186 0]	0.541
3	[0 4 -25]	[0 0 -100]	[0.316 3.714 -25]	[-0.316 0.286 0]	0.426
4	[-4 0 -25]	[0 0 -100]	[-3.659 0.167 -25]	[-0.341 -0.167 0]	0.380
5	[0 -4 -25]	[0 0 -100]	[0.037 -4.049 -25]	[-0.037 0.049 0]	0.061
6	[4 4 -25]	[0 0 -100]	[3.343 4.079 -25]	[0.657 -0.079 0]	0.662
7	[-4 4 -25]	[0 0 -100]	[-3.250 3.454 -25]	[-0.750 0.546 0]	0.928
8	[-4 -4 -25]	[0 0 -100]	[-4.060 -4.030 -25]	[0.060 0.030 0]	0.067
9	[4 -4 -25]	[0 0 -100]	[3.529 -3.491 -25]	[0.471 -0.509 0]	0.694

are planned as the entry point and [0 0 -100]^T is designated as the target point. After performing motion planning and computing inverse kinematics with configuration optimization, the headframe is actuated to indent the grip paper with the tip of the slender rod. For each planned entry point, indenting trials were repeated three times.

It is observed that the indents of three trials for each planned entry point merge together, so that the geometric center of an indent is taken as the actual entry point. Figure 6.7(b) shows all the actual indentations (black dots) and planned entry points (red dots). A stereo microscope (Model S6D, Leica, Wetzlar, Germany) was used to measure distance. For each planned entry point, the rod is inserted 0.5 mm more than the planned distance to ensure the contact between the grip paper and the rod tip. Table 6.1 also summarizes the error for all the tests, where $\mathbf{P}_e^B$, $\mathbf{P}_t^B$, and $\mathbf{P}_i^B$ are the position of the planned entry point, planned target point, and actual indentation, respectively. $\mathbf{d}_e^B$is the positioning error for the entry point and $\mathbf{d}_e^B = \mathbf{P}_e^B - \mathbf{P}_i^B$. The average positioning error is about 0.428 mm for all the planed targets points and the maximum positioning error is 0.928 mm for the planned entry point at [-4 4 -28]. The positioning error is primarily caused by the error of the linear actuators, structural error of the headframe, and the misalignment of the grip paper. Since the burr hole made by the surgeon is usually slightly larger than the surgical robot, this amount of positioning error in targeting the entry point should be acceptable. The reference paper was carefully placed to align its x- and y-axis with x_b- and y_b-axis, respectively. The positioning error is primarily caused by the positioning error of the linear actuators, the tolerance between the linear bearing and the rack, and the slack in the ball joints.

6.3.2 3D Positioning Accuracy

The second experimental study evaluates the positioning accuracy of the headframe for the target point in the 3D space. In this study, as shown in Figure 6.8(a), a modified slender rod with a vision marker on its tip is installed on the headframe. By detecting the position of the vision markers around the circumference of the base plate of the headframe in the coordinate frame of the camera, $\{F_C\}$, the position and orientation of $\{F_B\}$ can be registered in $\{F_C\}$, which are denoted by $\mathbf{P}_C^B$ and $\mathbf{R}_C^B$, respectively. The detailed registration process is given in Appendix A. Afterwards, several different locations are planned as the target point, $(\mathbf{P}_t^B)^T$, as shown in Table 6.2. After designating $[0\ 0\ \text{-}28]^T$ as the entry point, motion planning is performed and inverse kinematics is solved with optimized configuration. The rod with the vision marker is then actuated to reach the planned target point and the actual position of the vision marker with respect to $\{F_C\}$ is acquired by the stereoscopic camera and denoted as $\mathbf{P}_m^C$. Figure 6.8(b) shows a camera image showing the headframe with all the detected vision markers. Therefore, the position of the vision marker with respect to $\{F_B\}$ can be computed as:

$$\mathbf{p}_m^B = \mathbf{P}_C^B + \mathbf{R}_C^B \mathbf{P}_m^C \tag{6.16}$$

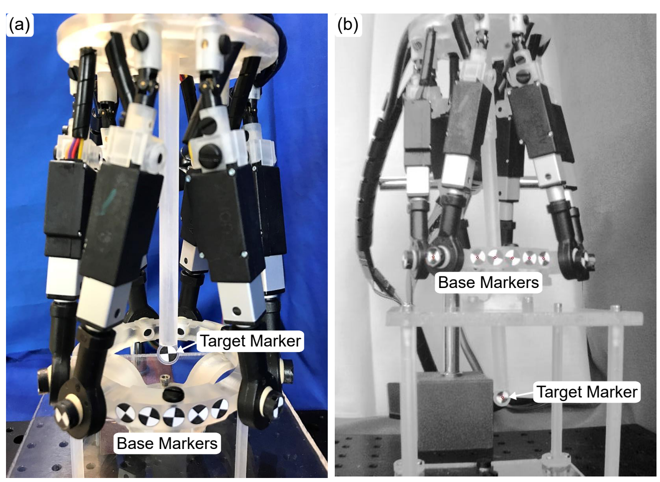

Figure 6.8: Experimental setup for evaluating 3D positioning accuracy: (a) headframe manipulating a slender rod with a vision marker on the tip and (b) all vision markers detected by the stereoscopic camera.

Table 6.2: Positioning error for target points

	Planned Entry Point	Planned Target Point	Actual Vision Marker	Positioning Error	Euclidean Distance Error
Symbol	$(\mathbf{P}_e^B)^T$	$(\mathbf{P}_t^B)^T$	$(\mathbf{P}_m^B)^T$	$\mathbf{d}_t^T$	$\|\mathbf{d}_t\|$
Unit	[mm mm mm]	[mm mm mm]	[mm mm mm]	[mm mm mm]	mm
1	[0 0 -28]	[0 0 -70]	[0.562 0.662 -69.850]	[-0.562 -0.662 -0.150]	0.881
2	[0 0 -28]	[0 0 -80]	[0.639 0.756 -80.295]	[-0.639 -0.756 0.295]	1.033
3	[0 0 -28]	[0 0 -90]	[0.816 0.770 -90.470]	[-0.816 -0.770 0.470]	1.208
4	[0 0 -28]	[5 0 -80]	[5.739 0.357 -79.892]	[-0.739 -0.357 -0.108]	0.828
5	[0 0 -28]	[0 5 -80]	[0.766 4.812 -80.247]	[-0.766 0.188 0.247]	0.827
6	[0 0 -28]	[-5 0 -80]	[-5.260 0.164 -80.601]	[0.260 -0.164 0.601]	0.675
7	[0 0 -28]	[0 -5 -80]	[0.660 -4.784 -80.600]	[-0.660 -0.216 0.600]	0.918

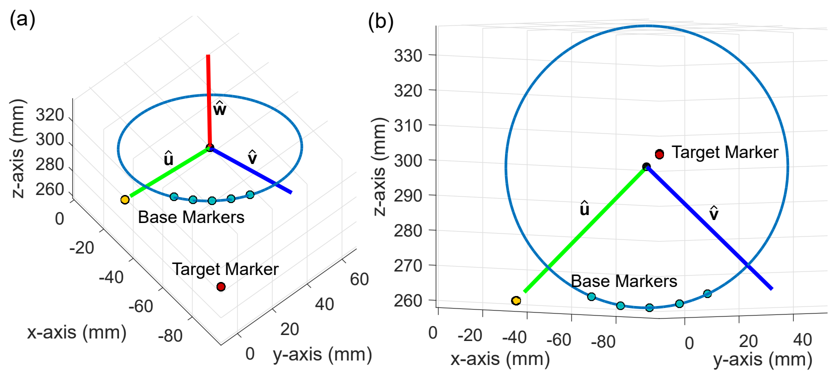

Figure 6.9: Registration of the base plate of the headframe and tip of the rod by detecting all the vision markers using the stereoscopic camera: (a) isometric view and (b) top view.

since $\mathbf{P}_C^B = -\mathbf{R}_C^B\mathbf{P}_B^C$ and $\mathbf{R}_C^B = (\mathbf{R}_B^C)^T$, we have:

$$\mathbf{P}_m^B = (\mathbf{R}_B^C)^T(\mathbf{P}_m^C - \mathbf{P}_B^C) \tag{6.17}$$

Therefore, the positioning error for the target point is given by: $\mathbf{d}_t^B = \mathbf{P}_t^B - \mathbf{P}_m^B$. Table 6.2 also summarizes the error for all the tests, where $\mathbf{d}_m^B$ is the positioning error for the target point and $\mathbf{d}_m^B = \mathbf{P}_t^B - \mathbf{P}_m^B$. The average positioning error is about 0.428 mm for all the planed targets points and the maximum positioning error is 0.928 mm for the planned entry point at [-4 4 -28]. The positioning error is probably caused by the error of the linear actuators, structural error of the head-frame, and tracking error of the stereoscopic camera. Therefore, the achieved positioning accuracy is comparable with other related works [116, 118]. Figures 6.9(a) and (b) shows the position of all vision markers detected by the stereo camera in the 3D space.

6.3.3 System Demonstration

After integrating a NICHE robot prototype with the robotic headframe, a proof-of-concept demonstration was carried out to evaluate the capability of the developed headframe. To perform an *ex vivo* study, gelatin tissue is made from 2% by weight Knox gelatin (Kraft Foods Global, Inc., USA) inside a glass container to simulate the brain phantom. Meanwhile, a plastic pedestal is placed in the glass container and a red oval core made from 3% by weight Knox gelatin tinted by red ink is secured on the pedestal to simulate the hemorrhage. To install the headframe interfaced with the NICHE robot, a acrylic cover with a 12 mm diameter thorough hole and three taped screw holes is fixed on the top of the glass container. After aligning the headframe pedestal with the screw holes, the whole setup can be securely installed on the top of the glass container using screws, as shown in Figure 6.10(a).

Due to the manual alignment between the headframe pedestal and the burr hole in practice, there is usually a slight misalignment, so the position of the entry point is set as $[1\ 1\ \text{-}28]^T$ to

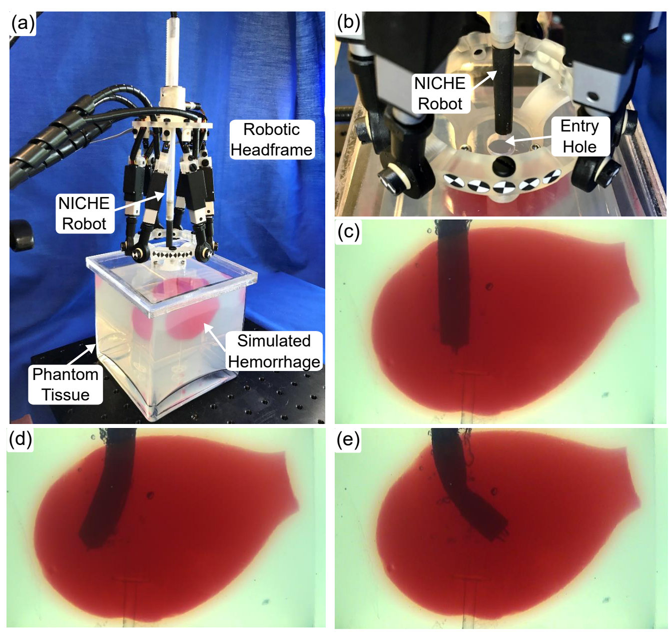

Figure 6.10: Proof-of-concept demonstration: (a) robotic headframe interfaced with the NICHE robot mounted on a container filled with gelatin phantom, (b) NICHE robot steered by the robotic headframe towards the entry hole, (c) NICHE robot inserted into the simulated hemorrhage (red gelatin core), (d) distal bending tip of the NICHE robot actuated and deflected, and (e) torsion module of the NICHE robot actuated and the end effector articulating within the gelatin phantom.

mimic the real scenario. The target point is designated inside the red gelatin core and it is decided as [0 0 -80]^T by manual measurement. Based on the position of the planned entry point and target point, the program for motion planning and inverse kinematics computation is executed. The robotic headframe is then actuated to steer the NICHE robot and align it with the target point and the entry point in the entry hole, as shown in Figure 6.10(b). The NICHE robot is then inserted into the gelatin core by the linear actuation module on the headframe, as shown in Figure 6.10(c). The whole insertion process was stable and smooth, and the robot tip reached the center of the gelatin core within five seconds. After the robot tip reaches the planned target point, the distal bending tip of the NICHE robot is actuated and bent within the gelatin core by applying constant heating current of 1A, as shown in Figure 6.10(d). The torsion joint of the NICHE robot is then actuated by applying constant heating current of 0.5A to articulate the robot tip, as shown in Figure 6.10(e).

6.4 Discussion and Conclusions

In this chapter, a lightweight and compact skull-mounted robot headframe is proposed to manipulate the NICHE robot. The headframe interfaced with the NICHE robot has a total weight of about 320 g, thus it can be mounted on the human skull with the minimum discomfort of patients. Due to the redundancy given by the symmetric surgical robot and the linear actuation module, the positioning accuracy can potentially be enhanced by minimizing the influence of the error in the joint space on the task space. Therefore, a brute-force algorithm is employed to search the optimal robot configuration that can minimize the positioning error. The 2D positioning accuracy for different entry points and 3D positioning accuracy for different target points are experimentally evaluated. The robotic headframe is capable of achieving sub-millimeter positioning accuracy. Finally, the capability of the headframe interfaced with the NICHE robot is demonstrated using a phantom model made of gelatin, showing the feasibility of the developed headframe in robot-assisted neurosurgery.

CHAPTER 7

IMAGE-GUIDED STUDIES

When meso-scale surgical robots are used in clinical trials, intra-operative imaging guidance will be necessary to provide target visualization and confirm the position of the robot with respect to the target. CT and MRI are two popular imaging modalities due to their capability of high-contrast 3D imaging for soft-tissue structures. This chapter will present the evaluating experiments of the NICHE robot and AFib robotic catheter under intra-operative CT and/or MR imaging guidance using *ex vivo* or *in vitro* models.

The rest of this chapter is organized as follows. Section 7.1 presents the experimental studies of the robot catheter under MR imaging guidance. Section 7.2 presents the manipulation of the NICHE robot under CT imaging guidance. Section 7.3 presents the evaluating experiments of the NICHE robot under MR imaging guidance. Section 7.4 concludes the chapter.

7.1 *In Vitro* Robot Evaluation

7.1.1 MR Imaging-Guided Tests

The MRI-compatibility of the SMA bending module and the steerable catheter tip is evaluated using the experimental setup shown in Figure 7.1(a). The braid-reinforced tube is removed due to its stainless steel braids. The steerable tip is fixed on a 3D-printed plastic tube and the distal two bending modules are immersed in water inside a container. The experimental setup was placed inside a 60 mm diameter quadrature detection coil (Doty Scientific Inc., Columbia, SC, USA) within a 7 Tesla MRI scanner (PharmaScan®, Bruker, Billerica, MA) to acquire MR images. The repetition time (TR) and echo time (TE) are 50 ms and 2.6 ms, respectively. In the first case, the second distal bending module of the steerable tip was actuated directly by Joule heating actuation. Figures 7.2(a) and (b) show the MR images acquired before actuation and after 2 A current was applied for 10 s. A bright area is observed near the steerable tip in the MR image, due to the intensified magnetic field caused by the large electric current through the leading wiring and SMA wire. The bending

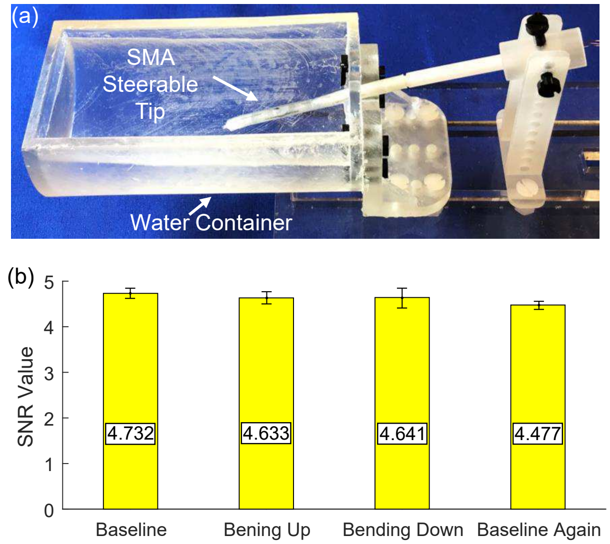

Figure 7.1: MRI-compatibility evaluation: (a) experimental setup with the SMA-actuated catheter tip inside a water container and (b) SNR values of MR images acquired before actuation (baseline), when the tip moves upward and downward, and after actuation (baseline again).

angle is relatively small due to the fast heat dissipation in water. In the second case, the second distal bending module is actuated by conductive heating actuation. Figures 7.2(c) to (f) show that there are no observable change of the MR imaging quality when the steerable tip is actuated by

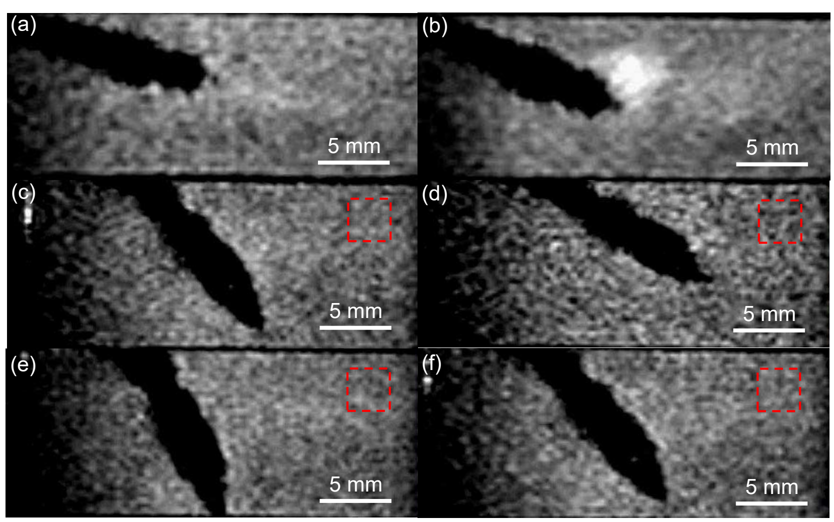

Figure 7.2: Manipulation of the SMA-actuated catheter tip under MR imaging guidance: (a) before Joule heating actuation, (b) during Joule heating actuation, (c) before conductive heating actuation before actuation, (d) tip moving upward under conductive heating actuation, (d) tip moving downward under conductive heating actuation, and (f) after conductive heating actuation.

100 mA electric current. Figure 7.1(b) concludes the signal-to-noise ratio (SNR) values of MR images acquired before, during, and after actuation for three individual tests. It is observed that the SNR values are almost constant in the whole procedure. The difference between these two cases proves that large electric current causes strong electromagnetic field and the developed steerable tip is MRI-compatible due to its small electric current requirement. To calculate SNR values, two consecutive images with a 5 s interval are acquired when the catheter maintains a stable pose. After selecting a fixed region of interest (ROI), as shown in Figures 7.2(c) to (f), the mean pixel intensity within the ROI in the first image is defined as the image signal. A third image is obtained by subtracting the second one from the first one and the image noise is defined as the standard deviation of the pixel intensity within the same ROI in the third image divided by $\sqrt{2}$ [123]. To develop a fully MRI-compatible catheter, the braid-reinforced tube can potentially be customized by using Nitinol as the filament material.

7.1.2 CT Imaging-Guided Manipulation

The NICHE robot with the second-generation torsion module is fixed on the tip of an aluminum rod and manually inserted into a cantaloupe (at its core) to evaluate its working performance in the humid environment, as shown in Figure 7.3(a). Figure 7.3(b) shows the shaded surface display of the robot prototype using a C-Arm CT scanner (Siemens, Munich, Germany). It demonstrates the ease of identifying the robot along with its individual components, such as the torsion module

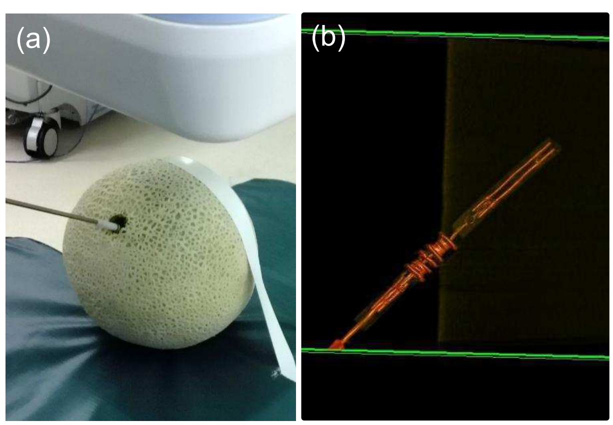

Figure 7.3: Experimental setup for CT imaging-guided tests on phantom models: (a) NICHE robot within the cantaloupe and (b) shaded surface display of the NICHE robot in a gelatin slab.

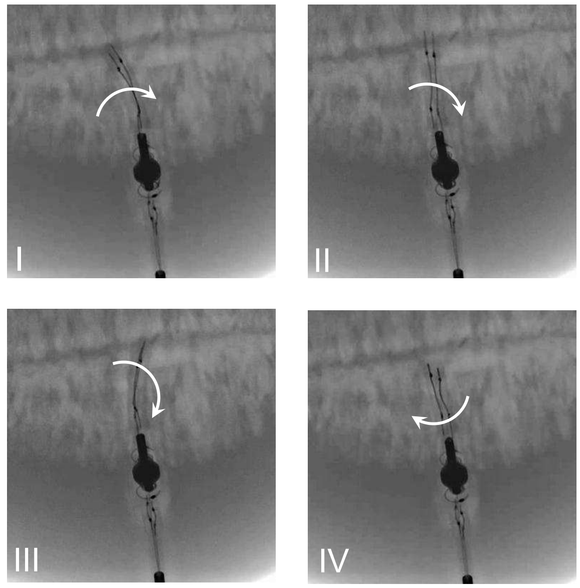

Figure 7.4: CT imaging of the tip articulation of the NICHE robot within the cantaloupe by actuating the SMA torsion module.

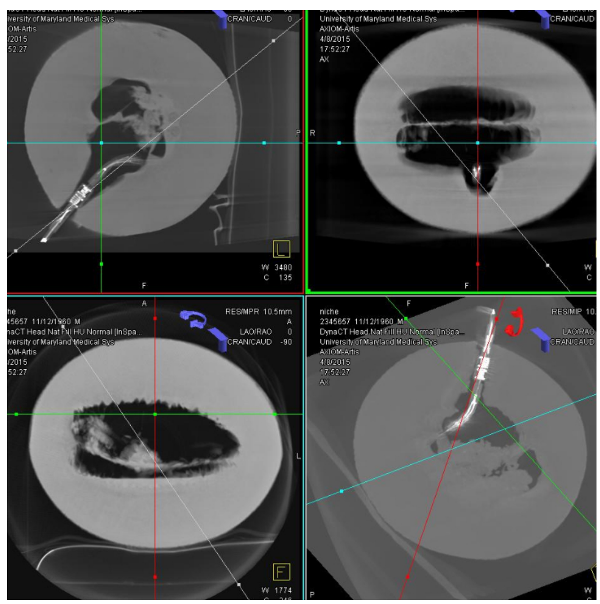

Figure 7.5: Screenshots of the multi-planar display capabilities of cone-beam CT and I-Guide reconstructions during the NICHE robot manipulation within the cantaloupe.

and the distal bending tip, by using cone-beam CT image reconstructions. Under C-Arm CT image guidance, a constant current of 1.9 A is provided to actuate the SMA torsion module. Figure 7.4 shows the rotary motion of the torsion module for about 300° (by visual estimation) in 30 s with the deflected bending tip. Since the structural components of the robot are plastic, they are transparent in CT images. The motion range is smaller than the motion range in air as presented in Section 2.2.3, probably due to the resistant force applied by the soft tissue in the cantaloupe on the torsion module when the tissue is pressed by the moving bending tip. This factor not only reduces the motion range, but also increase the temperature requirement for completing the forward SMA phase transformation. The highest heating temperature is limited by the maximum heating current and the heat resistance of the robot components and electric wiring. Figure 7.5 shows the multi-planar display capabilities of cone-beam CT and I-Guide reconstructions during the robot manipulation within the cantaloupe. This allows the operator to assess the individual components of the robot in relationship to adjacent soft-tissue structures in a variety of user defined planes.

7.2 *Ex Vivo* Robot Evaluation

7.2.1 Human Cadaver Head Preparation

The preparation of a human cadaver head for *ex vivo* robot evaluation is shown in Figure 7.6. As shown in Figure 7.6(a), the scalp around the designated entry point for the NICHE robot was removed in a preparation room. In the second step, a burr hole was drilled on the skull at the designated entry point, as shown in Figure 7.6(b). Subsequently, three screw holes were drilled using a

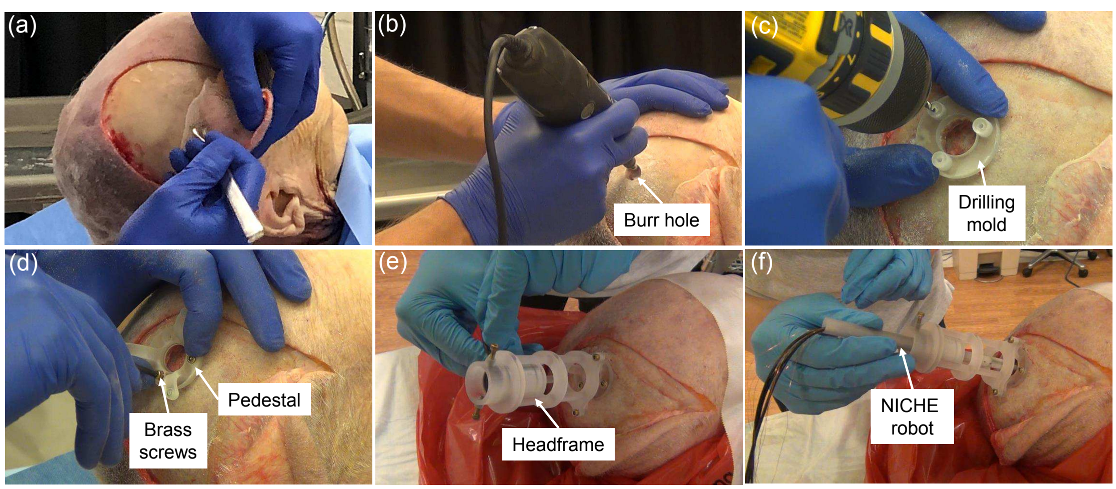

Figure 7.6: Preparation of the *ex vivo* studies on a human cadaver head: (a) removing scalp, (b) drilling a burr hole on the skull, (c) drilling screw holes using a mold, (d) mounting the pedestal onto the skull, (e) installing the headframe onto the pedestal, and (f) inserting the NICHE robot and fixing its position using brass screws.

mold and a pedestal was fixed on the skull using brass screws, as shown in Figures 7.6(c) and (d). After removing the dura inside the burr hole, the temperature of the brain tissue was measured to be about 25°C using an infrared thermometer. Afterwards, the cadaver head was transported onto a patient table in a surgical suite equipped with a C-arm CT scanner (Siemens, Munich, Germany). A nonrobotic headframe was then mounted onto the pedestal using brass screws, as shown in Figure 7.6(e). The pedestal and the headframe were 3D-printed in plastic material. After the NICHE robot was inserted through the linear bearing on the top of the headframe, the NICHE robot was locked using two brass screws, as shown in Figure 7.6(f).

7.2.2 CT Imaging-Guided Manipulation

CT is usually used to provide image guidance during intracranial neurosurgery, due to its good imaging contrast and allowance of surgeons' intra-operational intervention. Therefore, the NICHE robot equipped by the second-generation fiberoptic rotation sensor was evaluated under CT imaging guidance using the human cadaver head, as shown in Figure 7.7. The technique of conductive heating actuation was applied on the bending tip of the NICHE robot.

As shown in Figure 7.8(a), the cone-beam CT image shows the artifacts created by the NICHE robot in the initial straight configuration. The artifacts created by the SMA wires of the bending tip are clean, while the artifacts created by the brass screws and stainless steel linear bearing are messy, but they do not affect the ROI around the robot tip. In the first step, the bending tip was actuated by applying a 50 mA electric current. As shown in Figures 7.8(b) and (c), the bending tip performs a sharp deflection and the maximum bending angle is about 180° after 10 s. The SMA

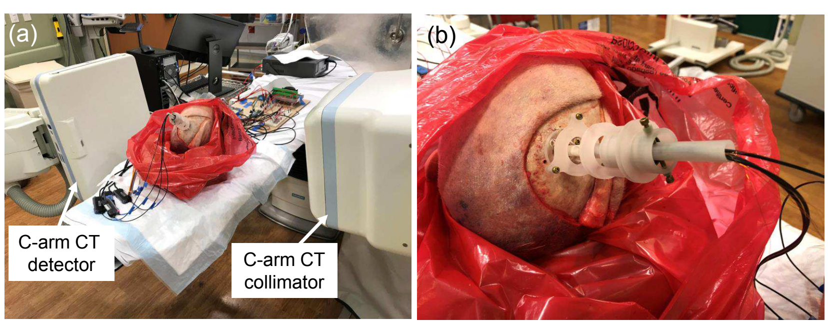

Figure 7.7: Experimental setup for CT imaging-guided tests on a human cadaver head: (a) overall view and (b) close-up view.

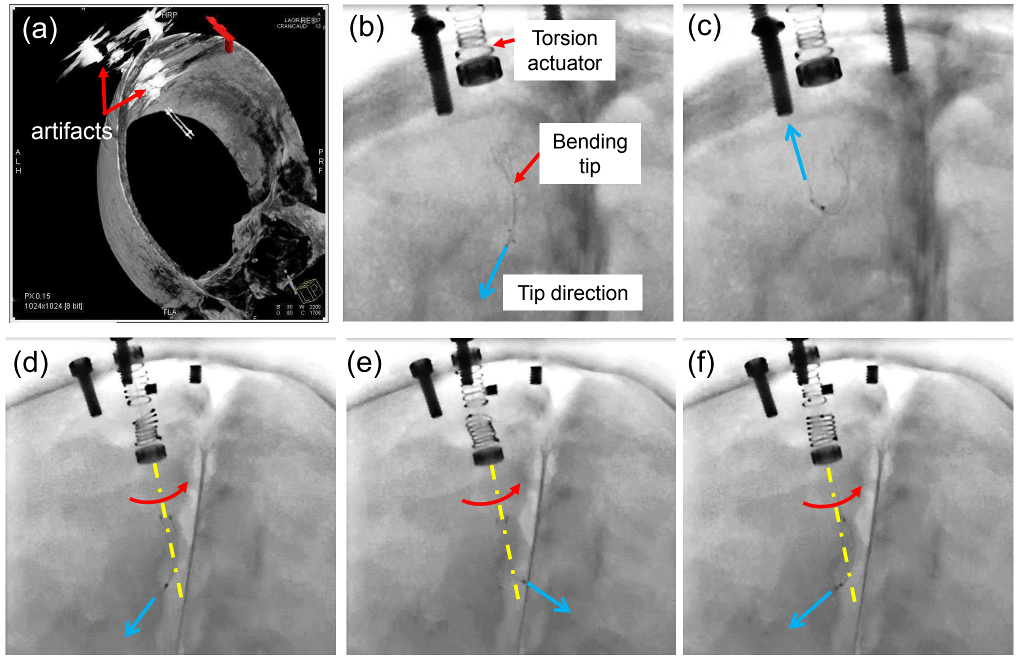

Figure 7.8: CT imaging-guided manipulation of the NICHE robot in the human cadaver brain: (a) cone-beam CT imaging showing artifacts, (b) beginning of tip deflection, (c) end of tip deflection, (d) beginning of tip articulation, (e) during tip articulation, and (f) end of tip articulation.

wires in the bending tip could be easily identified. Compared to the experimental results when Joule heating actuation was applied, as shown in Figure 7.4, conductive heating actuation enables a larger deflection of the bending tip. This is probably because when the robot is surrounded by the wet tissue, the heat of SMA is dissipated quickly via the thermal conduction with the tissue when the SMA is heated. When conductive heating actuation is used, the SMA wire can be heated efficiently even in the wet environment by increasing electric current and heating intensity, resulting in a larger deflection. However, when Joule heating actuation is used, it is challenging to increase the electric current, which is already required to be high to actuate the bending tip in air, due to the safety concern, power limitation, and overheat of electric wiring. Next, the torsion module is controlled using a PI controller to rotate by 360° with the motion feedback provided by the fiberoptic rotation sensor. Figures 7.8(e) to (f) show the CT images of the robot when the robot rotates to the target position. From the CT images, it is observed that the tip articulation is relatively precise and the actuation response was fast.

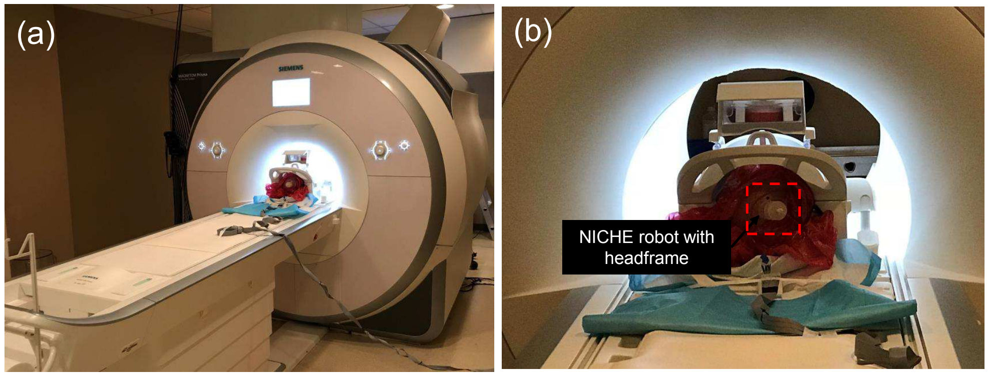

Figure 7.9: Experimental setup for MR imaging-guided tests on a human cadaver head: (a) overall view and (b) close-up view.

7.2.3 MR Imaging-Guided Manipulation

Due to the concern of radiation exposure to patients and surgeons when CT is used, MRI is an alternative solution to provide image guidance with good contrast and zero radiation. Therefore, the MRI-compatibility of the NICHE robot integrated with the SMA bending tip and SMA torsion module was evaluated. Due to the limited length of the off-the-shelf optical fibers, the fiberoptic rotation sensor was not used and the NICHE robot was controlled in the open-loop mode. To ensure the MRI-compatibility of the whole system, the headframe used for the CT tests was modified. The linear bearing for inserting the NICHE robot is a nonmagnetic PTFE-lined fiberglass bearing. The technique of conductive heating actuation was applied to the bending tip by routing nichrome coils around the SMA wires of the bending tip using the method presented in Section 3.1.2, while the torsion module was energized directly by Joule heating actuation. Ceramic bearings were used in the SMA torsion module to support the rotary shaft.

After the pedestal was mounted on the skull using brass screws, the human cadaver head was transported into the MRI suite and placed on the patient table. The headframe was then mounted onto the pedestal using plastic screws and the NICHE robot was inserted through the linear bearing and burr hole into the brain. After locking the NICHE robot using brass screws, the patient table with the cadaver head was moved into the 70 cm diameter bore of a 3-Tesla MRI scanner (Siemens, Munich, Germany). The digital control system was placed outside the MRI suite and the power cables were connected to the robot through a penetration panel. The power supply outputs a constant electric current to actuate the bending tip and torsion module.

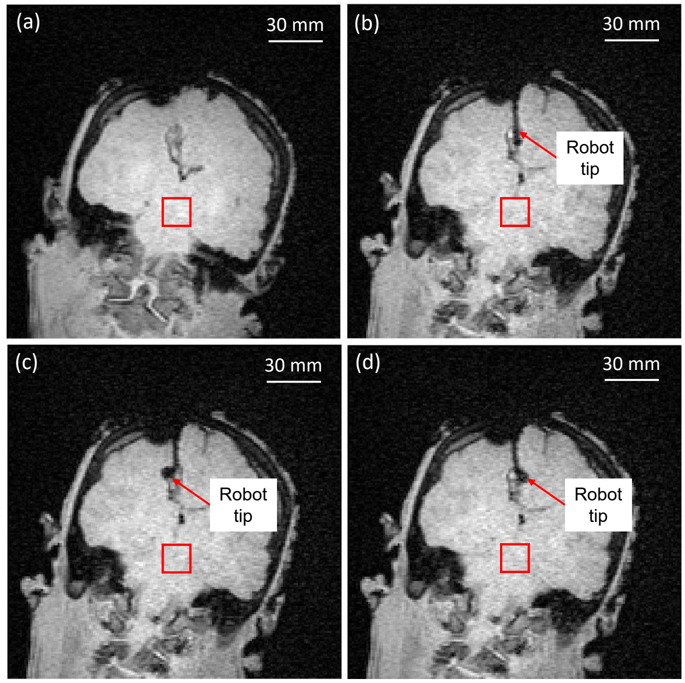

Figure 7.10: Dynamic MR imaging of the NICHE robot in the coronal plane: (a) human cadaver head without the NICHE robot, (b) NICHE robot in the brain before tip deflection, (c) bending tip of the NICHE robot deflecting towards the left, and (d) bending tip of the NICHE robot deflecting towards the right. The red rectangle shows the ROI for calculating SNR values.

To quantitatively evaluate the MRI-compatibility of the NICHE robot, dynamic MR imaging was performed. The SNR change when either the bending tip or the torsion module was actuated is calculated. The gradient echo (GRE) method was used and the scanning parameters were the same for the both cases. TR is 12 ms, TE is 1.72 ms, field-of-view (FOV) is 220 mm, flip angle is 10°, slicing thickness is 4 mm, voxel size is 1.4 mm $\times$ 1.4 mm $\times$ 4 mm, and the frame rate is 1.2 s/frame. To evaluate the bending tip, a series of dynamic MR images in the coronal plane were acquired when only the human cadaver head was in the scanner bore, as shown in Figure 7.10(a). After the NICHE robot was installed, MR images were acquired when the robot was not actuated, as shown in Figure 7.10(b). Afterwards, the bending tip was actuated by a 40 mA electric current to deflect to the left and then right, as shown in Figures 7.10(c) and (d), respectively. To evaluate the torsion module, a series of dynamic MR images in the transverse plane were acquired when only the human cadaver head was in the scanner bore, as shown in Figure 7.11(a). After the robot was installed and the bending tip was tested, a series of MR images in the transverse were acquired

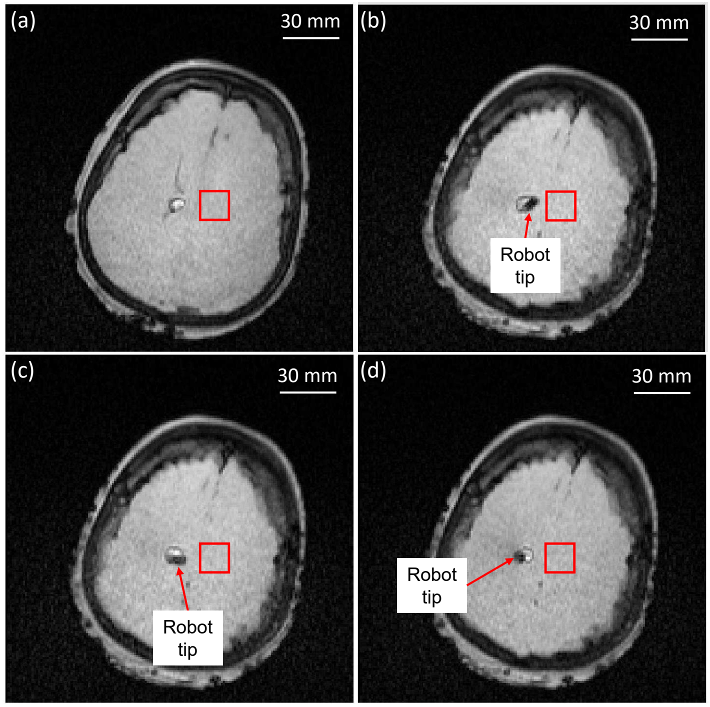

Figure 7.11: Dynamic MR imaging of the NICHE robot in the transverse plane: (a) human cadaver head without the NICHE robot, (b) NICHE robot in the brain before tip articulation, (c) robot tip articulating clockwise by actuating the SMA torsion module, and (d) robot tip at a stable position. The red rectangle shows the ROI for calculating SNR values.

when the torsion module was not actuated, as shown in Figure 7.11(b). Afterwards, when the torsion module was energized by a 2 A electric current, MR images were acquired, as shown in Figures 7.11(c) and (d). Since the bending tip was not energized, it partially recovered the straight configuration yet was still slightly deflected. Therefore, the rotating black area in Figures 7.11(b) to (d) is an oblique section of the bending tip.

To calculate SNR values, an ROI close to the robot is selected in dynamic MR images, as shown by the red squares in Figures 7.10 and 7.11. The method presented in Section 7.1.1 is used to calculate SNR values. Figure 7.12(a) shows the SNR change for the bending tip tests. The SNR value is 23.8 for only the cadaver head (baseline). The SNR value dropped about 17% to 19.7 after the NICHE robot was installed (bending unactuated). When the bending tip was actuated, the drop of the SNR value was 1.2% (bending actuated). The negligible SNR drop was due to the extremely low electric current for the conductive heating actuation. For the torsion module tests, the initial SNR value was 14.41 for MR imaging of only the cadaver head (baseline), as shown in

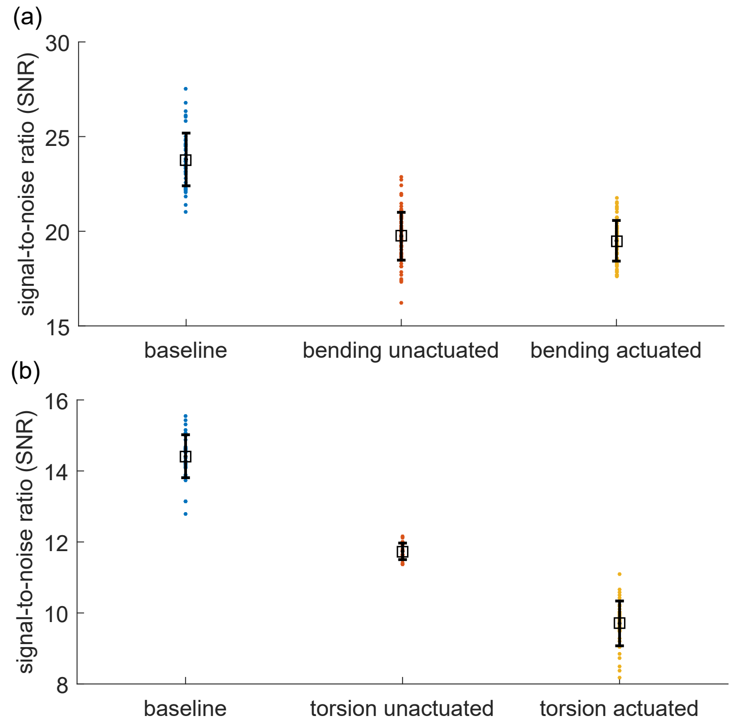

Figure 7.12: Change of SNRs value for dynamic MR imaging: (a) SMA bending tip actuated and (b) SMA torsion module actuated. The baseline denotes the SNR values when the human cadaver head was placed inside the bore of the MRI scanner without the NICHE robot.

Figure 7.12(b). The SNR value dropped by 18.5% to 11.7 for MR imaging of both the cadaver head and the unactuated robot (torsion unactuated). When the torsion module was energized, the SNR value experienced another significant drop of 17.3% and became 9.7 (torsion actuated), due to the high electric current (2 A) used for Joule heating actuation. In addition, it was observed that electric wiring sometimes snapped due to high Lorentz force when high electric current passed through it in the strong magnetic field in the bore of the MRI scanner.

7.3 Discussion and Conclusions

In this chapter, the robotic systems based on the fundamental SMA actuation modules are experimentally evaluated. In individual studies, intra-operative imaging guidance is provided by CT or MRI when the robot is manipulated. *In vitro* studies under MR imaging guidance show that the robotic catheter under conductive heating actuation is MRI-compatible. When the NICHE robot is manipulated in a cantaloupe under CT imaging guidance, the individual components of the robot against the surrounding tissue can be easily identified. The NICHE robot is further evaluated by manipulating it inside a human cadaver brain. Under CT imaging guidance, the articulation of the robot tip can be controlled in the closed-loop mode with the motion feedback provided by the fiberoptic rotation sensor. By applying the technique of conductive heating actuation on the bending tip, the bending tip can perform sharp deflection in brain tissue. Under MR imaging guidance, the NICHE robot shows good MRI-compatibility when the bending tip is actuated by conductive heating due to small electric current and electromagnetic field cancellation; Nevertheless, the MRI-compatibility and system reliability of the NICHE robot is lowered when the torsion module is actuated by Joule heating.

CHAPTER 8

CONCLUSIONS AND FUTURE WORK

8.1 Conclusions

This thesis focuses on the development of surgical robotic systems based on smart materials and structures. Nitinol SMA is explored to develop meso-scale actuation modules and optical sensors are developed to provided motion feedback. Since Nitinol is a safe material to be used in the magnetic and radioactive environment, the developed surgical robots can potentially be manipulated under intra-operative imaging guidance, which can provide surgeons with real-time visualization. In addition, intra-operative MR imaging-guided surgery, which is challenging using conventional surgical tools, can become possible. 3D-printing techniques are utilized to manufacture the robotic devices with relatively low cost, high accuracy, and fast speed, enabling disposable surgical robot prototypes. The specific contributions of the research presented in this dissertation are concluded as follows:

1) To perform torsion motion in robot-assisted surgery, a compact torsion module is developed based on the customized SMA torsion springs made of Nitinol wiring [124, 125]. Through the alternate shape recovery of SMA torsion springs under Joule heating, bi-directional torsion module can be performed. Given the nonlinear thermomechanical properties of SMA, the optimal pre-deformation of SMA torsion springs is derived to achieve the maximum motion range. The developed SMA torsion module is able to rotate by more than 360°, which is sufficient for most surgical applications requiring torsion motion.

2) Bending motion is another necessary motion type for surgical procedures. This research work pushes the SMA bending module closer to clinical applications by proposing a conductive heating actuation technique [126]. By routing a folded, enameled high-resistance nichrome wire around each SMA wire of the bending module, the bending module can be actuated efficiently by applying significantly low electric current to the nichrome wire. Since the electromagnetic fields by individual nichrome strands are canceled by each other, the MRI-compatibility of the device is

improved.

3) A compact fiberoptic rotation sensor is developed based on light intensity modulation to provide the motion feedback of the SMA torsion module and control its motion in a closed-loop mode [127–129]. A brass mirror is fabricated to modulate the light emitted and received by optical fibers when the mirror rotates with the torsion module. By using three fiber sets, the measurement range of the sensor is more than 360°. By integrating the sensor with the SMA torsion module, the rotation motion can be controlled precisely .

4) To measure the large-curvature deflection of the SMA bending module, an FBG bending sensor is developed. The sensor is fabricated by combining FBG fibers with an ultra-thin superelastic substrate using flexible adhesive with low shear modulus. Thus, the strain in the fibers can be controlled under the strain limit at large curvatures, enabling the measurement of large curvatures. However, hysteresis is observed due to the friction applied on the sensor. Due to the orthogonal arrangement of the fibers and SMA wires, the differential sensor output is insensitive to the temperature change caused by SMA actuation.

5) The developed actuation and sensing modules are applied to develop a robotic catheter for AFib treatment [126] and a neurosurgical robot, named NICHE, for ICH evacuation [130, 131], respectively. The robotic catheter consists of multiple SMA bending modules and shows MRI-compatibility. The NICHE robot is developed by integrating the SMA torsion module and SMA bending module to realize tip articulation in the blood clot. The rotation of the robot tip can be precisely controlled using the motion feedback provided by the fiberoptic rotation sensor. A skull-mounted robotic headframe is developed to manipulate the NICHE robot for ICH evacuation [132]. The developed robotic systems are evaluated using phantom and cadaver models under computed tomography (CT) and MR imaging guidance as a proof-of-concept.

8.2 Future Work

In this subsection, potential future work related to the smart actuation modules, intrinsic sensors, and the robotic systems is discussed as follows:

1) It is important to redesign the torsion module to enable its application in general surgical procedures. It is desired to enlarge the channel through the module so that more surgical tools, such

as an endoscope camera and micro scissors, can be integrated for surgical procedures in addition to ICH evacuation. Other smart materials, such as magnetically-driven materials and SMP, as well as tendon-driven mechanisms, can be explored for this objective.

2) The second objective is to improve the working performance of the SMA torsion module. To develop an MRI-compatible SMA torsion module, the conductive heating actuation technique can be applied. This requires to develop a mechanism to route a nichrome wire around the SMA spring. An alternative solution is to deposit high-resistance conductive material onto the spring with an electrical insulation layer [133]. To improve the working bandwidth, forced fluidic cooling can be explored [134].

3) The intrinsic shape sensors for the smart actuation modules need to be improved. Long optical fibers should be integrated with the sensor to evaluate its working performance in the MRI environment. The actual rotation of the NICHE robot tip need to be measured by using CT imaging or EM tracking to compare it with the reference when the tip is controlled in the closed-loop mode.

4) The FBG bending sensor needs to be improved to improve flexibility, measurement precision, and measurement range. Frictionless tubing can be threaded outside the sensor to potentially reduce the friction and hysteresis. The hysteric model needs to be solved so that the SMA bending module can potentially be feedback controlled. Other sensing mechanisms, such as nanofibers [135] and liquid metal [136], will be investigated to develop a uni-directional bending sensor to measure the 3D deflection of the bending module under external loading.

5) To manipulate the neurosurgical robot under MR imaging guidance, it is imperative to develop an MRI-compatible robotic headframe. The headframe needs to be designed properly so that it can be fit inside the bore of the MRI scanner. To enable an MRI-compatible robotic headframe, smart materials, tendon-driven mechanisms, and hydraulic actuation systems can be explored.

Appendices

APPENDIX A
HEADFRAME REGISTRATION IN CHAPTER 6

As shown in Figure 6.8, the base plate of the headframe is divided into three sections by the ball joints and five vision markers are placed along the circumference of the base plate in the section between the positive x- and y-axis. Besides, two vision markers are placed on the two bolts used to fix the two ball joints along the positive x- and y-axis, respectively. The position of the six vision markers from the positive x-axis are obtained by the stereoscopic camera and denoted by: $\mathbf{p}_i^C = [x_i^C \; y_i^C \; z_i^C]^T$ $(i \in \{x, 1, 2, \cdots, 5\})$, where the subscript '$x$' denotes the vision marker on the x-axis. These position values are acquired by N times in a period of time. The base plane through the origin of $\{F_B\}$ and all the vision markers is denoted by: $c_1 x + c_2 y + c_3 z = 1$, where c_1, c_2, and c_3 denote three constant coefficients. $\mathbf{C} \equiv [c_1 \; c_2 \; c_3]^T$ can be calculated by solving the following equation using the least-square method:

$$\left[\mathbf{p}_{x1}^C \; \cdots \; \mathbf{p}_{xN}^C \; \mathbf{p}_{11}^C \; \cdots \; \mathbf{p}_{5N}^C\right]_{3\times 6N}^T \mathbf{C} = \mathbf{I}_{6N\times 1} \tag{A.1}$$

To calculate the position of $\{F_B\}$ with respect to $\{F_C\}$, namely $\mathbf{P}_B^C \equiv [x_B^C \; y_B^C \; z_B^C]^T$, the geometric relationship among the vision markers is utilized. The vector between two vision markers with the same distance to the origin of $\{F_B\}$ is perpendicular to the vector from their middle point to the origin of $\{F_B\}$, which yields:

$$(\mathbf{p}_m^C - \mathbf{p}_n^C)\cdot(\mathbf{P}_B^C - \frac{\mathbf{p}_m^C + \mathbf{p}_n^C}{2}) = 0 \tag{A.2}$$

where $m \neq n$ and $m, n \in \{x, 1, 2, \cdots, 5\}$. Since any two vision markers between the x- and y-axis is in compliance with the above geometric constraint, we have:

$$\begin{bmatrix} \mathbf{p}_{11}^{C\,\mathrm{T}} - \mathbf{p}_{21}^{C\,\mathrm{T}} \\ \vdots \\ \mathbf{p}_{41}^{C\,\mathrm{T}} - \mathbf{p}_{51}^{C\,\mathrm{T}} \\ \vdots \\ \mathbf{p}_{4N}^{C\,\mathrm{T}} - \mathbf{p}_{5N}^{C\,\mathrm{T}} \end{bmatrix} \mathbf{P}_B^C = \frac{1}{2} \begin{bmatrix} \|\mathbf{p}_{11}^C\|^2 - \|\mathbf{p}_{21}^C\|^2 \\ \vdots \\ \|\mathbf{p}_{41}^C\|^2 - \|\mathbf{p}_{51}^C\|^2 \\ \vdots \\ \|\mathbf{p}_{4N}^C\|^2 - \|\mathbf{p}_{5N}^C\|^2 \end{bmatrix} \tag{A.3}$$

In addition to the above geometric relationship, the origin of $\{F_B\}$ is on the base plane, which yields:

$$\mathbf{C}^{\mathrm{T}}\mathbf{P}_B^C = 1 \tag{A.4}$$

To solve the above overdetermined system, Equation (A.4) is rewritten by representing z_B^C in terms of x_B^C and y_B^C. By substituting the rewritten Equation (A.4) into Equation (A.3), the overdetermined system can be solved using the least-square approach and $\mathbf{P}_B^C$ can be thereby estimated. Therefore, the unit vectors along the x-, y-, and z-axis of $\{F_B\}$ with respect to $\{F_C\}$ are given by:

$$\begin{aligned} \hat{\mathbf{u}} &= \frac{\mathbf{p}_x^C - \mathbf{P}_B^C}{\|\mathbf{p}_x^C - \mathbf{P}_B^C\|} \\ \hat{\mathbf{w}} &= -\frac{\mathbf{C}}{\|\mathbf{C}\|} \\ \hat{\mathbf{v}} &= \hat{\mathbf{w}} \times \hat{\mathbf{u}} \end{aligned} \tag{A.5}$$

The rotation matrix mapping $\{F_B\}$ to $\{F_C\}$ is given by:

$$\mathbf{R}_B^C = \begin{bmatrix} \hat{\mathbf{u}} & \hat{\mathbf{v}} & \hat{\mathbf{w}} \end{bmatrix} \tag{A.6}$$

APPENDIX B

USE OF COPYRIGHTED MATERIALS AND PERMISSIONS

1. © 2019 IEEE. Reprinted, with permission, from Jaydev P. Desai, **Jun Sheng**, Shing Shin Cheng, Xuefeng Wang, Nancy J. Deaton, and Nahian Rahman, "Towards Patient-Specific 3D-Printed Robotic Systems for Surgical Interventions", *IEEE Transactions on Medical Robotics and Bionics*, May 2019.

2. © 2019 IEEE. Reprinted, with permission, from **Jun Sheng**, Nancy J. Deaton, and Jaydev P. Desai, "A Large-Deflection FBG Bending Sensor for the SMA Bending Module", *2019 IEEE International Conference on Robotics and Automation (ICRA 2019)*, May 2019.

3. © 2018 IEEE. Reprinted, with permission, from **Jun Sheng**, Xuefeng Wang, Timm-Michael L. Dickfeld, and Jaydev P. Desai, "Towards the Development of A Steerable and MRI-Compatible Cardiac Catheter for Atrial Fibrillation Treatment", *IEEE Robotics and Automation Letters*, Oct. 2018.

4. © 2018 IEEE. Reprinted, with permission, from **Jun Sheng** and Jaydev P. Desai, "A Highly Compact Fiberoptic Rotation Sensor for a Neurosurgical Robot", *2018 IEEE International Symposium on Medical Robotics (ISMR 2018)*, Mar. 2018.

5. © 2018 IEEE. Reprinted, with permission, from **Jun Sheng** and Jaydev P. Desai, "Development of a Meso-Scale Fiberoptic Rotation Sensor for a Torsion Actuator", *IEEE Robotics and Automation Letters*, Jan. 2018.

6. © 2017 IEEE. Reprinted, with permission, from **Jun Sheng** and Jaydev P. Desai, "A Skull-Mounted Robotic Headframe for a Neurosurgical Robot", *2017 IEEE/RSJ International Conference on Intelligent Robots and Systems (IROS 2017)*, Sep. 2017.

7. © 2017 IEEE. Reprinted, with permission, from **Jun Sheng**, Dheeraj Gandhi, Rao Gullapalli, Marc Simard, and Jaydev P. Desai, "Development of a Meso-Scale SMA-Based Torsion Actuator for Image-Guided Procedures", *IEEE Transactions on Robotics*, Feb. 2017.

8. © 2015 IEEE. Reprinted, with permission, from **Jun Sheng** and Jaydev P. Desai, "A Novel Meso-Scale SMA-Actuated Torsion Actuator", *2015 IEEE/RSJ International Conference on Intelligent Robots and Systems (IROS 2015)*, Sep. 2015.

9. © 2015 IEEE. Reprinted, with permission, from **Jun Sheng** and Jaydev P. Desai, "Towards a SMA-Actuated Neurosurgical Intracerebral Hemorrhage Evacuation (NICHE) robot", *2015 IEEE/RSJ International Conference on Intelligent Robots and Systems (IROS 2015)*, Sep. 2015.

10. © Copyright 2015 IOP Publishing. Reprinted, with permission, from **Jun Sheng** and Jaydev P. Desai, "Design, Modeling and Characterization of A Novel Meso-Scale SMA-Actuated Torsion Actuator", *Smart Materials and Structures*, Aug. 2015.

BIBLIOGRAPHY

[1] Thomas G Weiser, Scott E Regenbogen, Katherine D Thompson, Alex B Haynes, Stuart R Lipsitz, William R Berry, and Atul A Gawande. An estimation of the global volume of surgery: a modelling strategy based on available data. *The Lancet*, 372(9633):139–144, 2008.

[2] Michele L McCarroll, Melissa D Zullo, G Dante Roulette, Thomas M Mendise, Edward Ferris, Jessica Zolton, Stephen J Andrews, and Vivian E von Gruenigen. Development and implementation results of an interactive computerized surgical checklist for robotic-assisted gynecologic surgery. *Journal of robotic surgery*, 9(1):11–18, 2015.

[3] Adam Wittek, Karol Miller, Ron Kikinis, and Simon K Warfield. Patient-specific model of brain deformation: Application to medical image registration. *Journal of biomechanics*, 40(4):919–929, 2007.

[4] Yik San Kwoh, Joahin Hou, Edmond A Jonckheere, and Samad Hayati. A robot with improved absolute positioning accuracy for CT guided stereotactic brain surgery. *IEEE Transactions on Biomedical Engineering*, 35(2):153–160, 1988.

[5] James M Drake, Michael Joy, Andrew Goldenberg, and David Kreindler. Computer-and robot-assisted resection of thalamic astrocytomas in children. *Neurosurgery*, 29(1):27–33, 1991.

[6] JH Chung, KH Huh, SY Kim, DS Kwon, Jungju Lee, and YS Yoon. Development of a surgical robot for total hip arthroplasty. In *Proceeding of 2nd International Workshop on Human-Friendly Welfare Robotic Systems*, pages 106–111, 2001.

[7] Satyam Kalan, Sanket Chauhan, Rafael F Coelho, Marcelo A Orvieto, Ignacio R Camacho, Kenneth J Palmer, and Vipul R Patel. History of robotic surgery. *Journal of Robotic Surgery*, 4(3):141–147, 2010.

[8] TRK Varma and P Eldridge. Use of the neuromate stereotactic robot in a frameless mode for functional neurosurgery. *The International Journal of Medical Robotics and Computer Assisted Surgery*, 2(2):107–113, 2006.

[9] Jorge Gonzalez-Martinez, Sumeet Vadera, Jeffrey Mullin, Rei Enatsu, Andreas V Alexopoulos, Ravish Patwardhan, William Bingaman, and Imad Najm. Robot-assisted stereotactic laser ablation in medically intractable epilepsy: Operative technique. *Operative Neurosurgery*, 10(2):167–173, 2014.

[10] Sarah Ferrand-Sorbets, D Taussig, Martine Fohlen, Christine Bulteau, Georg Dorfmuller, and Olivier Delalande. Frameless stereotactic robot-guided placement of depth electrodes for stereo-electroencephalography in the presurgical evaluation of children with drug-resistant focal epilepsy. In *CNS Annual Meeting*, 2010.

[11] Michel Lefranc, Cyrille Capel, Anne-Sophie Pruvot-Occean, Anthony Fichten, Christine Desenclos, Patrick Toussaint, Daniel Le Gars, and Johann Peltier. Frameless robotic stereotactic biopsies: a consecutive series of 100 cases. *Journal of neurosurgery*, 122(2):342–352, 2015.

[12] Alvaro Bertelsen, Javier Melo, Emilio Sánchez, and Diego Borro. A review of surgical robots for spinal interventions. *The International Journal of Medical Robotics and Computer Assisted Surgery*, 9(4):407–422, 2013.

[13] Nieves Calcerrada Díaz-Santos, Juan Antonio Blasco Amaro, Gloria Ariza Cardiel, and Elena Andradas Aragonés. The safety and efficacy of robotic image-guided radiosurgery system treatment for intra-and extracranial lesions: a systematic review of the literature. *Radiotherapy and Oncology*, 89(3):245–253, 2008.

[14] G Nikolic, B Jerbic, and D Chudy. Robotic aplications in surgery with special emphasis on aplications in neurosurgery. *DAAAM International Scientific Book*, pages 149–173, 2013.

[15] Dong-Geol Choi, Byung-Ju Yi, and Whee-Kuk Kim. Design of a spring backbone micro endoscope. In *Intelligent Robots and Systems, 2007. IROS 2007. IEEE/RSJ International Conference on*, pages 1815–1821. IEEE, 2007.

[16] Nabil Simaan, Russell Taylor, and Paul Flint. High dexterity snake-like robotic slaves for minimally invasive telesurgery of the upper airway. In *International Conference on Medical Image Computing and Computer-Assisted Intervention*, pages 17–24. Springer, 2004.

[17] Mingyen Ho, Yeongjin Kim, Shing Shin Cheng, Rao Gullapalli, and Jaydev P Desai. Design, development, and evaluation of an MRI-guided SMA spring-actuated neurosurgical robot. *The International Journal of Robotics Research*, 34(8):1147–1163, 2015.

[18] Hao Su, Gang Li, D Caleb Rucker, Robert J Webster III, and Gregory S Fischer. A concentric tube continuum robot with piezoelectric actuation for MRI-guided closed-loop targeting. *Annals of Biomedical Engineering*, 44(10):2863–2873, 2016.

[19] Patrick Sears and Pierre Dupont. A steerable needle technology using curved concentric tubes. In *Intelligent Robots and Systems, 2006 IEEE/RSJ International Conference on*, pages 2850–2856. IEEE, 2006.

[20] Robert J Webster, Joseph M Romano, and Noah J Cowan. Kinematics and calibration of active cannulas. In *Robotics and Automation, 2008. ICRA 2008. IEEE International Conference on*, pages 3888–3895. IEEE, 2008.

[21] Taoming Liu, Nate Lombard Poirot, Dominique Franson, Nicole Seiberlich, Mark A Griswold, and M Cenk Çavuşoğlu. Modeling and validation of the three-dimensional deflection of an MRI-compatible magnetically actuated steerable catheter. *IEEE Transactions on Biomedical Engineering*, 63(10):2142–2154, 2016.

[22] Johnathan A Engh, G Podnar, D Kondziolka, and Cameron N Riviere. Toward effective needle steering in brain tissue. In *Engineering in Medicine and Biology Society, 2006. EMBS'06. 28th Annual International Conference of the IEEE*, pages 559–562. IEEE, 2006.

[23] Elif Ayvali, Chia-Pin Liang, Mingyen Ho, Yu Chen, and Jaydev P Desai. Towards a discretely actuated steerable cannula for diagnostic and therapeutic procedures. *The International Journal of Robotics Research*, 31(5):588–603, 2012.

[24] Mingyen Ho, Alan B McMillan, J Marc Simard, Rao Gullapalli, and Jaydev P Desai. Toward a meso-scale SMA-actuated MRI-compatible neurosurgical robot. *IEEE Transactions on Robotics*, 28(1):213–222, 2012.

[25] Yeongjin Kim, Shing Shin Cheng, Mahamadou Diakite, Rao P Gullapalli, J Marc Simard, and Jaydev P Desai. Toward the development of a flexible mesoscale MRI-compatible neurosurgical continuum robot. *IEEE Transactions on Robotics*, 33(6):1386–1397, 2017.

[26] Philip J Swaney, Jessica Burgner, Ray A Lathrop, Hunter B Gilbert, Kyle D Weaver, and Robert J Webster. Minimally-invasive intracerebral hemorrhage removal using an active cannula. In *Robotics and Automation (ICRA), 2013 IEEE International Conference on*, pages 219–224. IEEE, 2013.

[27] Yue Chen, Isuru S Godage, Saikat Sengupta, Cindy Lin Liu, Kyle D Weaver, Eric J Barth, and Robert J Webster. An MRI-compatible robot for intracerebral hemorrhage removal. In *2017 design of medical devices conference*, pages V001T08A019–V001T08A019. American Society of Mechanical Engineers, 2017.

[28] Lisa A Lyons, Robert J Webster, and Ron Alterovitz. Planning active cannula configurations through tubular anatomy. In *2010 IEEE international Conference on Robotics and Automation*, pages 2082–2087. IEEE, 2010.

[29] Cenk Baykal, Luis G Torres, and Ron Alterovitz. Optimizing design parameters for sets of concentric tube robots using sampling-based motion planning. In *2015 IEEE/RSJ International Conference on Intelligent Robots and Systems (IROS)*, pages 4381–4387. IEEE, 2015.

[30] Robert J Webster, Jin Seob Kim, Noah J Cowan, Gregory S Chirikjian, and Allison M Okamura. Nonholonomic modeling of needle steering. *The International Journal of Robotics Research*, 25(5-6):509–525, 2006.

[31] Hunter B Gilbert, D Caleb Rucker, and Robert J Webster III. Concentric tube robots: The state of the art and future directions. In *Robotics Research*, pages 253–269. Springer, 2016.

[32] Hao Su, Diana C Cardona, Weijian Shang, Alexander Camilo, Gregory A Cole, D Caleb Rucker, Robert J Webster, and Gregory S Fischer. A MRI-guided concentric tube continuum robot with piezoelectric actuation: a feasibility study. In *Robotics and Automation (ICRA), 2012 IEEE International Conference on*, pages 1939–1945. IEEE, 2012.

[33] Xuefeng Wang, Shing Shin Cheng, and Jaydev P Desai. Design, analysis, and evaluation of a remotely actuated MRI-compatible neurosurgical robot. *IEEE Robotics and Automation Letters*, 3(3):2144–2151, 2018.

[34] Jun Zhang, Jun Sheng, Ciaran T ONeill, Conor J Walsh, Robert J Wood, Jee Hwan Ryu, Jaydev P Desai, and Michael C Yip. Robotic artificial muscles: Current progress and future perspectives. *IEEE Transactions on Robotics*, 2019.

[35] Robert J Wood. The first takeoff of a biologically inspired at-scale robotic insect. *IEEE Transactions on Robotics*, 24(2):341–347, 2008.

[36] Ron Pelrine, Roy D Kornbluh, Qibing Pei, Scott Stanford, Seajin Oh, Joseph Eckerle, Robert J Full, Marcus A Rosenthal, and Kenneth Meijer. Dielectric elastomer artificial muscle actuators: Toward biomimetic motion. In *Smart Structures and Materials 2002: Electroactive polymer actuators and devices (EAPAD)*, volume 4695, pages 126–138. International Society for Optics and Photonics, 2002.

[37] Mihai Duduta, David R Clarke, and Robert J Wood. A high speed soft robot based on dielectric elastomer actuators. In *2017 IEEE International Conference on Robotics and Automation (ICRA)*, pages 4346–4351. IEEE, 2017.

[38] Seok Heo, Tedy Wiguna, Hoon Cheol Park, and Nam Seo Goo. Effect of an artificial caudal fin on the performance of a biomimetic fish robot propelled by piezoelectric actuators. *Journal of Bionic Engineering*, 4(3):151–158, 2007.

[39] Arne Ölander. An electrochemical investigation of solid cadmium-gold alloys. *Journal of the American Chemical Society*, 54(10):3819–3833, 1932.

[40] Je-sung Koh, Sa-reum Kim, and Kyu-jin Cho. Self-folding origami using torsion shape memory alloy wire actuators. In *ASME 2014 International Design Engineering Technical Conferences and Computers and Information in Engineering Conference*, pages V05BT08A043–V05BT08A043. American Society of Mechanical Engineers, 2014.

[41] Han Zhang, Yves Bellouard, Thomas C Sidler, Etienne Burdet, Aun-Neow Poo, and Reymond Clavel. Monolithic shape memory alloy microgripper for 3D assembly of tissue engineering scaffolds. In *Microrobotics and Microassembly III*, volume 4568, pages 50–61. International Society for Optics and Photonics, 2001.

[42] Leia Stirling, Chih-Han Yu, Jason Miller, Elliot Hawkes, Robert Wood, Eugene Goldfield, and Radhika Nagpal. Applicability of shape memory alloy wire for an active, soft orthotic. *Journal of Materials Engineering and Performance*, 20(4-5):658–662, 2011.

[43] Weiming Huang. Two-way behavior of a Nitinol torsion bar. In *Smart Structures and Materials 1999: Smart Materials Technologies*, volume 3675, pages 284–295. International Society for Optics and Photonics, 1999.

[44] W Huang and W Toh. Training two-way shape memory alloy by reheat treatment. *Journal of Materials Science Letters*, 19(17):1549–1550, 2000.

[45] Mohammad H Elahinia, Hashem Ashrafiuon, Mehdi Ahmadian, and Hanghao Tan. A temperature-based controller for a shape memory alloy actuator. *Transactions of the ASME-L-Journal of Vibration and Acoustics*, 127(3):285–291, 2005.

[46] Veturia CHIROIU and Ligia MUNTEANU. A flexible beam actuated by a shape memory alloy ribbon. *Proc. of the Romanian Academy, Series A: Mathematics, Physics, Technical Sciences, Information Science*, 4(1):1–7, 2003.

[47] Jaronie Mohd Jani, Martin Leary, and Aleksandar Subic. Designing shape memory alloy linear actuators: a review. *Journal of Intelligent Material Systems and Structures*, page 1045389X16679296, 2016.

[48] Seok Chang Ryu, Zhan Fan Quek, Je-Sung Koh, Pierre Renaud, Richard J Black, Behzad Moslehi, Bruce L Daniel, Kyu-Jin Cho, and Mark R Cutkosky. Design of an optically controlled MR-compatible active needle. *IEEE Transactions on Robotics*, 31(1):1–11, 2015.

[49] Seok Chang Ryu, Pierre Renaud, Richard J Black, Bruce L Daniel, and Mark R Cutkosky. Feasibility study of an optically actuated MR-compatible active needle. In *Intelligent Robots and Systems (IROS), 2011 IEEE/RSJ International Conference on*, pages 2564–2569. IEEE, 2011.

[50] Jae-Eul Shim, Ying-Jun Quan, Wei Wang, Hugo Rodrigue, Sung-Hyuk Song, and Sung-Hoon Ahn. A smart soft actuator using a single shape memory alloy for twisting actuation. *Smart Materials and Structures*, 24(12):125033, 2015.

[51] Joël Abadie, Nicolas Chaillet, and C Lexcellent. Modeling of a new SMA micro-actuator for active endoscopy applications. *Mechatronics*, 19(4):437–442, 2009.

[52] Joshua Gafford, Hiroyuki Aihara, Christopher Thompson, Robert Wood, and Conor Walsh. Distal proprioceptive sensor for motion feedback in endoscope-based modular robotic systems. *IEEE Robotics and Automation Letters*, 3(1):171–178, 2018.

[53] Geunbae Lim, Kazuyuki Minami, Masahisa Sugihara, Masaru Uchiyama, and Masayoshi Esashi. Active catheter with multi-link structure based on silicon micromachining. In *Micro Electro Mechanical Systems, 1995, MEMS'95, Proceedings. IEEE*, page 116. IEEE, 1995.

[54] Y Haga, Y Tanahashi, and M Esashi. Small diameter active catheter using shape memory alloy. In *Micro Electro Mechanical Systems, 1998. MEMS 98. Proceedings., The Eleventh Annual International Workshop on*, pages 419–424. IEEE, 1998.

[55] Ki-Tae Park and Masayoshi Esashi. A multilink active catheter with polyimide-based integrated CMOS interface circuits. *Journal of Microelectromechanical Systems*, 8(4):349–357, 1999.

[56] T Mineta, T Mitsui, Y Watanabe, S Kobayashi, Y Haga, and M Esashi. Batch fabricated flat meandering shape memory alloy actuator for active catheter. *Sensors and Actuators A: Physical*, 88(2):112–120, 2001.

[57] Takashi Mineta, Toshiaki Mitsui, Yoshiyuki Watanabe, Seiya Kobayashi, Youichi Haga, and Masayoshi Esashi. An active guide wire with shape memory alloy bending actuator fabricated by room temperature process. *Sensors and Actuators A: Physical*, 97:632–637, 2002.

[58] Chen Liang, Frank M Davidson, Lawrence M Schetky, and Friedrich K Straub. Applications of torsional shape memory alloy actuators for active rotor blade control: opportunities and limitations. In *1996 Symposium on Smart Structures and Materials*, pages 91–100. International Society for Optics and Photonics, 1996.

[59] G Song. Design and control of a Nitinol wire actuated rotary servo. *Smart Materials and Structures*, 16(5):1796, 2007.

[60] Chao-Chieh Lan, Jhe-Hong Wang, and Chen-Hsien Fan. Optimal design of rotary manipulators using shape memory alloy wire actuated flexures. *Sensors and Actuators A: Physical*, 153(2):258–266, 2009.

[61] Yeongjin Kim and Jaydev P Desai. Design and kinematic analysis of a neurosurgical spring-based continuum robot using SMA spring actuators. In *Intelligent Robots and Systems (IROS), 2015 IEEE/RSJ International Conference on*, pages 1428–1433. IEEE, 2015.

[62] Chaoyang Shi, Xiongbiao Luo, Peng Qi, Tianliang Li, Shuang Song, Zoran Najdovski, Toshio Fukuda, and Hongliang Ren. Shape sensing techniques for continuum robots in minimally invasive surgery: a survey. *IEEE Transactions on Biomedical Engineering*, 64(8):1665–1678, 2017.

[63] Thomas Schulz, Silvia Puccini, Jens-Peter Schneider, and Thomas Kahn. Interventional and intraoperative MR: Review and update of techniques and clinical experience. *European Radiology*, 14(12):2212–2227, 2004.

[64] Hongliang Ren and Pierre E Dupont. Tubular enhanced geodesic active contours for continuum robot detection using 3D ultrasound. In *Robotics and Automation (ICRA), 2012 IEEE International Conference on*, pages 2907–2912. IEEE, 2012.

[65] Byoungho Lee. Review of the present status of optical fiber sensors. *Optical Fiber Technology*, 9(2):57–79, 2003.

[66] Roy J Roesthuis, Marco Kemp, John J van den Dobbelsteen, and Sarthak Misra. Three-dimensional needle shape reconstruction using an array of fiber Bragg grating sensors. *IEEE/ASME Transactions on Mechatronics*, 19(4):1115–1126, 2014.

[67] Yong-Lae Park, Santhi Elayaperumal, Bruce Daniel, Seok Chang Ryu, Mihye Shin, Joan Savall, Richard J Black, Behzad Moslehi, and Mark R Cutkosky. Real-time estimation of 3-D needle shape and deflection for MRI-guided interventions. *IEEE/ASME Transactions On Mechatronics*, 15(6):906–915, 2010.

[68] Ran Xu, Aaron Yurkewich, and Rajni V Patel. Curvature, torsion, and force sensing in continuum robots using helically wrapped FBG sensors. *IEEE Robotics and Automation Letters*, 1(2):1052–1059, 2016.

[69] Seok Chang Ryu and Pierre E Dupont. FBG-based shape sensing tubes for continuum robots. In *Robotics and Automation (ICRA), 2014 IEEE International Conference on*, pages 3531–3537. IEEE, 2014.

[70] FM Araújo, LA Ferreira, JL Santos, and F Farahi. Temperature and strain insensitive bending measurements with D-type fibre Bragg gratings. *Measurement Science and Technology*, 12(7):829, 2001.

[71] Xianfeng Chen, Chi Zhang, David J Webb, Kyriacos Kalli, and Gang-Ding Peng. Highly sensitive bend sensor based on Bragg grating in eccentric core polymer fiber. *IEEE Photonics Technology Letters*, 22(11):850–852, 2010.

[72] Hao Liu, Amirhossein Farvardin, Sahba Aghajani Pedram, Iulian Iordachita, Russell H Taylor, and Mehran Armand. Large deflection shape sensing of a continuum manipulator for

minimally-invasive surgery. In *IEEE International Conference on Robotics and Automation: ICRA:[proceedings] IEEE International Conference on Robotics and Automation*, volume 2015, page 201. NIH Public Access, 2015.

[73] Shahriar Sefati, Farshid Alambeigi, Iulian Iordachita, Mehran Armand, and Ryan J Murphy. FBG-based large deflection shape sensing of a continuum manipulator: Manufacturing optimization. In *SENSORS, 2016 IEEE*, pages 1–3. IEEE, 2016.

[74] Lucas Elijovich, Pratik V Patel, and J Claude Hemphill. Intracerebral hemorrhage. In *Seminars in Neurology*, volume 28, pages 657–667. © Thieme Medical Publishers, 2008.

[75] Martin S Dennis, JP Burn, PA Sandercock, John M Bamford, Derick T Wade, and Charles P Warlow. Long-term survival after first-ever stroke: the oxfordshire community stroke project. *Stroke*, 24(6):796–800, 1993.

[76] Benjamin Barnes, Daniel F Hanley, and Juan R Carhuapoma. Minimally invasive surgery for intracerebral haemorrhage. *Current Opinion in Critical Care*, 20(2):148–152, 2014.

[77] Takeshi Morita, Minoru Kuribayashi Kurosawa, and Toshiro Higuchi. A cylindrical shaped micro ultrasonic motor utilizing PZT thin film (1.4 mm in diameter and 5.0 mm long stator transducer). *Sensors and Actuators A: Physical*, 83(1):225–230, 2000.

[78] Takeshi morita, Minoru Kuribayashi Kurosawa, and Toshiro Higuchi. Cylindrical micro ultrasonic motor utilizing bulk lead zirconate titanate (PZT). *Japanese Journal of Applied Physics*, 38(5S):3347, 1999.

[79] Yutaka Doshida, Sumiaki Kishimoto, Keisuke Ishii, Hiroshi Kishi, Hideki Tamura, Yoshiro Tomikawa, and Seiji Hirose. Miniature cantilever-type ultrasonic motor using Pb-free multilayer piezoelectric ceramics. *Japanese Journal of Applied Physics*, 46(7S):4921, 2007.

[80] Andreas PF Bernhard and Inderjit Chopra. Analysis of a bending-torsion coupled actuator for a smart rotor with active blade tips. *Smart Materials and Structures*, 10(1):35, 2001.

[81] Alfredo Quiñones-Hinojosa, Marcus L Ware, Nader Sanai, and Michael W McDermott. Assessment of image guided accuracy in a skull model: Comparison of frameless stereotaxy techniques vs. frame-based localization. *Journal of Neuro-oncology*, 76(1):65–70, 2006.

[82] Kailash Krishnan, Siti F Mukhtar, James Lingard, Aimee Houlton, Elizabeth Walker, Tanya Jones, Nikola Sprigg, Lesley A Cala, Jennifer L Becker, Robert A Dineen, et al. Performance characteristics of methods for quantifying spontaneous intracerebral haemorrhage: data from the efficacy of nitric oxide in stroke (enos) trial. *Journal of Neurol, Neurosurgery, and Psychiatry*, 86(11):1258–1266, 2015.

[83] Chen Liang and CA Rogers. One-dimensional thermomechanical constitutive relations for shape memory materials. *Journal of Intelligent Material Systems and Structures*, 1(2):207–234, 1990.

[84] Vincent De Sars, Sinan Haliyo, and Jerome Szewczyk. A practical approach to the design and control of active endoscopes. *Mechatronics*, 20(2):251–264, 2010.

[85] John A Shaw, Chris B Churchill, and MA Iadicola. Tips and tricks for characterizing shape memory alloy wire: Part 1-differential scanning calorimetry and basic phenomena. *Experimental Techniques*, 32(5):55–62, 2008.

[86] Andrés Bruhn, Joachim Weickert, and Christoph Schnörr. Lucas/kanade meets horn/schunck: Combining local and global optic flow methods. *International journal of Computer Vision*, 61(3):211–231, 2005.

[87] Zhao Guo, Haoyong Yu, and Liang-Boon Wee. Design of a novel compliant differential shape memory alloy actuator. In *Intelligent Robots and Systems (IROS), 2013 IEEE/RSJ International Conference on*, pages 4925–4930. IEEE, 2013.

[88] M Moallem and VA Tabrizi. Tracking control of an antagonistic shape memory alloy actuator pair. *Control Systems Technology, IEEE Transactions on*, 17(1):184–190, 2009.

[89] Jagadeesan Jayender, Rajnikant V Patel, Suwas Nikumb, and Mile Ostojic. Modeling and control of shape memory alloy actuators. *Control Systems Technology, IEEE Transactions on*, 16(2):279–287, 2008.

[90] Shing Shin Cheng and Jaydev P Desai. Towards high frequency actuation of SMA spring for the neurosurgical robot-MINIR-II. In *Robotics and Automation (ICRA), 2015 IEEE International Conference on*, pages 2580–2585. IEEE, 2015.

[91] Susan Colilla, Ann Crow, William Petkun, Daniel E Singer, Teresa Simon, and Xianchen Liu. Estimates of current and future incidence and prevalence of atrial fibrillation in the US adult population. *The American Journal of Cardiology*, 112(8):1142–1147, 2013.

[92] Marisa Chard and Reza Tabrizchi. The role of pulmonary veins in atrial fibrillation: a complex yet simple story. *Pharmacology & Therapeutics*, 124(2):207–218, 2009.

[93] Carlo Pappone, Salvatore Rosanio, Giuseppe Oreto, Monica Tocchi, Filippo Gugliotta, Gabriele Vicedomini, Adriano Salvati, Cosimo Dicandia, Patrizio Mazzone, Vincenzo Santinelli, et al. Circumferential radiofrequency ablation of pulmonary vein ostia a new anatomic approach for curing atrial fibrillation. *Circulation*, 102(21):2619–2628, 2000.

[94] Pierre Jaïs, Rukshen Weerasooriya, Dipen C Shah, Mélèze Hocini, Laurent Macle, Kee-Joon Choi, Christophe Scavee, Michel Haïssaguerre, and Jacques Clémenty. Ablation therapy for atrial fibrillation (AF). *Cardiovascular Research*, 54(2):337–346, 2002.

[95] Samuel B Kesner and Robert D Howe. Design and control of motion compensation cardiac catheters. In *Robotics and Automation (ICRA), 2010 IEEE International Conference on*, pages 1059–1065. IEEE, 2010.

[96] Hedyeh Rafii-Tari, Christopher J Payne, and Guang-Zhong Yang. Current and emerging robot-assisted endovascular catheterization technologies: a review. *Annals of Biomedical Engineering*, 42(4):697–715, 2014.

[97] D.J. Griffiths. *Introduction to Electrodynamics*. Pearson Education, 2014.

[98] Kodjo Mawuli Armattoe, Céline Bouby, Mohamed Haboussi, and T Ben Zineb. Modeling of latent heat effects on phase transformation in shape memory alloy thin structures. *International Journal of Solids and Structures*, 88:283–295, 2016.

[99] Shing Shin Cheng, Yeongjin Kim, and Jaydev P Desai. New actuation mechanism for actively cooled SMA springs in a neurosurgical robot. *IEEE Transactions on Robotics*, 2017.

[100] T Jesse Lim and David L McDowell. Path dependence of shape memory alloys during cyclic loading. *Journal of Intelligent Material Systems and Structures*, 6(6):817–830, 1995.

[101] Jim H Whitelaw. Convective heat transfer. *International Encyclopedia of Heat and Mass Transfer*, page 237, 1997.

[102] Jose Brandao Faria. A theoretical analysis of the bifurcated fiber bundle displacement sensor. *IEEE Transactions on Instrumentation and Measurement*, 47(3):742–747, 1998.

[103] Pinyo Puangmali, Kaspar Althoefer, and Lakmal D Seneviratne. Mathematical modeling of intensity-modulated bent-tip optical fiber displacement sensors. *IEEE Transactions on Instrumentation and Measurement*, 59(2):283–291, 2010.

[104] Xinhua Yi, Jinwu Qian, Linyong Shen, Yanan Zhang, and Zhen Zhang. An innovative 3D colonoscope shape sensing sensor based on FBG sensor array. In *Information Acquisition, 2007. ICIA'07. International Conference on*, pages 227–232. IEEE, 2007.

[105] Kai Tai Wan, Christopher KY Leung, and Noah G Olson. Investigation of the strain transfer for surface-attached optical fiber strain sensors. *Smart Materials and Structures*, 17(3):035037, 2008.

[106] Shahriar Sefati, Michael Pozin, Farshid Alambeigi, Iulian Iordachita, Russell H Taylor, and Mehran Armand. A highly sensitive fiber Bragg grating shape sensor for continuum manipulators with large deflections. In *SENSORS, 2017 IEEE*, pages 1–3. IEEE, 2017.

[107] Hao Liu, Amirhossein Farvardin, Robert Grupp, Ryan J Murphy, Russell H Taylor, Iulian Iordachita, and Mehran Armand. Shape tracking of a dexterous continuum manipulator utilizing two large deflection shape sensors. *IEEE Sensors Journal*, 15(10):5494–5503, 2015.

[108] Roy J Roesthuis, Sander Janssen, and Sarthak Misra. On using an array of fiber Bragg grating sensors for closed-loop control of flexible minimally invasive surgical instruments. In *Intelligent Robots and Systems (IROS), 2013 IEEE/RSJ International Conference on*, pages 2545–2551. IEEE, 2013.

[109] Jason P Moore and Matthew D Rogge. Shape sensing using multi-core fiber optic cable and parametric curve solutions. *Optics Express*, 20(3):2967–2973, 2012.

[110] Mohammad Al Janaideh, Subhash Rakheja, and Chun-Yi Su. A generalized Prandtl-Ishlinskii model for characterizing the hysteresis and saturation nonlinearities of smart actuators. *Smart Materials and Structures*, 18(4):045001, 2009.

[111] Qing Hang Li, Lucia Zamorano, Abhilash Pandya, Ramiro Perez, Jianxing Gong, and Fernando Diaz. The application accuracy of the NeuroMate robot-A quantitative comparison with frameless and frame-based surgical localization systems. *Computer Aided Surgery*, 7(2):90–98, 2002.

[112] Tzung-Cheng Tsai and Yeh-Liang Hsu. Development of a parallel surgical robot with automatic bone drilling carriage for stereotactic neurosurgery. *Biomedical Engineering: Applications, Basis and Communications*, 19(04):269–277, 2007.

[113] Taiga Nakano, Naohiko Sugita, Takashi Ueta, Yasuhiro Tamaki, and Mamoru Mitsuishi. A parallel robot to assist vitreoretinal surgery. *International Journal of Computer Assisted Radiology and Surgery*, 4(6):517–526, 2009.

[114] Jumpei Arata, Yasunori Tada, Hiroaki Kozuka, Tomohiro Wada, Yoshitaka Saito, Norio Ikedo, Yuichiro Hayashi, Masazumi Fujii, Yasukazu Kajita, Masaaki Mizuno, et al. Neurosurgical robotic system for brain tumor removal. *International Journal of Computer Assisted Radiology and Surgery*, 6(3):375–385, 2011.

[115] L Joskowicz, R Shamir, M Freiman, M Shoham, E Zehavi, F Umansky, and Y Shoshan. Image-guided system with miniature robot for precise positioning and targeting in keyhole neurosurgery. *Computer Aided Surgery*, 11(4):181–193, 2006.

[116] Louis B Kratchman, Grégoire S Blachon, Thomas J Withrow, Ramya Balachandran, Robert F Labadie, and Robert J Webster. Design of a bone-attached parallel robot for percutaneous cochlear implantation. *IEEE Transactions on Biomedical Engineering*, 58(10):2904–2910, 2011.

[117] Jan-Philipp Kobler, Jens Kotlarski, Julian Öltjen, Stephan Baron, and Tobias Ortmaier. Design and analysis of a head-mounted parallel kinematic device for skull surgery. *International Journal of Computer Assisted Radiology and Surgery*, 7(1):137–149, 2012.

[118] Changsheng Li, Nicolas Kon Kam King, and Hongliang Ren. A skull-mounted robot with a compact and lightweight parallel mechanism for positioning in minimally invasive neurosurgery. *Annals of Biomedical Engineering*, pages 1–14, 2018.

[119] Tsuneo Yoshikawa. Manipulability of robotic mechanisms. *The International Journal of Robotics Research*, 4(2):3–9, 1985.

[120] Giovanni Boschetti, Rossella Rosa, and Alberto Trevisani. Parallel robot translational performance evaluation through direction-selective index (DSI). *Journal of Robotics*, 2011, 2011.

[121] Jean-Pierre Merlet. Jacobian, manipulability, condition number, and accuracy of parallel robots. *Journal of Mechanical Design*, 128(1):199–206, 2006.

[122] Tae-Young Lee and Jae-Kyung Shim. Forward kinematics of the general 6-6 Stewart platform using algebraic elimination. *Mechanism and Machine Theory*, 36(9):1073–1085, 2001.

[123] National Electrical Manufacturers Association et al. Determination of signal-to-noise ratio (SNR) in diagnostic magnetic resonance imaging. *NEMA Standards Publication MS 1-2001*, 2001.

[124] Jun Sheng and Jaydev P Desai. Design, modeling and characterization of a novel meso-scale sma-actuated torsion actuator. *Smart Materials and Structures*, 24(10):105005, 2015.

[125] Jun Sheng and Jaydev P Desai. A novel meso-scale sma-actuated torsion actuator. In *2015 IEEE/RSJ International Conference on Intelligent Robots and Systems (IROS)*, pages 4718–4723. IEEE, 2015.

[126] Jun Sheng, Xuefeng Wang, Timm-Michael L Dickfeld, and Jaydev P Desai. Towards the development of a steerable and mri-compatible cardiac catheter for atrial fibrillation treatment. *IEEE Robotics and Automation Letters*, 3(4):4038–4045, 2018.

[127] Jun Sheng and Jaydev P Desai. A highly compact fiberoptic rotation sensor for a neurosurgical robot. In *2018 International Symposium on Medical Robotics (ISMR)*, pages 1–6. IEEE, 2018.

[128] Jun Sheng and Jaydev P Desai. Development of a mesoscale fiberoptic rotation sensor for a torsion actuator. *IEEE Robotics and Automation Letters*, 3(1):537–543, 2017.

[129] Jaydev P Desai, Jun Sheng, Shing Shin Cheng, Xuefeng Wang, Nancy J Deaton, and Nahian Rahman. Toward patient-specific 3d-printed robotic systems for surgical interventions. *IEEE Transactions on Medical Robotics and Bionics*, 1(2):77–87, 2019.

[130] Jun Sheng and Jaydev P Desai. Towards a sma-actuated neurosurgical intracerebral hemorrhage evacuation (niche) robot. In *2015 IEEE/RSJ International Conference on Intelligent Robots and Systems (IROS)*, pages 3805–3810. IEEE, 2015.

[131] Jun Sheng, Dheeraj Gandhi, Rao Gullapalli, J Marc Simard, and Jaydev P Desai. Development of a meso-scale sma-based torsion actuator for image-guided procedures. *IEEE Transactions on Robotics*, 33(1):240–248, 2016.

[132] Jun Sheng and Jaydev P Desai. A skull-mounted robotic headframe for a neurosurgical robot. In *2017 IEEE/RSJ International Conference on Intelligent Robots and Systems (IROS)*, pages 2511–2516. IEEE, 2017.

[133] Jamie K Paik and Robert J Wood. A bidirectional shape memory alloy folding actuator. *Smart Materials and Structures*, 21(6):065013, 2012.

[134] Joshua B Gafford, Robert J Wood, and Conor J Walsh. A high-force, high-stroke distal robotic add-on for endoscopy. In *Robotics and Automation (ICRA), 2017 IEEE International Conference on*, pages 1117–1124. IEEE, 2017.

[135] Changhyun Pang, Gil-Yong Lee, Tae-il Kim, Sang Moon Kim, Hong Nam Kim, Sung-Hoon Ahn, and Kahp-Yang Suh. A flexible and highly sensitive strain-gauge sensor using reversible interlocking of nanofibres. *Nature materials*, 11(9):795, 2012.

[136] Seokbeom Kim, Jungchul Lee, and Bumkyoo Choi. Stretching and twisting sensing with liquid-metal strain gauges printed on silicone elastomers. *IEEE Sensors Journal*, 15(11):6077–6078, 2015.

VITA

Jun Sheng earned his Bachelor of Science degree in Mechanical Engineering from Shanghai Jiao Tong University, Shanghai, China, in 2011. He also received his Master of Science degree in Electrical Engineering from National Taiwan University, Taipei, Taiwan, in 2013. In June of 2014, he began his doctoral program in the Department of Mechanical Engineering at the University of Maryland, College Park, and transferred to the doctoral program in Robotics at the Georgia Institute of Technology in August of 2016. His research interests are centered around surgical robotics, smart actuation and sensing, and biomedical devices.